In presenting this thesis or dissertation as a partial fulfillment of the requirements for an advanced degree from Emory University, I hereby grant to Emory University and its agents the non-exclusive license to archive, make accessible, and display my thesis or dissertation in whole or in part in all forms of media, now or hereafter known, including display on the world wide web. I understand that I may select some access restrictions as part of the online submission of this thesis or dissertation. I retain all ownership rights to the copyright of the thesis or dissertation. I also retain the right to use in future works (such as articles or books) all or part of this thesis or dissertation.

Signature:

_____	_____
Ivan Antonov	Date

SPECTROSCOPIC STUDIES OF MOLECULES THAT CHALLENGE COMPUTATIONAL CHEMISTRY

By
Ivan Antonov
Doctor of Philosophy

Chemistry

_____
Michael C. Heaven
Advisor

_____
Joel M. Bowman
Committee Member

_____
Tim Lian
Committee Member

Accepted:

_____
Lisa A. Tedesco, Ph.D.
Dean of the James T. Laney School of Graduate Studies

_____
Date

SPECTROSCOPIC STUDIES OF MOLECULES THAT CHALLENGE COMPUTATIONAL CHEMISTRY

By

Ivan Antonov

B.S., Samara State University, 2002

Advisor: Michael C. Heaven, Ph.D.

An abstract of

A dissertation submitted to the Faculty of the

James T. Laney School of Graduate Studies of Emory University

in partial fulfillment of the requirement for the degree of

Doctor of Philosophy

in Chemistry

2013

Abstract

Spectroscopic Studies of Molecules that Challenge Computational Chemistry

By Ivan Antonov

The gas-phase electronic spectra of small Be-containing ($Be2^+$, $BeOBe^+$, BeC), Hf-containing (HfF^+ and HfS^+) and actinide molecules (ThF, ThF^+, UF and UF^+) were recorded with variety of experimental techniques. *Ab initio* electronic structure calculations were used to facilitate the assignment of the observed spectra.

The ground electronic states of Be_2^+ and $BeOBe^+$ were probed using the PFI-ZEKE technique. The rotational symmetry selection rules were used to confirm the symmetry of the ground state as $^2\Sigma_u$ in Be_2^+ and $^2\Sigma_g^+$ in $BeOBe^+$. The ionization energies were refined over previous measurements. Results from recent theoretical calculations are in good agreement with the experimental data.

Electronic spectra for BeC were recorded over the range 30500-40000 cm^{-1}. The vibronic structure consists of a series of bands with erratic energy spacings. Theoretical calculations indicate that the erratic vibronic structure results from strong interactions between the four lowest energy $^3\Pi$ states. The predictions were sufficiently close to the observed structure to permit partial assignment of the spectra. Bands originating from the low-lying $1^5\Sigma^-$ state were also identified, yielding a $^5\Sigma^-$ to $X^3\Sigma^-$ energy interval of 2305±80 cm^{-1}.

The electronic spectra for HfS^+ and HfF^+ were recorded with PFI-ZEKE technique. Three electronic states were identified in HfS^+ and four in HfF^+. The ionization energies for neutral molecules, term energies and molecular constants for the ground and low-lying states of cations are reported. The results for HfF^+ support the contention that HfF^+ is a viable candidate for electron electric dipole moment measurements. The spacings between adjacent $X^1\Sigma^+$ and $^3\Delta_1$ levels are found to be less favorable for the proposed studies of the fine structure constant.

The low-lying states of ThF^+ and UF^+ were probed PFI-ZEKE photoelectron spectroscopy. Vibronic progressions belonging to four electronic states of ThF^+ and sixteen electronic states of UF^+ were identified. The ground state in ThF^+ is tentatively assigned as $^1\Sigma^+$. The $^3\Delta_1$ state of ThF^+, of interest for investigation of the electron electric dipole moment, is just 315.0(5) cm^{-1} above the ground state. The observed patterns of low-lying electronic states of UF^+ are consistent with *ab initio* calculations and ligand field theory predictions.

SPECTROSCOPIC STUDIES OF MOLECULES THAT CHALLENGE COMPUTATIONAL CHEMISTRY

By

Ivan Antonov

B.S., Samara State University, 2002

Advisor: Michael C. Heaven, Ph.D.

A dissertation submitted to the Faculty of the

James T. Laney School of Graduate Studies of Emory University

in partial fulfillment of the requirement for the degree of

Doctor of Philosophy

in Chemistry

2013

ACKNOWLEDGEMENTS

I would like to express my deepest gratitude to my advisor Dr. Michael Heaven for inviting me to visit Emory University and start the graduate program. He is very patient adviser and competent scientist. His support, encouragement and advice were keys to success of my studies.

I would also like to thank my committee members as well as all Physical Chemistry division faculty members for their input on my research. Special thanks to Drs. Joel Bowman, Tim Lian and James Kindt for their graduate courses and cumulative exams.

I would like to extend my gratitude to the current and past members of Heaven lab for their contribution to my research and for creating friendly environment in the lab. My sincere appreciation goes to Drs. Valery Azyazov, Vasily Goncharov, Jeremy Merritt, Beau Barker and Jiande Han.

I would like to thank my school teachers of School N41, Samara, Russia and professors of Samara State University for sharing their knowledge and experience with me and giving me the basic skills that helped me in my academic career.

I am very grateful to my parents and my grandmother for raising me and supporting my interest in sciences. I thank my wife, Elena Antonova, for being with me and for her support and love.

Table of Contents

List of tables

List of figures

CHAPTER I

INTRODUCTION

Ab initio computational chemistry in recent decades has developed into efficient and - powerful tool for predicting chemical and physical properties of molecules. It can attempt to calculate geometry of a stable molecule, relative energies of different geometrical and electronic configurations, molecular properties such as dipole moment, polarizability, energy of dissociation and ionization etc. The methods of computational chemistry provide very accurate data for small molecules and molecules formed by light elements.

Accurate *ab initio* calculations however can be complicated for certain systems. As the cost of computation increases non-linearly with number of electrons, molecules that contain more than few atoms should be treated at less computationally expensive and less accurate levels of theory. Di- and triatomic molecules may contain too many electrons for accurate computation if they formed by atoms of heavy elements such as actinides.

Ab initio calculation become significantly more expensive when relativistic effects have to be included for accurate results. As the charge of nuclei increases, the velocities of inner shell electrons approach the speed of light and relativistic effects cannot be ignored. Actinide-containing molecules require either explicit relativistic treatment or approximations such as the use of a Relativistic Effective Core Potential (RECP) where the relativistic effects are implicitly included in the ECP parameters.

Another challenge for *ab initio* calculations is posed by molecules that require multireference treatments in order to adequately recover the correlation energy. This situation can occur when a molecule has several outer shell electrons that can be distributed among a set of nearly degenerate orbitals. Accurate solution of this problem requires multireference methods

which are less accurate and significantly more computationally expensive than single reference methods. Molecules formed by heavy elements and transition metals often require multireference treatment. Another example where multireference character is observed in molecules formed by light elements is beryllium-containing species such as Be_2 and BeOBe.

As computational chemists develop new methods to solve complicated problems they require accurate benchmark data against which the results of calculations can be verified. The benchmark data can be either experimental (e.g. obtained by spectroscopy, X-ray structure analysis, NMR etc.) or theoretical (obtained by higher level theory method). Comparison of measured and calculated data provides the means for validation and refinement of computational methods.

Gas-phase molecular spectroscopy is one of the tools used to provide experimental benchmark data. It can be used to probe the geometry of molecules, electronic structure, thermodynamic properties such as the energies of ionization and dissociation, force constants, spin-orbit coupling constants etc. An advantage of gas-phase spectroscopy is that target molecules are free from solvation effects. Therefore, the information obtained is only related to the properties of target species. This allows for direct comparison with results of accurate *ab initio* calculations. Another advantage of isolating molecules in the gas phase is that it permits studies of radicals and ions.

In recent years, high level *ab initio* calculations have been applied to a number of small actinide-containing molecules[1-3]. However, accurate gas phase data for evaluation of theoretical methods is still unavailable for a large number of molecules formed by actinides[1]. Often, spectroscopic data are lacking for the isoelectronic species such as molecular ions or molecules formed by the elements that belong to the same group in periodic table.

Small diatomic and triatomic molecules are interesting targets because they are building blocks of larger systems. The simple chemical bonds that exist in them can be probed in isolation and results can be applied to study of larger systems. Beyond the issue of testing the theoretical

methods, accurate gas phase spectroscopy data on these molecules have practical and fundamental significance. Characteristic spectral features are useful for spectral analysis. Ionization and dissociation energies are used in calculating of other thermodynamic properties.

In this thesis, several neutral and ionic species are studied using various gas-phase spectroscopic techniques. Approximately one half consisted of Be atoms bound to Be, O and C. The remainder were actinides or hafnium bound to O, F or S.

Beryllium compounds are interesting and challenging from the theoretical point of view. The Be atom itself demonstrates multireference effects and is often chosen as an illustrative model system in textbooks[4]. Be compounds also exhibit multireference characteristics, and there have been many computational studies, conducted at varying levels of theory, that produced conflicting predictions. For example the ground state of BeOBe was predicted as either $^1\Sigma_g^+$ or $^3\Sigma_u^+$ depending on the level of theory. It was controversial until recent experimental study[5] where it was shown to be $^1\Sigma_g^+$.

Both Be_2 and BeOBe molecules should not exist according to simple molecular orbital theory because both Be and BeO are closed-shell species[5,6]. However, the beryllium dimer was shown[6-11] to possess weak but surprisingly short bond of 2.45 Å. BeOBe is a stable molecule as it was shown by mass-spectrometry[12]. Both Be_2 and BeOBe were extensively studied previously with gas-phase spectroscopy techniques[5-7,9,11] and the results are in good agreement with highest level computation studies[5,11,13-15]. High level *ab initio* calculations were performed on the Be_2^+ and $BeOBe^+$ cations; however no experimental studies of them existed until this work.

Several high-level theory calculations[16-18] were performed on the ground and excited states of BeC. Different *ab initio* calculations predicted a ground state of either triplet or quintet multiplicity. No spectroscopic studies existed to test the theoretical predictions prior to this study. The ionization energy (IE) of both species was measured and properties of the Be_2^+ and $BeOBe^+$ cations were predicted[5,6,11]. However, no direct experimental studies were done until this work.

Chapters II and III of this thesis describe studies of the Be_2^+ and $BeOBe^+$ cations that utilized the pulsed field ionization – zero electron kinetic energy (PFI-ZEKE)[19] technique. Spectroscopic constants of the ground electronic states were obtained and compared to theoretical predictions. The IE values of Be_2 and BeOBe were measured with better accuracy. Chapter IV describes studies of BeC using resonantly enhanced multi-photon ionization (REMPI) and photo-ionization efficiency (PIE) techniques. Erratic pattern of vibronic levels were observed and explained using high level *ab initio* calculations. The IE of BeC was measured and ground state term symbol was determined.

The HfS molecule is interesting because it was proposed to exist in cold stars[20]. It has been studied previously by several research groups with various spectroscopic methods[21-24]. The HfS^+ cation has not been studied before, however gas-phase spectroscopy studies on isoelectronic species such as HfO^+ and ThO^+ are available[25,26]. Interestingly, in both HfO^+ and ThO^+ metal-oxygen bond is weaker but stiffer then in the neutral molecules. No data was available on ThS and ThS^+. Studying HfS^+ may facilitate ThS^+ study in future and advance understanding of bonding in actinide-sulfur compounds.

Chapter V of this thesis describes study of HfS^+ cation with PFI-ZEKE technique. The spectrum of HfS^+ was recorded in the range 0 to 9600 cm^{-1} above the ionic ground state. The ground and two electronically excited states were observed and assigned as $^2\Sigma^+$, $^2\Delta_{3/2}$ and $^2\Delta_{5/2}$ respectively. *Ab initio* calculations were performed and the results were in good agreement with the observations. The IE value of HfS was measured and the dissociation energy of HfS^+ was shown by thermodynamic considerations to be lower than that of HfS. Interestingly, despite having weaker bond, the vibration frequency of the cation is higher and bond length is shorter than in the neutral HfS. Corresponding trends were observed previously for ThO/ThO^+ and HfO/HfO^+[25,26].

Thorium and hafnium fluorides are species of interest for the fundamental physics community. Recently, it was suggested that the electric dipole moment of the electron (eEDM)

can be measured in a heavy diatomic molecule polarized by an external electric field[27,28]. The best molecule for such measurements should possess a long-lived $^3\Delta_1$ state derived from an $ns^1(n-1)d^1$ outer shell configuration of the metal center. The heavy metal is needed as it allows for stronger internal field upon polarization. HfF^+ and ThF^+ cations are predicted to have such states and could be polarized using modest fields[29] to generate intramolecular fields of 30 and 90 GV/cm respectively. The energy level structures and lifetimes of the excited states in HfF^+ and ThF^+ were predicted with *ab initio* methods to be sufficient for eEDM measurement[28]. However, no direct confirmation could be found as no spectroscopy data existed for either of these cations prior to the studies reported here.

In Chapter VI of this work, studies of HfF^+, ThF and ThF^+ are reported. Both HfF^+ and ThF^+ were shown to be suitable for eEDM measurements. In HfF^+ the $^3\Delta_1$ ($6s^15d^1$) state was found at lower energy as compared to *ab initio* calculations, and its lifetime was longer than *ab initio* estimates. In ThF^+ the assignment of the first excited state was unclear and $^3\Delta_1$ is either ground or first excited state. In both cases, the molecule is suitable for eEDM studies. The IE's of both HfF and ThF were measured with high accuracy.

Uranium diatomic molecules are model systems that may be used to investigate the bonding in actinide species. The isoelectronic UF and UH molecules were studied previously using high level *ab initio* calculations[30,31]. These molecules are also model systems that can be used to test the applicability of ligand field theory (LFT) for actinides. The degree to which the 5f electrons participate in bonding is one of the most intriguing questions in actinide chemistry[32]. In actinides, the 5f orbitals extend much further from the atom center compared to 4f electrons of lanthanides[33]. It is well-known that 4f subshell in lanthanide compounds can be treated as metal-centered nonbonding electrons. Mainly due to this fact, LFT is a very effective tool for predicting spectral properties of lanthanide molecules[34]. It was shown that LFT cannot be directly applied to actinide species in the same way as to lanthanide species[32,35]. However the LFT integrals were treated as fit parameters and used to explain the observed energy level patterns in UO[10,35] and

UO^{+36}. The next question is whether the change of ligand will affect the applicability of LFT to actinide species.

In Chapter VII, the first gas-phase spectroscopic studies of UF and UF^+ are described. In UF the ground state and 2 electronically excited states in the 18000-20000 cm^{-1} energy range were studied using LIF. The dispersed fluorescence technique was used to probe low-lying electronic states of UF. The IE was measured with high accuracy and corrected the previous value obtained with electron impact technique. The electronic structure of UF^+ was studied using the PFI-ZEKE technique. More than 50 vibronic levels belonging to 16 electronic states were found. *Ab initio* calculations were used to explain the observed electronic structure. The calculated energies of electronic levels were in good agreement with the experimental measurements. The observed patterns of electronic levels of UF^+ were very similar to those of the isoelectronic UO molecule and suggested that the LFT model is applicable to uranium diatomic species with ionic bonds.

REFERENCES

(1) Dolg, M.; Cao, X. Y. *Chemical Reviews* **2012**, *112*, 403-480.

(2) Gagliardi, L. *International Journal of Quantum Chemistry* **2011**, *111*, 3302-3306.

(3) Eliav, E.; Kaldor, U. In *Recent Progress in Coupled Cluster Methods: Theory and Applications*; Carsky, P., Paldus, J., Pittner, J., Eds.; Springer: Dordrecht, 2010; Vol. 11, p 113-144.

(4) Jensen, F. *Introduction to computational chemistry*; 2nd ed.; John Wiley & Sons: Chichester, England ; Hoboken, NJ, 2007.

(5) Merritt, J. M.; Bondybey, V. E.; Heaven, M. C. *J. Phys. Chem. A* **2009**, *113*, 13300-13309.

(6) Merritt, J. M.; Bondybey, V. E.; Heaven, M. C. *Science (Washington, DC, U. S.)* **2009**, *324*, 1548-1551.

(7) Bondybey, V. E. *Chem. Phys. Lett.* **1984**, *109*, 436-41.

(8) Bondybey, V. E. *Science* **1985**, *227*, 125-131.

(9) Bondybey, V. E.; English, J. H. *J. Chem. Phys.* **1984**, *80*, 568-70.

(10) Kaledin, L. A.; Kaledin, A. L.; Heaven, M. C.; Bondybey, V. E. *Theochem* **1999**, *461-462*, 177-186.

(11) Merritt, J. M.; Kaledin, A. L.; Bondybey, V. E.; Heaven, M. C. *Phys. Chem. Chem. Phys.* **2008**, *10*, 4006-4013.

(12) Theard, L. P.; Hildenbrand, D. L. *J. Chem. Phys.* **1964**, *41*, 3416-20.

(13) Meng, B.; Bruna, P. J.; Wright, J. S. *Mol. Phys.* **1993**, *79*, 1305-25.

(14) Fischer, I.; Bondybey, V. E.; Rosmus, P.; Werner, H. J. *Chem. Phys.* **1991**, *151*, 295-308.

(15) Hogreve, H. *Chem. Phys. Lett.* **1991**, *187*, 479-486.
(16) Borin, A. C.; Ornellas, F. R. *J. Chem. Phys.* **1993**, *98*, 8761-9.
(17) Borin, A. C.; Ornellas, F. R. *Chem. Phys.* **1994**, *184*, 59-66.
(18) Wright, J. S.; Kolbuszewski, M. *J. Chem. Phys.* **1993**, *98*, 9725-33.
(19) Muller-Dethlefs, K., Schlag, K. *Ann. Rev. Phys. chem.* **1991**, *42*, 109-136.
(20) Bernath, P. F. *International Reviews in Physical Chemistry* **2009**, *28*, 681-709.
(21) Launila, O.; Jonsson, J.; Edvinsson, G.; Taklif, A. G. *Journal of Molecular Spectroscopy* **1996**, *177*, 221-231.
(22) Callender, C. L.; Hackett, P. A.; Rayner, D. M. *Journal of the Optical Society of America B-Optical Physics* **1988**, *5*, 1341-1342.
(23) Cooke, S. A.; Gerry, M. C. L. *Journal of Molecular Spectroscopy* **2002**, *216*, 122-130.
(24) Jonsson, J.; Edvinsson, G.; Taklif, A. G. *Physica Scripta* **1994**, *50*, 661-665.
(25) Goncharov, V.; Heaven, M. C. *Journal of Chemical Physics* **2006**, *124*, 7.
(26) Merritt, J. M.; Bondybey, V. E.; Heaven, M. C. *Journal of Chemical Physics* **2009**, *130*, 9.
(27) Meyer, E. R.; Bohn, J. L. *Phys. Rev. A At., Mol., Opt. Phys.* **2008**, *78*, 010502/1-010502/4.
(28) Petrov, A. N.; Mosyagin, N. S.; Titov, A. V. *Phys. Rev. A At., Mol., Opt. Phys.* **2009**, *79*, 012505/1-012505/7.
(29) Leanhardt, A. E.; Bohn, J. L.; Loh, H.; Maletinsky, P.; Meyer, E. R.; Sinclair, L. C.; Stutz, R. P.; Cornell, E. A. *J. Mol. Spectrosc.* **2011**, *270*, 1-25.
(30) Dolg, M.; Cao, X. Y. *Journal of Physical Chemistry A* **2009**, *113*, 12573-12581.
(31) Fedorov, D. G.; Nakajima, T.; Hirao, K. *Journal of Chemical Physics* **2003**, *118*, 4970-4975.
(32) Kaledin, L. A.; McCord, J. E.; Heaven, M. C. *Journal of Molecular Spectroscopy* **1994**, *164*, 27-65.
(33) Edelstein, N. *J. Alloy. Comp.* **1995**, *197*, 223.
(34) Field, R. W. *Ber. Bunsenges. Phys. Chem.* **1982**, *86*, 771.
(35) Kaledin, L. A.; Heaven, M. C. *Journal of Molecular Spectroscopy* **1997**, *185*, 1-7.
(36) Goncharov, V.; Kaledin, L. A.; Heaven, M. C. *Journal of Chemical Physics* **2006**, *125*, 8.

CHAPTER II
SPECTROSCOPIC CHARACTERIZATION OF Be_2^+ X $^2\Sigma_u^+$ AND THE IONIZATION ENERGY OF Be_2

II.1 INTRODUCTION

As beryllium is a closed-shell atom, application of the simplest molecular orbital theory to the Be_2 dimer predicts an unstable molecule with a formal bond order of zero. However, spectroscopic observations show that the molecule is weakly bound[1-6], with a surprisingly short equilibrium bond distance of 2.45 Å. Due to this unusual circumstance, Be_2 has been the subject of numerous theoretical studies[7-17]. A detailed experimental study that yielded an accurate dissociation energy has only recently been published[5,18].

The first ionization energy (IE) of Be_2 is expected to correlate with the removal of an electron from the 2*s* σ_u antibonding orbital, resulting in a $X^2\Sigma_u^+$ ground state ion with a bond order of 1/2. High level theoretical calculations predict that the ion is bound by approximately 2 eV[6,19-21]. Our previous experimental photoionization efficiency (PIE) studies of the beryllium dimer have clearly confirmed the presence of a substantial bond for the Be_2^+ cation and provided approximate values for some of its properties.[6] The ionization threshold, combined with the known ionization energy of Be atom and the previously available estimate for the bond energy of $Be_2(X)$, defined a bond dissociation energy of D_0^+=16072(40) cm^{-1} (2.07 eV)[6] for Be_2^+. An analysis of the auto-ionizing Rydberg structure observed above the ionization threshold yielded an estimate for the vibrational frequency for Be_2^+ of $\omega_e^+ = 498(20)$ cm^{-1}.

The objective of the present study was to improve the characterization of Be_2^+ by applying a two-color pulsed field ionization zero kinetic energy (PFI-ZEKE) photoelectron technique. We have obtained rotationally resolved data for the vibrational levels v^+=0-6, whose analysis confirmed the $^2\Sigma_u^+$ symmetry for the ground state and yielded vibration-rotation

constants. The ionization energy determination, which represents a significant improvement over that achieved using direct photoionization, combined with the most recent value for the bond dissociation energy of Be_2, establishes a more accurate value for the bond energy of Be_2^+.

II.2 EXPERIMENTAL

The sequential excitation scheme used to record resonantly enhanced multiphoton ionization (REMPI) and PFI-ZEKE spectra for Be_2 is illustrated in Fig. II.1. The experimental apparatus used for this study is shown on Fig. II.2. The setup consisted of two differentially pumped vacuum chambers. The pulsed laser vaporization source was located in the first chamber evacuated by a 10″ diffusion pump (Varian VHS-10). The focused output of a Nd/YAG laser (Continuum Minilite II, operating at ~20 mJ) was used to ablate the surface of a beryllium rod that was continuously rotated and translated to expose a fresh surface for each laser shot. A pulsed solenoid valve (Parker-Hannifin, Series 9, 0.8 mm nozzle diameter) was used to entrain the ablated vapor in helium carrier gas. The formation of Be_2 molecules in the ablation source was facilitated by optimizing the backing pressure and pulse duration of the solenoid valve and the power and the timing of the ablation laser relative to the solenoid valve. A digital delay generator (Stanford Research Systems, model DG-535) was used to adjust timing of the solenoid valve and the ablation laser. The stagnation pressure and pulse duration of the solenoid valve were typically 5.0 bar and 200 μs respectively.

The pressure in the source chamber was in the order of 10^{-4} torr when the pulsed valve operated. The gas pulse formed a supersonic expansion and effectively cooled the ablated molecules. Few centimeters downstream the ablation source the gas pressure decreased significantly and the gas pulse propagated as a free-jet expansion. Approximately 5 cm after the source the expansion was crossed by a laser beam and laser induced fluorescence (LIF) was collected by a set of optics and detected by a Photonis XP 2020 photomultiplier tube. LIF

excitation spectrum is recorded by scanning the wavelength of the probe laser. For dispersed fluorescence (DF) the light was focused on the entrance slit of a 0.25 m Ebert monochromator (Jarrell-Ash model 82-410, 1180 line/mm grating, 0.7 mm slit width) prior to detection. DF spectrum was recorded by scanning the wavelength of the monochromator. Scattered light was reduced by placing baffles on the entrance and exit windows and using long-pass filters in front of the photomultiplier tube.

Conical skimmer with a 5 mm diameter orifice was used to transmit the core of the free-jet expansion into a second differentially pumped chamber that housed a time-of-flight (TOF) mass spectrometer and the components for REMPI and PFI-ZEKE detection. The second chamber was evacuated by a turbomolecular pump (Seiko Seiki STP-400). The pressure in the second chamber was typically in the order of 10^{-7}-10^{-8} torr depending on the gas load in the first chamber.

Two independent Nd/YAG pumped dye lasers (Coherent Scanmate Pro and a Continuum ND6000) were used for excitation in LIF, REMPI and PFI-ZEKE techniques. The LIF and REMPI spectra typically displayed a resolution of ~0.15 cm^{-1}. When higher resolution was need a Fabri-Perot etalon could be installed in the resonator of the ScanMate Pro laser. The spectra taken with the etalon displayed a resolution of about 0.05 cm^{-1}. Spectral intensities were not corrected for variations in the laser output power. Wavelength calibration was achieved using an I_2 reference cell where the fundamental outputs from the dye lasers were used to observe the B-X bands. Absolute calibrations were good to ±0.1 cm^{-1}. When the laser wavelength was outside the range of I_2 B-X system calibrations were made by atomic lines of Fe, Ti and other metals found in the source. The calibrations by atomic lines are expected to be good to ±0.5 cm^{-1}. The monochromator was calibrated by emission lines of a Hg lamp. Band centers for DF data were good to ±15 cm^{-1}.

The digital delay generator was used to trigger the experiment at 10 Hz, temporally overlap the two laser pulses, and to have them coincide with the arrival time of Be_2 in the

molecular beam. The two counter propagating laser beams were overlapped in the ionization region of the TOF spectrometer, along an axis that was perpendicular to the molecular beam and the flight tube. The flight path of the mass spectrometer was 50 cm and the repeller and extractor plates were held at +1880 V and +1530 V. REMPI spectra were recorded to verify that the first laser was tuned into resonance with a specific ro-vibronic line of the B-X transition[1,6]. The Be_2^+ ions produced in sequential ionization with REMPI technique were detected by a microchannel plate located at the end of the flight tube above the TOF mass spectrometer accelerator plate.

For PFI-ZEKE detection both the extractor and repeller plates were held at -5.1 V during photoexcitation, providing field free conditions inside the excitation region. After a delay of 1.7 μs, which was needed to allow for the direct electrons to exit the detection zone, the voltage on the lower plate was lowered to effect pulsed field ionization of high-*n* Rydberg states, and acceleration of the electrons towards the detector. A pulsed field of 1.43 V cm^{-1} was used for the recording of PFI-ZEKE spectra. A smaller field of 0.36 V cm^{-1} was applied to measure the ionization energy using the blue edge of the $v^+ = 0$, J^+=0 feature. The delayed photoelectrons produced when PFI-ZEKE technique was applied were detected by a microchannel plate located 10 cm below the TOF mass spectrometer repeller plate. The current on both REMPI and PFI-ZEKE microchannel plates was amplified by fast preamplifier (Ortec VT120A) and recorded with a digital oscilloscope (Tektronix TDS 2012). A program written with Labview 7.0 package was used to control the wavelength of the lasers, acquire and integrate the signal from the oscilloscope and store the data on a computer.

II.3 RESULTS AND ANALYSIS

In the initial series of PFI-ZEKE measurements the first laser excited the Be_2 B-X 2-0 transition. Rotationally resolved REMPI spectra for this band exhibited rotational population distributions that were consistent with a local temperature of approximately 4 K. Fig. II.3 shows a broad scan of the PFI-ZEKE spectrum, taken with the first laser tuned to the R(1) rotational line. The energy scale for this trace is that of the second photon. The three bands in Fig. II.3 correspond to the ionization limits for the v^+=0, 1 and 2 levels. Fig. II.4 shows the rotational structure of the v^+=1 band obtained with initial excitation of the R(1) and R(2) lines. Note that only even rotational lines were observed for excitation of R(1), while odd rotational lines were seen for R(2). This is due to the conservation of nuclear spin symmetry. Excitation of the B-X 3-0 and 6-0 bands was used to probe higher energy vibrational levels of the ion (v^+=2-6).

An ionization energy of IE_0=59824(2) cm^{-1} was obtained from multiple determinations of the blue edge of the $v^+ = 0$, J^+=0 feature, recorded using the R(1) line for intermediate state excitation. The energy given here was referenced to the Be_2(X) v=0, J=0 level by adding the ground state rotational energy (E(J=1)=1.22 cm^{-1})[1] to the observed transition energy ($hv_1 + hv_2$).

The vibrational energy level spacings for Be_2^+ were determined using the line centers of the J^+=0 features. The line centers were obtained by fitting Gaussian functions to the spectra. Table II. 1 lists the vibrational energies for v^+=1-6, determined relative to v^+=0. Fitting the polynomial

$$G(v^+) = \omega_e^+ v^+ - \omega_e x_e^+ v^+ \left(v^+ + 1\right) \qquad (1)$$

to the energies of Table II. 1 yielded the vibrational constants ω_e^+=525.88(12) and $\omega_e x_e^+$=4.44(2), where the standard deviations from the regression are given in parenthesis. A fit that included the cubic anharmonicity term yielded a value for $\omega_e y_e^+$ that was statistically insignificant.

Rotational constants were obtained by fitting the rigid rotor energy level expression, $E(J^+) = B_v^+ J^+(J^+ + 1)$ to the energy level spacings. The results are collected in Table II. 1. Fitting these data to the expression

$$B_v^+ = B_e^+ - \alpha_e^+(v^+ + 1/2) \qquad (3)$$

yielded B_e^+=0.765(3) and α_e^+=0.0103(8).

II.4 DISCUSSION

The observed rotational angular momentum selection rules, which are dictated by conservation of the nuclear spin symmetry, confirm that the ground state of Be_2^+ is $X^2\Sigma_u^+$ (odd rotational levels of $Be_2(X)$ ionize to even rotational levels of $Be_2^+(X)$ and vice versa).

The ionization energy obtained from the PFI-ZEKE measurements (59824(2) cm^{-1}) is in good agreement with the previous PIE determination (59828(40) cm^{-1})[6], while the uncertainty range is reduced by a factor of 20. With this improvement it is pertinent to revisit that dissociation energy of Be_2^+ using the new ionization energy and recently revised value for the dissociation energy of $Be_2(X)$ (D_0=807.4 cm^{-1})[5]. The dissociation energy of the ion is given by

$$D_0^+ = IE(Be) + D_0 - IE_0(Be_2) \qquad (3)$$

which, for IE(Be)=75192.0 cm^{-1} (ref. [22]) gives D_0^+=16175(5) cm^{-1}. This value is 103 cm^{-1} higher than the previous estimate.

The vibration-rotation constants for Be_2^+ indicate that the potential energy curve, for the energy range examined, is close in form to the Morse approximation. To further illustrate this point, the Rydberg-Kliein-Rees (RKR) turning points were calculated from the ro-vibrational constants. The results are listed in Table II. 2 and plotted in Fig. II.5. The smooth curve in this figure is a Morse potential that was fitted to the RKR turning points, with D_e^+ constrained to the

experimentally determined value of 16438 cm^{-1}. The equilibrium distance determined by the RKR inversion was R_e^+=2.211 Å.

Recent *ab initio* theoretical calculations for Be_2^+ are found to be in respectable agreement with the present measurements. Table II. 3 lists representative theoretical results for comparison. Density functional methods have also been used to examine Be_2^+. The local spin density calculations of Kolchin and Hall[23] predict a dissociation energy of D_e^+=17600 cm^{-1} and an equilibrium distance of R_e^+=2.24 Å. Srinivas and Jellinek[13] used a gradient corrected DFT model (BPW91) with a Pople style basis set (631/31). They obtained a bond dissociation energy of D_e^+ =19200 cm^{-1}, an equilibrium distance of R_e^+=2.21 Å, and an IE_e of 55330 cm^{-1}. While these results are not of the same quality as those obtained from large-scale MRDCI calculations, it is clear that DFT yields reasonable results for the dimer ion, and its value for further studies of larger clusters is supported by the comparison with the experimental data.

Be_2^+ is isoelectronic with LiBe and Li_2^-. Spectra have been recorded for LiBe[24], and MRCI calculations[25-27] indicate a binding energy of 2420 cm^{-1}. Bauschlicher et al.[27] analyzed the nature of the LiBe bond and concluded that it is mostly due to the dispersion interaction. They note that "the LiBe bonding orbital is basically 2s+2s with very little 2p character and is localized primarily on the Be atom (86%)." As the spectra for LiBe provided data for just the lowest vibrational levels of the ground state (v=0 and 1), the theoretical prediction has yet to be tested. Li_2^- is also found to be appreciably less strongly bound than Be_2^+. Hogreve[28] predicted a bond energy of 7315 cm^{-1}, which is surprisingly close to that of neutral Li_2 (8516 cm^{-1}). Hence, the strength of the Be_2^+ bond appears to be uniquely high for this isoelectronic group. The stronger bond for Be_2^+, as compared to LiBe, appears to be largely due to the degeneracy of the atomic orbitals of the former. The reasons for the weaker bond for Li_2^- are more difficult to discern. Correlation effects are particularly important in the bonding of Be_2^+, where doubly excited

configurations make significant contributions to the stability of the ground state. Meng et al.[29] have also drawn attention to the fact that Be_2^+ will possess strongly bound doubly excited states that are yet to be observed.

REFERENCES

(1) Bondybey, V. E. *Chem. Phys. Lett.* **1984**, *109*, 436-41.

(2) Bondybey, V. E. *Science* **1985**, *227*, 125-131.

(3) Bondybey, V. E.; English, J. H. *J. Chem. Phys.* **1984**, *80*, 568-70.

(4) Kaledin, L. A.; Kaledin, A. L.; Heaven, M. C.; Bondybey, V. E. *Theochem* **1999**, *461-462*, 177-186.

(5) Merritt, J. M.; Bondybey, V. E.; Heaven, M. C. *Science (Washington, DC, U. S.)* **2009**, *324*, 1548-1551.

(6) Merritt, J. M.; Kaledin, A. L.; Bondybey, V. E.; Heaven, M. C. *Phys. Chem. Chem. Phys.* **2008**, *10*, 4006-4013.

(7) Harrison, R. J.; Handy, N. C. *Chem. Phys. Lett.* **1983**, *98*, 97-101.

(8) Petersson, G. A.; Shirley, W. A. *Chem. Phys. Lett.* **1989**, *160*, 494-501.

(9) Evangelisti, S.; Bendazzoli, G. L.; Gagliardi, L. *Chem. Phys.* **1994**, *185*, 47-56.

(10) Martin, J. M. L. *Chem. Phys. Lett.* **1999**, *303*, 399-407.

(11) Roeeggen, I.; Almlof, J. *Int. J. Quantum Chem.* **1996**, *60*, 453-466.

(12) Spirko, V. *J. Mol. Spectrosc.* **2006**, *235*, 268-270.

(13) Srinivas, S.; Jellinek, J. *J. Chem. Phys.* **2004**, *121*, 7243-7252.

(14) Anderson, A. G.; Goddard, W. A. i. *J. Chem. Phys.*, *132*, 164110/1-164110/13.

(15) Bytautas, L.; Matsunaga, N.; Ruedenberg, K. *J. Chem. Phys.*, *132*, 074307/1-074307/15.

(16) Nguyen, H.-V.; Galli, G. *J. Chem. Phys.*, *132*, 044109/1-044109/8.

(17) Patkowski, K.; Spirko, V.; Szalewicz, K. *Science (Washington, DC, U. S.)* **2009**, *326*, 1382-1384.

(18) Bernath, P. F. *Science (Washington, DC, U. S.)* **2009**, *324*, 1526-1527.

(19) Meng, B.; Bruna, P. J.; Wright, J. S. *Mol. Phys.* **1993**, *79*, 1305-25.

(20) Hogreve, H. *Chem. Phys. Lett.* **1991**, *187*, 479-486.

(21) Fischer, I.; Bondybey, V. E.; Rosmus, P.; Werner, H. J. *Chem. Phys.* **1991**, *151*, 295-308.

(22) Linde, D. R. *Ionization potentials of atoms and atomic ions*, 1992.

(23) Kolchin, A. M.; Hall, R. W. *J. Chem. Phys.* **2000**, *113*, 4083-4092.

(24) Schlachta, R.; Fischer, I.; Rosmus, P.; Bondybey, V. E. *Chem. Phys. Lett.* **1990**, *170*, 485-91.

(25) Fischer, I.; Bondybey, V. E.; Rosmus, P.; Werner, H. J. *Chem. Phys.* **1991**, *151*, 295-308.

(26) Pak, K.; Ermler, W. C.; Kern, C. W.; Bondybey, V. E. *J. Cluster Sci.* **1991**, *2*, 19-28.

(27) Bauschlicher, C. W., Jr.; Langhoff, S. R.; Partridge, H. *J. Chem. Phys.* **1992**, *96*, 1240.

(28) Hogreve, H. *Eur. Phys. J. D* **2000**, *8*, 85-91.

(29) Meng, B.; Bruna, P. J.; Wright, J. S. *Mol. Phys.* **1993**, *79*, 1305-25.

Table II.1. Vibrational energies and rotational constants for $Be_2^+ \ X^2\Sigma_u^+$

v	E[a]/ cm^{-1}	Residual[b]	B_v[c] /cm^{-1}
0	0.0	-0.05	0.762
1	517.0	-0.03	0.753
2	1024.7	0.33	0.732
3	1524.6	-0.30	0.729
4	2014.7	0.00	0.717
5	2496.1	0.05	0.711
6	2968.8	0.00	0.699

[a.] Energy relative to the zero point level. Error limits (1σ) are 0.5 cm^{-1}

[b.] Residuals (cm^{-1}) for the fit of Eq. 1 to the vibrational energies.

[c.] Error limits (1σ) are 0.005 cm^{-1}

Table II.2. RKR turning points for $Be_2^+ \ X^2\Sigma_u^+$

v^+	E calc. (cm^{-1})	R^- (Å)	R^+ (Å)
0	261.95	2.100	2.339
1	778.95	2.027	2.445
2	1287.07	1.982	2.525
3	1786.31	1.947	2.594
4	2276.67	1.918	2.657
5	2758.15	1.893	2.717
6	3230.75	1.872	2.775
7	3694.47	1.853	2.830
8	4149.31	1.836	2.885

Table II.3. Comparison of measured and calculated spectroscopic constants for Be_2^+ $X^2\Sigma_u^+$

	Expt.[a]	Merritt et al.[b]	Fischer et al.[c]	Hogreve[d]	Meng et al.[e]	Srinivas and Jellinek[f]
D_e^+	16438(5)	16684	15889	16212	15646	19200
ω_e^+	524.88(12)	-	502	-	513	-
$\omega_e x_e^+$	4.44(2)	-	4.2	-	4.2	-
$\Delta G_{1/2}^+$	517.0(5)	516.0	494	503.6	505	-
R_e^+ (Å)	2.211(8)	2.211	2.231	2.236	2.249	2.21
IE_e	59685(2)	59540	-	-	60090	55330

[a.] Constants are in units of cm^{-1}, with the exception of R_e^+.

[b.] RCCSD(T) calculation with the cc-pV5Z basis set. Ref. [6]

[c.] MRCI calculation with a (11s,6p,4d,2f)/[8s,6p,4d,2f] basis set. Ref. [21]

[d.] MRDCI calculation with a (13s,5p,2d)/[8s,5p,2d] basis set. Ref. [20]

[e.] MRDCI calculation with a (11s,6p,3d)/[6s,4p,3d] basis set. Ref. [29]

f. DFT calculations (BPW91) with a 631/31 basis set. Ref. [13]

Figure II.1. Two-color excitation scheme used for observation of the PFI-ZEKE spectrum of Be_2.

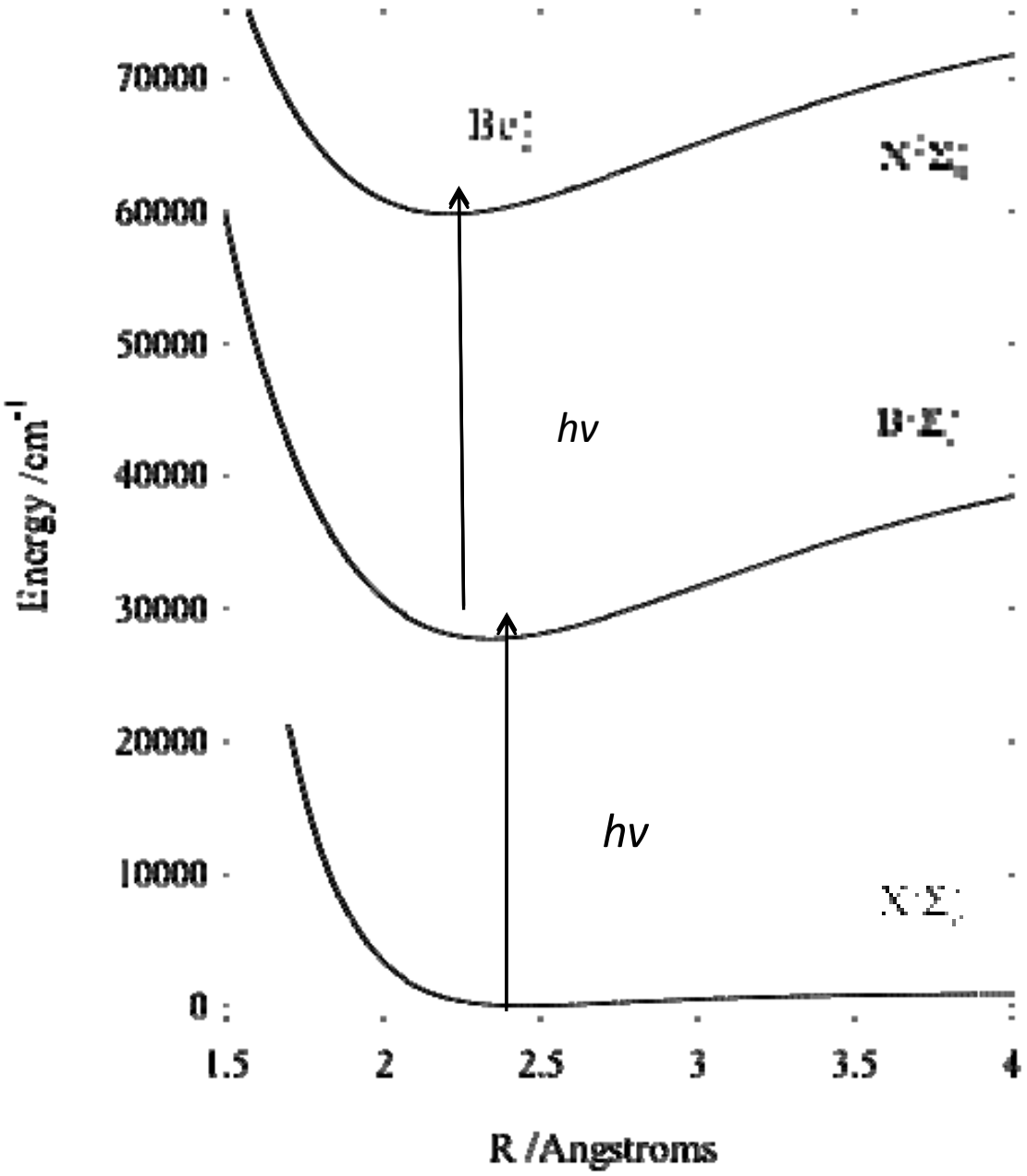

Figure II.2. Diagram of PFI-ZEKE spectrometer.

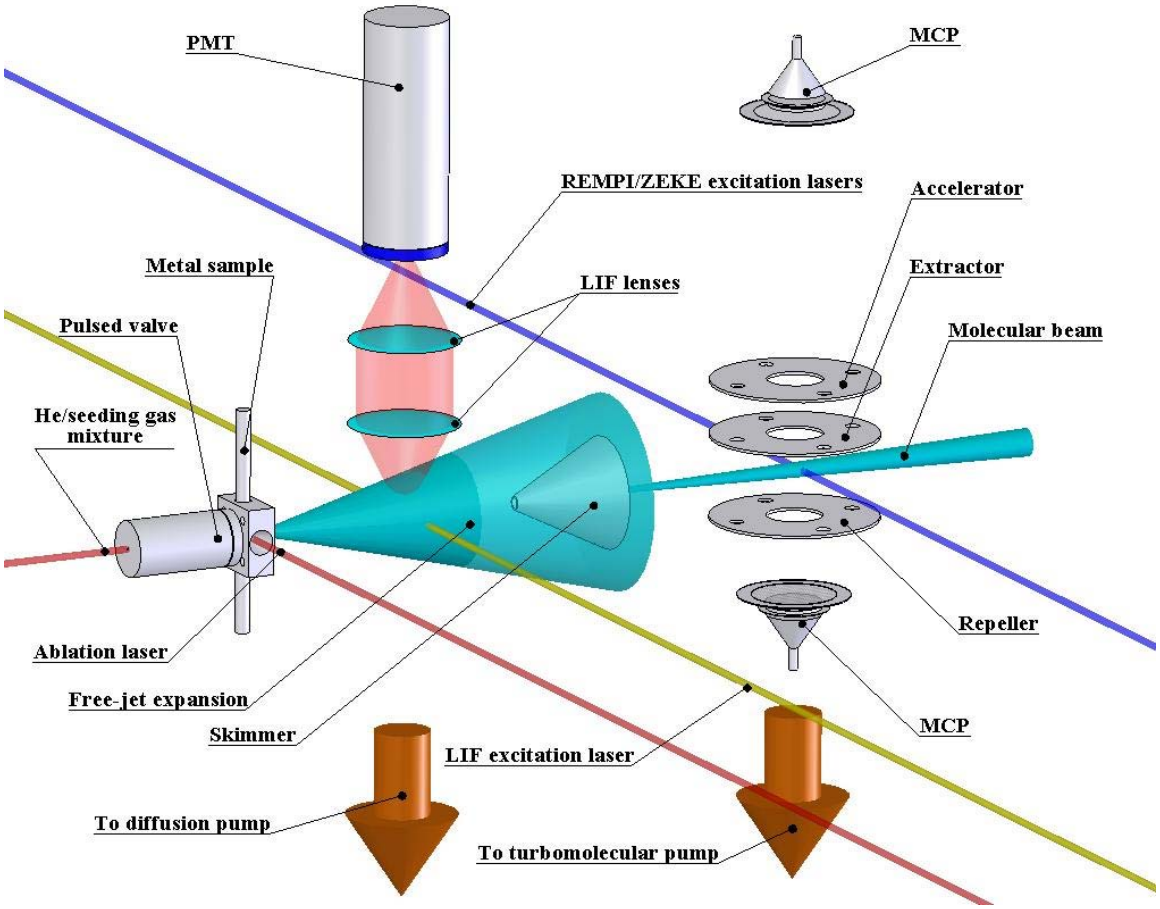

Figure II.3. Survey spectrum showing the v^+=0, 1, and 2 bands of Be_2^+.

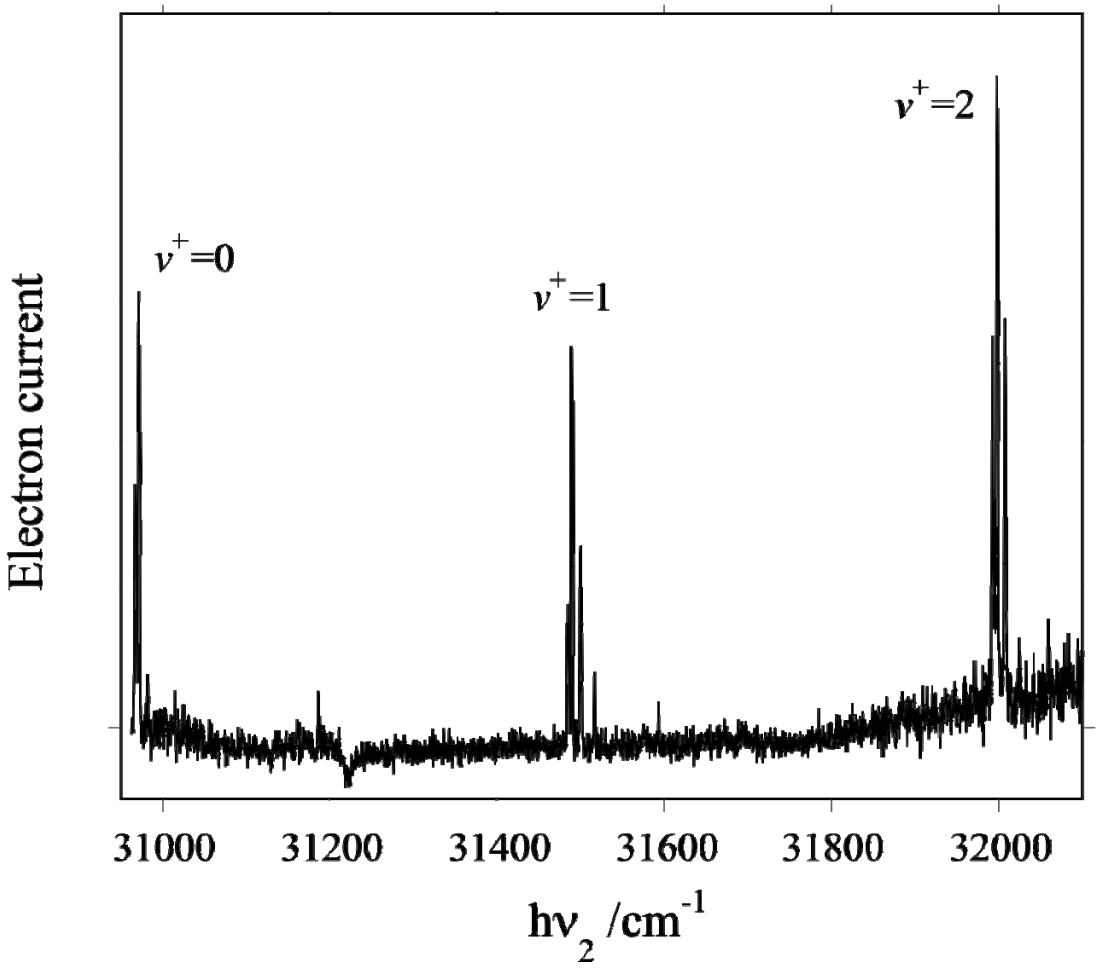

Figure II.4. Rotationally resolved PFI-ZEKE spectra for the v^+=1 band of Be_2^+.

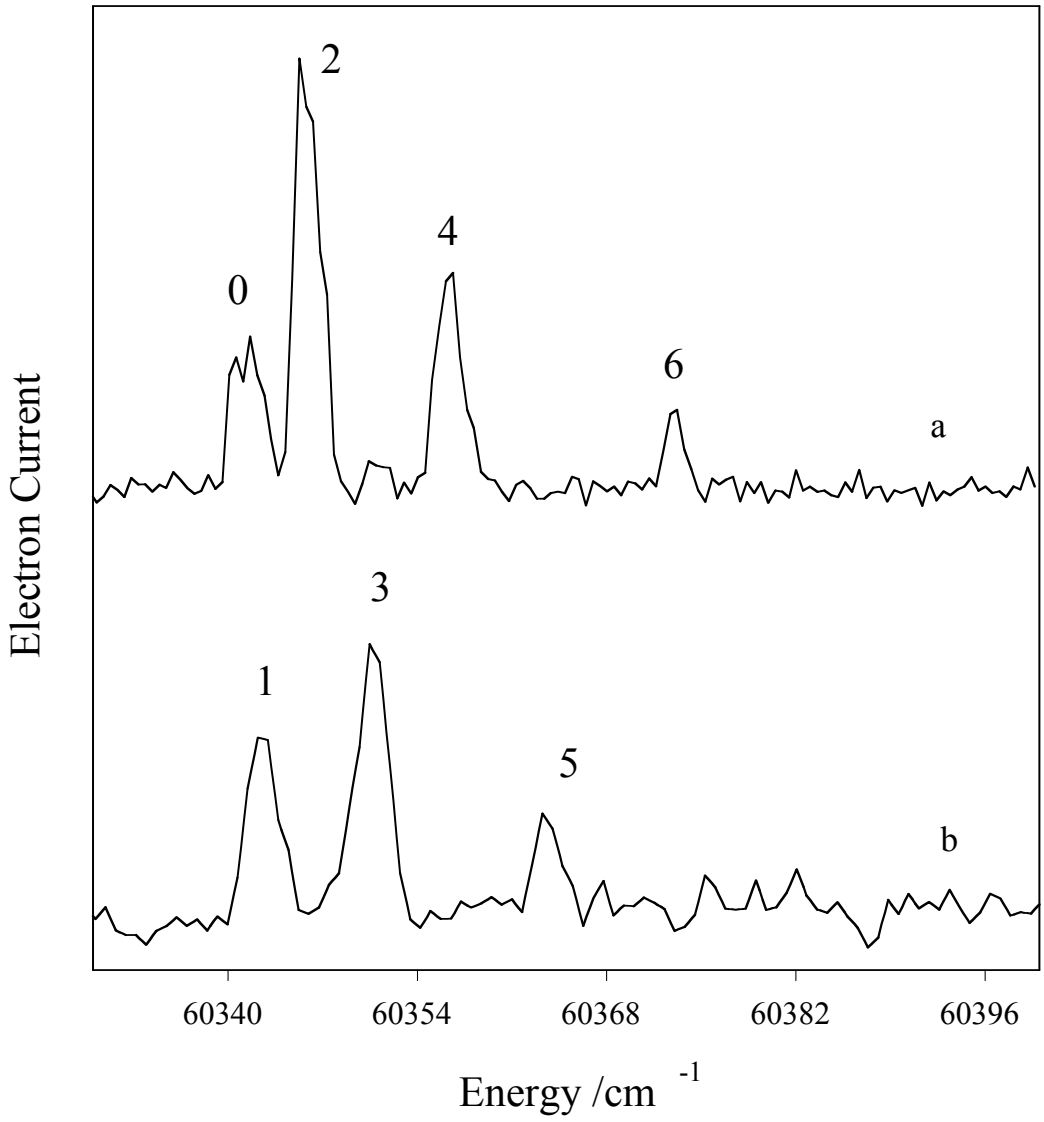

These spectra were recorded with hν_1 set to excited the B-X 2-0 band lines R(1) (trace a) and R(2) (trace (b)). The numbers given next to each line are the J^+ values. The energy scale is relative to the v=0, J=0 level of Be_2 X.

Figure II.5. RKR turning points for the ground state of Be_2^+ (solid circles) and a fitted Morse potential energy function (smooth line).

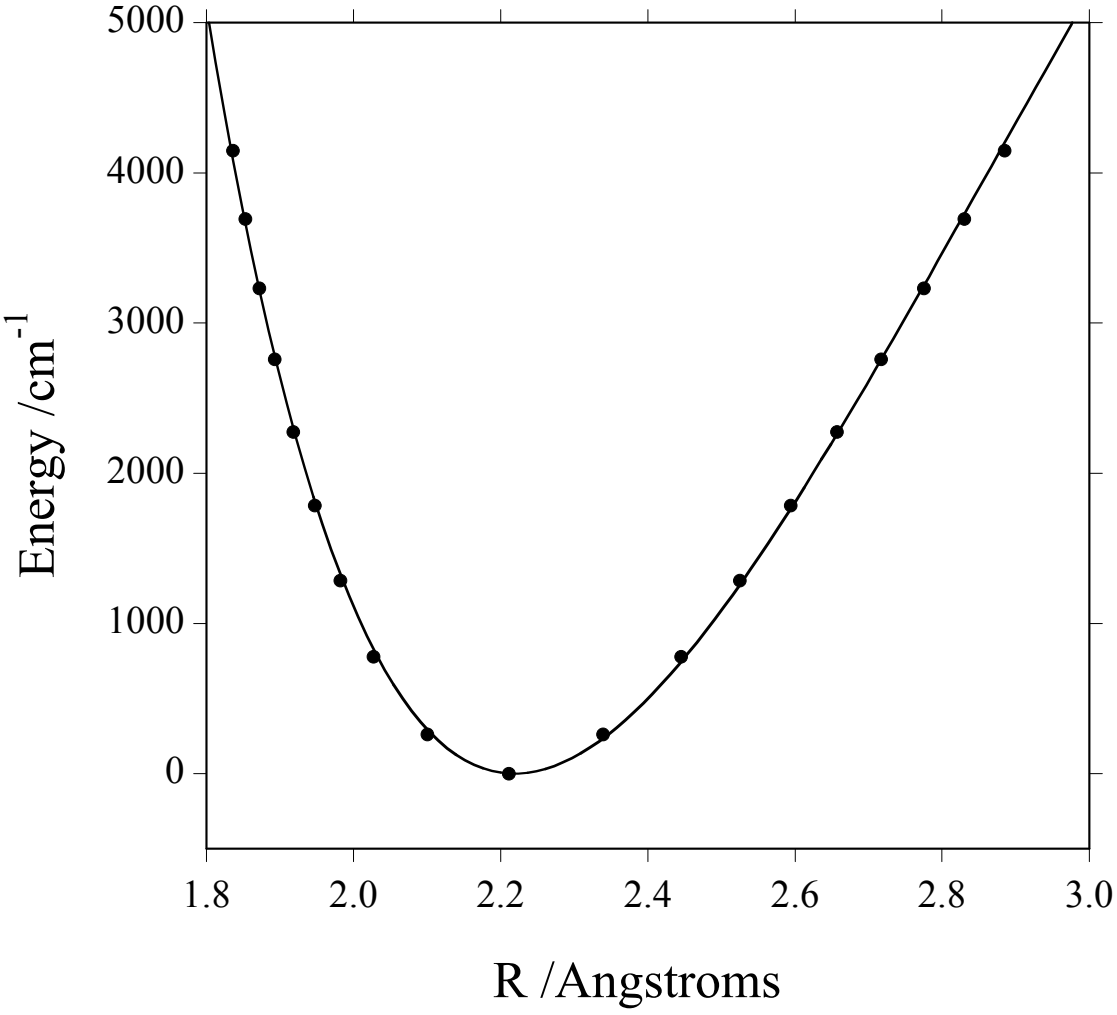

CHAPTER III

PFI-ZEKE SPECTRUM OF THE GROUND ELECTRONIC STATE OF $BEOBE^+$

III.1 INTRODUCTION

Neutral BeOBe has been studied both experimentally[1-4] and theoretically[3-6]. The molecule was first detected in a Knudsen-cell mass spectrometry experiment[1]. Later BeOBe was examined in matrix isolation experiments by Andrews and co-workers, who observed the infrared absorption band for the anti-symmetric stretch[3]. *Ab initio* calculations performed at the MP2 level of theory predicted a $^3\Sigma_u^+$ symmetry ground state for BeOBe[3]. However, Boldyrev and Simons[5] found that higher level calculations (quadratic configuration interaction with single, double and perturbative triple excitations) yielded a $^1\Sigma_g^+$ ground state that was markedly multi-reference in character. Roughly speaking, the bonding in BeOBe can be viewed as the donation of an electron from each of the Be atoms, resulting in the formal structure $Be^+O^{2-}Be^+$. The valence molecular orbitals that are responsible for the multi-reference character of the singlet state are the non-bonding linear combinations of the Be 2*s* orbitals[4-6], $4\sigma_g = 1/\sqrt{2}\left(Be_1(2s) + Be_2(2s)\right)$ and $3\sigma_u = 1/\sqrt{2}\left(Be_1(2s) - Be_2(2s)\right)$. The multi-reference configuration interaction (MRCI) calculations of Merritt et al.[4] indicated that the $^1\Sigma_g^+$ wavefunction was 54% $4\sigma_g^2$ and 41% $3\sigma_u^2$.

Gas phase spectra for BeOBe have been obtained using resonantly enhanced multiphoton ionization (REMPI), laser induced fluorescence (LIF) and stimulated emission pumping (SEP) techniques[4]. These data confirmed the linear centrosymmetric structure and the $^1\Sigma_g^+$ electronic symmetry for the ground state. Rotational constants and the fundamental frequencies of the ground state vibrational modes were also determined.

Given this background, it is apparent that ionization of BeOBe could result in a $4\sigma_g\ ^2\Sigma_g^+$ or $3\sigma_u\ ^2\Sigma_u^+$ state. MRCI calculations for the ion predict that the former is the ground state, with $^2\Sigma_u^+$ some 3146 cm^{-1} higher in energy. Merritt et al.[4] determined the ionization energy (IE) of BeOBe using photoionization threshold measurements (8.119(5) eV), but they did not obtain spectroscopic data for the ion.

In the present study we have used pulsed field ionization zero electron kinetic energy (PFI-ZEKE) spectroscopy to obtain spectroscopic data for $BeOBe^+$ and to refine the value for the IE. The results indicate the removal of an electron from a non-bonding orbital and confirm the $^2\Sigma_g^+$ symmetry for the ground state. In the following the vibrational modes of BeOBe and the ion are labeled 1, 2, and 3 for the symmetric stretch, bend and anti-symmetric stretch, respectively.

III.2 EXPERIMENTAL

The apparatus used in this study has been described in detail in previous section. BeOBe was prepared in the gas phase by ablating the surface of a beryllium rod with the fundamental output of a Nd/YAG laser (Continuum Minilite II, operating at ~20 mJ). The Be rod was continuously rotated and translated to expose a fresh surface for each laser shot. Helium supplied by a pulsed solenoid valve was used to cool and entrain the resulting plume, which was then expanded as a free-jet. Typically the source pressure and gas pulse duration were 2.1 bar and 240 μs. While $BeOBe^+$ could be observed using pure He as the carrier gas, it was typically seeded with 0.1% O_2 to increase both signal strength and stability of the source. The core of the free-jet expansion was transmitted into a second differentially pumped chamber though a conical skimmer with a 5 mm diameter orifice. The second chamber contains a time-of-flight mass spectrometer (TOFMS), and the components for both REMPI and PFI-ZEKE measurements.

The sequential excitation scheme shown in Fig. III.1 was used to record both REMPI and PFI-ZEKE spectra. Two pulsed Nd/YAG pumped dye lasers (Coherent Scanmate Pro and a Continuum ND6000 with laser line widths (FWHM) of ~0.15 cm^{-1}) were used for the sequential excitation. The two counter propagating laser beams were overlapped in the ionization region of the TOFMS, along an axis that was perpendicular to both the molecular beam and the spectrometer's flight tube. Digital delay generators were used to trigger the experiment at 10 Hz, to overlap the two laser beams in time and to have them coincide with the arrival of BeOBe in the molecular beam. REMPI spectra of BeOBe were recorded first so that the pump laser could be tuned to a specific ro-vibronic line. REMPI spectra have been collected previously by Merritt et al.[4]. The R(1) and R(2) rotational lines of the $(1)^1\Sigma_u^+ \leftarrow X^1\Sigma_g^+$ transition, $1_0^3 3_0^2$ band were chosen for the first step in the sequential ionization scheme. This band was selected because it is free of any overlapping transitions and displays a simple P and R branch structure with well resolved rotational lines, allowing a single rotational level to be easily identified and selected. PFI-ZEKE experiments were typically recorded by holding the extractor and repeller plates at -0.1 V during photoexcitation to establish field-free conditions. A delay time between 1.38 and 2.78 μs was used to allow prompt electrons to exit the ionization region. After the delay the voltage on the repeller plate was lowered to effect pulsed-field ionization of molecules in high-*n* Rydberg states, and to accelerate the resulting electrons towards the detector. A pulsed field of 1.43 V/cm was used to record all of the ZEKE spectra, except for those containing terminating on the 1_1 vibrational level of the ion. A stronger pulsed field of 2.14 V/cm was used to observe this level, due to the low signal intensities. Wavelength calibration was achieved using an I_2 reference cell, where the fundamental outputs from the dye lasers were used to observe the B-X bands.

III.3 RESULTS AND ANALYSIS

REMPI spectra were rotationally resolved and displayed a population distribution that was indicative of a rotational temperature of approximately 7K. Figure III.2 displays a broad scan of the PFI-ZEKE spectrum containing transitions the 0_0, the 2_1 and the 2_2 levels. Figure III.3 displays the 1_1 transition. The energy scale of Fig's III.2 and III.3 is that of the second photon. While signal intensities were not corrected for variations in laser power, transitions to bands other than the origin were much weaker, indicating that the electronic transition displayed in Fig. III.1 is near vertical. Figure III.4 displays scans over the origin band taken by pumping the R(1) and R(2) lines of the intermediate state.

The centers of the rotational lines were located by fitting a Gaussian function to each resolved feature. The rotational energy levels were well represented by the rigid rotor expression $E_{rot}=BN^+(N^++1)$, where N^+ is the angular momentum of the ion, exclusive of electron spin (Hund's case b). The spin-rotation splitting was below the resolution of these measurements. Note that only transitions to odd rotational states in the cation were observed using excitation via the R(1) line and even rotational states from the R(2) line. This pattern is due to the conservation of nuclear spin symmetry. Fitting of the rigid rotor energy level expression to the line centers was used to obtain the rotational constants that are listed in Table III. 1.

Vibrational energy level spacings were found by using the $N^+=1$ line centers and the rotational constants to locate the energies for the $N^+=0$ levels. The vibrational spacings are listed in Table III. 1. Vibrational constants for the bending mode were determined using the equation.

$$G(v^+) = \omega_e^+ v^+ - \omega_e x_e^+ v^+ \left(v^+ + 1\right)$$

Constants for the bending mode were $\omega_e^{+(2)}$=151.1(4) and $\omega_e x_e^{+(2)}$=3.5(1) cm^{-1}. $\Delta G_{1/2}^{+(1)}$ for the symmetric stretch was found to be 1037(4) cm^{-1}, where the relatively large error range is due to the weak signal intensity and the large pulsed field needed to observe this transition. Also, the

assignment of the rotational lines in this band was uncertain. Attempts were made to observe the anti-symmetric stretch, but this could not be detected.

The ionization energy of BeOBe, 56480(4) cm^{-1} was derived from multiple determinations of the blue edge of the 0_0, $N^+=1$ feature, recorded using the R(1) line of the intermediate state. The value given here is for the hypothetical $J=0\rightarrow N^+=0$ transition ($h\nu_1+h\nu_2-E(N^+=1)+E(J=0)$). This is in good agreement with the result of Merritt et al.[4], with an order of magnitude improvement in the uncertainty. The $BeOBe^+$ spectroscopy constants determined in this work are listed in Table III.2.

III.4 DISCUSSION

Theoretical calculations (MRCI)[4] yield a linear, symmetric structure for $BeOBe^+$, and the PFI-ZEKE spectra are consistent with this prediction. The exchange symmetry of the ground state can be rigorously determined from the rotational selection rules. Ionization starting from the J=1 level of the BeOBe $X\,^1\Sigma_g^+$ state accessed only the odd N^+ levels. Similarly, ionization from J=2 resulted in even N^+ states. Conservation of the odd/even property of the rotational levels shows that the ground state of the ion has the same electronic inversion symmetry as that of the neutral. Hence the ground state of BeOBe is $X\,^2\Sigma_g^+$.

The experimental evidence also supports the view that the HOMO of the ground electronic state of neutral BeOBe is non-bonding in character. The BeO bond length for the cation is equal to 1.392(8) Å, using the approximation $R_0 = \frac{h}{2}\sqrt{\frac{1}{m_{Be}B_0}}$. This is essentially unchanged from the value of R_0(BeO)=1.396(3) Å for the neutral X electronic state[4]. The $\Delta G_{1/2}$ value for the symmetric stretch is also nearly the same with 1037(4) cm^{-1} and 1039(1) cm^{-1} for the cation and neutral, respectively. The $\Delta G_{1/2}$ value for the bending mode does show a significant change with 144.2(5) cm^{-1} and 113(2) cm^{-1} for the cation and neutral, respectively. The higher bending

frequency for the ion is slightly surprising. Ostojic et al.[6] found that the $4\sigma_g 3\sigma_u\ ^3\Sigma_u^+$ state of neutral BeOBe has a higher bending frequency than that of $X\ ^1\Sigma_g^+$. They attributed this difference to the stabilization of the $4\sigma_g$ orbital on bending, which decreases the bending frequency of the neutral molecule in ground state. Based on this argument the $4\sigma_g$ configuration of the ground state ion would be expected to show a lower bending frequency than that of the neutral molecule.

Ab intio calculations by Boldyrev et al.[7] for MgOMg show that the molecule is very similar to BeOBe. It also has a linear $^1\Sigma_g^+$ ground state that has significant multi-reference character, and a low-lying $^3\Sigma_u^+$ state. The $MgOMg^+$ ion was predicted to be linear with a $^2\Sigma_g^+$ ground state[8]. Little experimental evidence exists for MgOMg. It has been trapped in a He droplet and subsequently detected by mass spectrometry[9]. MgOMg may also have been detected in the absorption spectrum of Mg atoms reacting with O_2 in a vacuum arc source, although no definite assignment could be made[10]. Andrews et al.[3,11] have used matrix isolation spectroscopy to examine the species produced when alkaline earth metals are laser vaporized in the presence of O_2. The products were characterized using IR absorption measurements. CaOCa was detected and a bent equilibrium structure was deduced from the results for isotopic substitution of both the Ca and O atoms[11]. Laser ablation of Mg did not yield bands that could be attributed to MgOMg. BaOBa has been created in a laser vaporization source and one-photon ionization efficiency measurements were used to determine the IE (3.87(5) eV)[12,13]. No experimental studies of SrOSr have been published, are far as the authors are aware. We have found that BeOBe is readily detected using photoionization techniques with mass selected detection. It is very probable that the other Group IIA hyperstochiometric oxides, which are species of significant theoretical interest, can be characterized by these methods.

REFERENCES

(1) Theard, L. P.; Hildenbrand, D. L. *J. Chem. Phys.* **1964**, *41*, 3416-20.

(2) Thompson, C. A.; Andrews, L. *J. Chem. Phys.* **1994**, *100*, 8689-99.

(3) Andrews, L.; Chertihin, G. V.; Thompson, C. A.; Dillon, J.; Byrne, S.; Bauschlicher, C. W., Jr. *J. Phys. Chem.* **1996**, *100*, 10088-10099.

(4) Merritt, J. M.; Bondybey, V. E.; Heaven, M. C. *J. Phys. Chem. A* **2009**, *113*, 13300-13309.

(5) Boldyrev, A. I.; Simons, J. *J. Phys. Chem.* **1995**, *99*, 15041-5.

(6) Ostojic, B.; Jensen, P.; Schwerdtfeger, P.; Assadollahzadeh, B.; Bunker, P. R. *J. Mol. Spectrosc.* **2010**, *263*, 21-26.

(7) Boldyrev, A. I.; Shamovskii, I. L.; Schleyer, P. v. R. *J. Am. Chem. Soc.* **1992**, *114*, 6469-75.

(8) Boldyrev, A. I.; Simons, J.; Schleyer, P. v. R. *Chem. Phys. Lett.* **1995**, *233*, 266-72.

(9) Krasnokutski, S. A.; Huisken, F. *J. Phys. Chem. A* **2010**, *114*, 7292-7300.

(10) Pesic, D.; Gaydon, A. G. *Proc. Phys. Soc., London* **1959**, *73*, 244-9.

(11) Andrews, L.; Ault, B. S. *J. Mol. Spectrosc.* **1977**, *68*, 114-21.

(12) Boutou, V.; Lebeault, M. A.; Allouche, A. R.; Paulig, F.; Viallon, J.; Bordas, C.; Chevaleyre, J. *J. Chem. Phys.* **2000**, *112*, 6228-6236.

(13) Boutou, V.; Lebeault-Dorget, M. A.; Allouche, A. R.; Bordas, C.; Chevaleyre, J. *Z. Phys. D At., Mol. Clusters* **1997**, *40*, 448-453.

Table III. 1: Vibrational energies and rotational constants for $BeOBe^{+}$.

v_2	E^a/cm^{-1}	$B_v{}^b/cm^{-1}$
0	0.0	0.483
1	144.2	0.491
2	281.4	0.503
v_1		
1	1037	0.478

a. Energy relative to the zero point level. Error is 0.5 cm^{-1} and 4 cm^{-1} for v_2 and v_1 respectively.

b. Error is 0.005 cm^{-1}.

Table III. 2: Spectroscopic constants for $BeOBe^{+}$.

	IE	R_0(BeO)	$\omega_e^{(2)}$	$\omega_e x_e^{(2)}$
Value[a]	65480(4)	1.392(8)	151.1(4)	3.5(1)

All units are in cm^{-1} except for R_0 which is in Å.

Figure III.1. Two-color excitation scheme used to record the PFI-ZEKE spectrum of BeOBe.

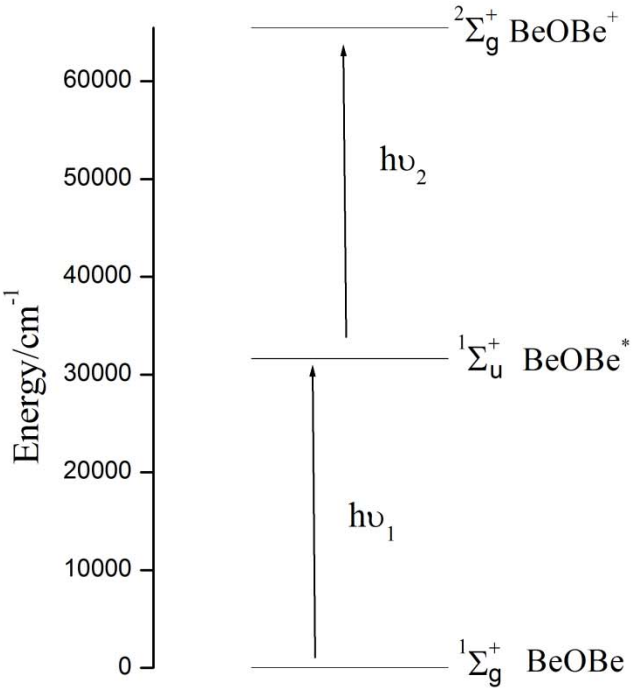

Figure III.2. Survey scan of the origin band and the first two bending modes of $BeOBe^+$. The energy scale is that of the second photon.

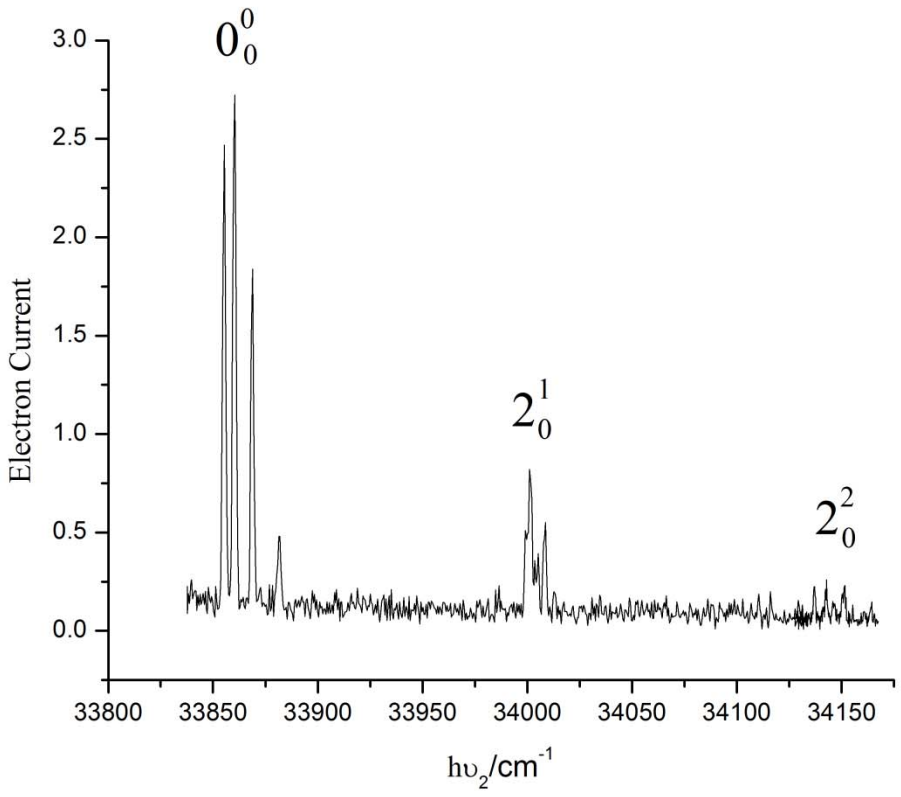

Figure III.3. PFI-ZEKE spectrum of the 1_1 band. Assignment of the rotational lines is not certain due to the weak signal strength. The numbers given next to each line are the N^+ values. The energy scale is that of the second photon.

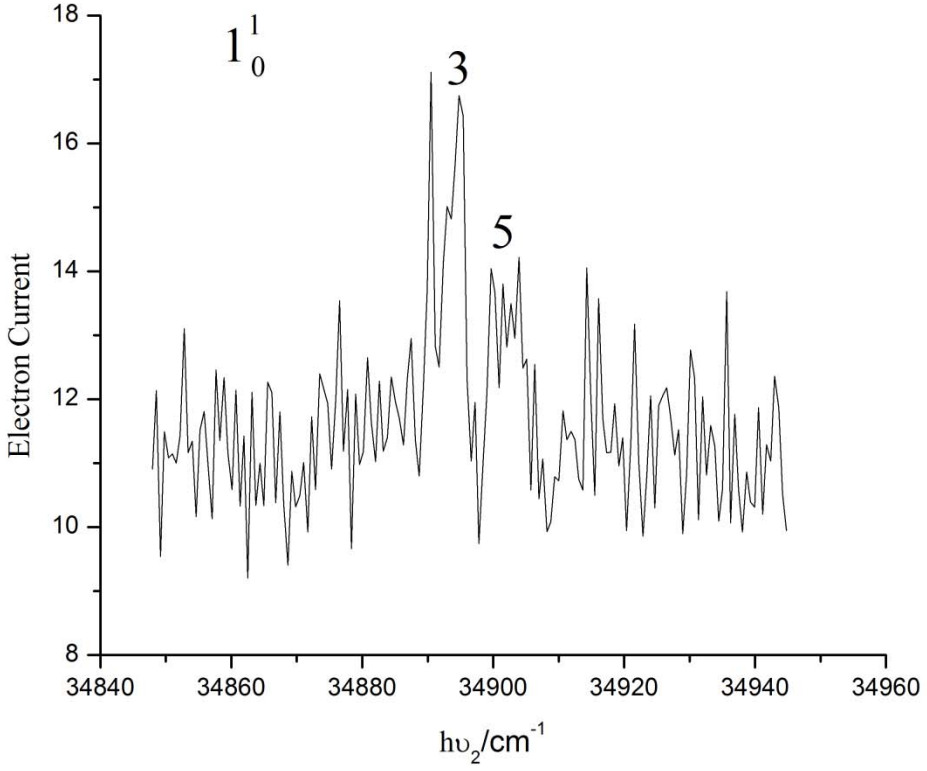

Figure III.4. PFI-ZEKE spectrum of the origin band taken with $h\nu_1$ tuned to the $1_0^3 3_0^2$ band of the $(1)^1\Sigma_u^+ \leftarrow X^1\Sigma_g^+$ transition. Trace A was recorded using the R(1) line and trace B using the R(2) line. Note the appearance of only odd or even rotational lines of the ion, respectively. The numbers given next to each line are the N^+ values. The energy scale has been shifted so it is relative to the J″=0 level of the neutral molecule ground state.

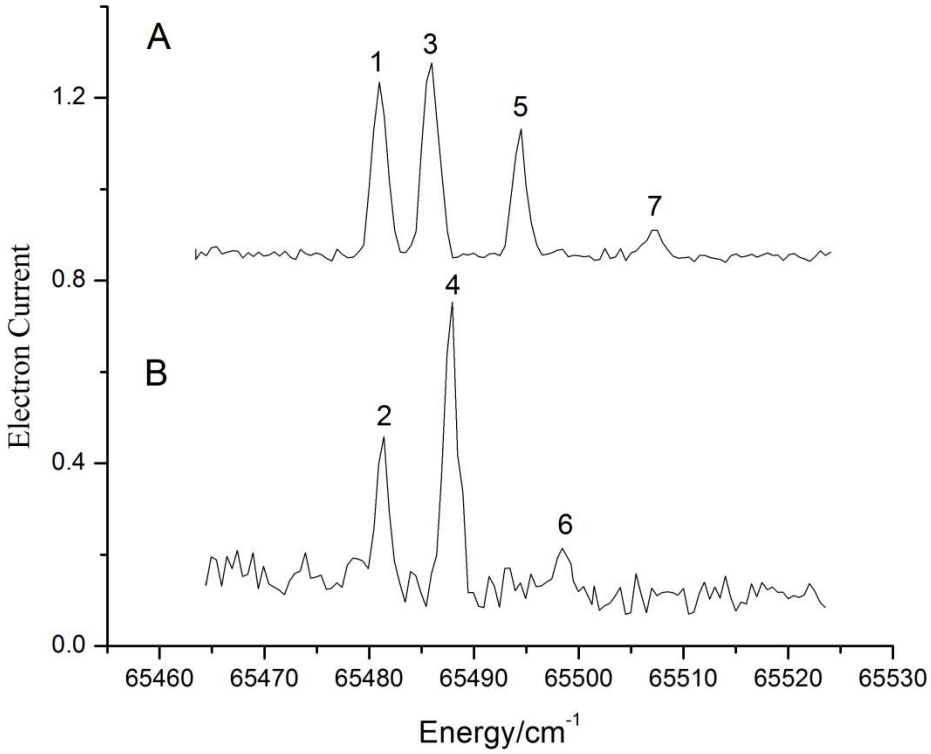

CHAPTER IV

EXPERIMENTAL AND THEORETICAL STUDIES OF THE ELECTRONIC TRANSITIONS OF BEC

IV.1 INTRODUCTION

Diatomic beryllium carbide has been the subject of several theoretical investigations[1-13]. Interest in this molecule has arisen because it poses challenges for computational *ab initio* electronic structure models, and studies of the isolated Be-C bond can yield insights concerning beryllium carbides.

Initially, it was not known if BeC would have a $^3\Sigma^-$ or $^5\Sigma^-$ ground state[6,9]. The valence orbitals can be approximately described as 1σ (C2*s*), 2σ (Be2*sp* - C2*sp*), $1\pi_x$, $1\pi_y$ (C $2p_x$,$2p_y$ + Be $2p_x$,$2p_y$) and 3σ(Be2*sp* + C2*sp*). The possibilities for the ground state are then $^3\Sigma^-$ (leading configurations $1\sigma^2 2\sigma^2 1\pi_x 1\pi_y$ and $1\sigma^2 3\sigma^2 1\pi_x 1\pi_y$) or $^5\Sigma^-$ ($1\sigma^2 2\sigma 3\sigma 1\pi_x 1\pi_y$). The triplet state is multi-configurational while the quintet is well described by a single determinant[1,2,6,9]. Consequently, single reference treatments such as HF and GVB found the quintet to be lower in energy, while the ordering reversed when higher level correlation treatments were applied. The highest level calculations have consistently predicted a $^3\Sigma^-$ ground state, with the $^5\Sigma^-$ state at energy of approximately 1500-2000 cm^{-1}. Note that $^3\Sigma^-$ correlates with ground state atomic products (Be(^{1}S)+C(^{3}P)) while the quintet state correlates with the products Be(^{3}P)+C(^{3}P), 21979 cm^{-1} above the ground state dissociation asymptote. The prediction that the minima of the $^3\Sigma^-$ and $^5\Sigma^-$ states are so close in energy reflects a substantially stronger bond for the latter. This point has been discussed by Wright and Kolbuszewski[2], who noted that the approximate bond orders of the $1\sigma^2 2\sigma^2 1\pi^2$ and $1\sigma^2 2\sigma 3\sigma 1\pi^2$ configurations were 1.0 and 1.5, respectively.

Recent generations of density functional theory (DFT) calculations also find that $^3\Sigma^-$ is the ground state, and predict molecular constants that are in good agreement with the results from multi-configurational *ab initio* calculations[7,10-12]. These comparisons were used to benchmark methods that were then applied to investigate the properties of larger beryllium carbide clusters.

Several electronically excited states of BeC have been examined using multi-reference single and double excitation calculations that were followed by a configuration interaction treatment (MRSD-CI). Wright and Kolbuszewski[2] predicted the potential energy curves of 25 states, including those of singlet, triplet and quintet multiplicity. They noted that BeC, like the isoelectronic B_2 molecule, exhibits a number of deeply bound, doubly excited states. For excitation energies that are relevant to the present study (30000-40000 cm^{-1}) they predicted a family of strongly interacting $^3\Pi$ states. Borin and Ornellas[1] used MRSD-CI to examine the properties of 13 states of BeC. Their results were published at almost the same time as the paper by Wright and Kolbuszewski[2], and there was good agreement between the two sets of calculations. Again, strong interactions between the $^3\Pi$ states were readily apparent.

Theoretical prediction of the photoelectron spectrum of BeC was carried out by Borin and Ornellas[3]. These calculations also used the MRSD-CI method. The ground state for the ion was found to be $1\sigma^2 2\sigma 1\pi_x 1\pi_y$, $X^4\Sigma^-$. The ionization energy, with inclusion of the zero-point energies, was estimated to be 8.316 eV.

In the present study we have recorded rotationally resolved electronic spectra for BeC and determined of the ionization energy (IE). Transitions to the interacting $^3\Pi$ states dominated the spectral region examined (for example, see Fig. IV.3 of ref. 2[2]), resulting in vibronic structure that exhibited few regular intervals. Assignment of these data required predictions of the vibronic term energies and Franck-Condon factors. The *ab initio* calculations were performed by our collaborator Richard Dawes (see also Appendix) and proved to be critical for understanding the electronic and vibrational structure of BeC responsible for the observed spectra. Hence, in the

following I begin by describing the theoretical calculations of Richard Dawes. I then describe the experimental procedures, observations, analyses and comparisons with theory.

IV.2 THEORETICAL CALCULATIONS

Potential energy curves for states of Σ, Π and Δ symmetry were calculated using a dynamically weighted MRCI technique[14], with each state individually optimized. The energy dependent weight factor was set to B = 3.0 eV. Dunning's augmented, correlation consistent basis sets were used for Be and C. Results obtained using triple, quadruple and quintuple zeta basis sets were extrapolated to the complete basis set (CBS) limit, correlating all electrons. The Davidson correction (+Q) was not applied since tests including the asymptotic gaps between atomic states (discussed below) confirmed better uncorrected performance (which has been noted previously in other few-electron systems[15]). An estimate of the small relativistic correction was added using the eighth-order Douglas-Kroll-Hess Hamiltonian (DKH8), and CBS extrapolation using the same basis sets. The small effects of spin-orbit coupling were neglected. All calculations were carried out using the MOLPRO 2010.1 suite of programs[16].

Adiabatic potential energy curves for $X^3\Sigma^-$ and the $n^3\Pi$ states with n=1-4 are shown in Fig. IV.1 (a). These particular states are displayed because they account for the majority of the bands observed above 31000 cm^{-1}. The molecular ground ($X^3\Sigma^-$) and $1^3\Pi$ states correlate asymptotically with ground state atoms C(^3P_g) and Be(^1S_g), while the $2^3\Pi$ and $3^3\Pi$ states correlate to the Be(^3P_u) excited atomic state. The $4^3\Pi$ state correlates to excited states of both atoms, C(^1D_g) and Be(^3P_u). Asymptotic gaps between the atomic states were calculated (by the procedure described above) at a distance of 10.0 Å. The Be(^3P_u) state was calculated at 22033 cm^{-1} (no Davidson) and 21846 cm^{-1} (with Davidson) above the ground state, compared with an experimental value[17] of 21978.3 cm^{-1}. The asymptotic gap to $4^3\Pi$ was calculated at 32175 cm^{-1} (no Davidson) and 31748 cm^{-1} (with Davidson) compared with 32170.9 cm^{-1} from experiment[17].

The calculated gaps between atomic states are significantly more accurate without application of the Davidson correction. Molecular constants for the ground state, derived from the potential, were ω_e=937.9, $\omega_e x_e$=9.6, B_e=1.190, B_0=1.178 cm^{-1}, and R_e=1.661 Å. In order to compute the vibronic energies of the $^3\Pi$ states, the diabatic potential energy curves and coupling matrix elements were reconstructed from the n=1-4 adiabats. At each internuclear distance, the inverse eigenvalue problem was solved for a four-coupled-state model including couplings only between neighboring states. Diabatic coupling strengths were set to one-half of the minimum gaps between adiabatic curves[18,19]. Based on calculated derivative couplings (MOLPRO), Gaussian coupling profiles were used. The parameters used in the diabatization procedure are presented in the Appendix section and the resulting diabatic curves are plotted in Fig. IV.1 (b). Vibronic energies were then computed by the discrete variable representation (DVR) method[20], taking into account the interactions between the four states. To solve the 1D Hamiltonian, 1000 *sinc*-DVR points were placed in a regular grid between 1.0 and 6.0 Å (the coupled 4-state matrix is thus of dimension 4000). It can be appreciated from Figure IV.1 that with a four-state model, even vibronic states with dominant $3^3\Pi$ and $4^3\Pi$ character couple to the continuum through the chain of couplings. Therefore an optimized complex absorbing potential (CAP) was used and the vibronic state solutions were obtained by diagonalizing the resulting complex-symmetric Hamiltonian. Following Skokov *et al*.[21] and Mussa *et al*.[22], the height and range of the CAP was optimized for each state individually. The real part of each eigenvalue provided the vibronic energy, while the complex part defined the width of the level. Table IV.1 lists the vibronic energies for these coupled states, relative to the energy of the ground state zero-point level. The states are simply numbered in ascending energy order to facilitate further discussion. Column three gives rotational constants derived from $<1/R^2>$ expectation values, while column four lists the Franck-Condon factors for transitions originating from $X^3\Sigma^-$, v=0. The last four columns of Table IV.1 give the fractional characters of the eigenstates, in terms of percentage contributions

from each of the four diabatic $^3\Pi$ states. The calculated widths are very small for the states discussed here and are tabulated in Appendix section.

Fig. IV.2 shows potential energy curves for the ground state and the first two states of quintet multiplicity ($1^5\Sigma^-$ and $1^5\Pi$), which are also relevant to the observed transitions. Table IV. 2 lists the energies and Franck-Condon factors for $1^5\Pi$, v' $\leftarrow 1^5\Sigma^-$, v''=0 transitions, along with rotational constants for the $1^5\Pi$state. The calculations predict that the zero-point level of $1^5\Sigma^-$ is 2059.7 cm^{-1} above $X^3\Sigma^-$, v=0, with a rotational constant of B_0=1.250 cm^{-1}. The low-energy vibrational levels of $1^5\Sigma^-$ were well represented by the constants ω_e=1036.0, $\omega_e x_e$=7.84 cm^{-1}.

To explore all of the most plausible assignment options for the spectra, calculations of the vibronic levels of the $2^3\Sigma^-$, $3^3\Sigma^-$, $1^3\Sigma^+$, $2^3\Sigma^+$, $1^3\Delta$ and $2^3\Delta$ states were carried out. These results have been provided in the Appendix section.

IV.3 EXPERIMENTAL

The apparatus used for these experiments has been described in Section II. Gas phase samples of BeC were generated by pulsed laser ablation. The output of a pulsed Nd/YAG laser (Continuum Minilite II, operating at ~20 mJ per pulse at 1064 nm) was focused onto the surface of a beryllium rod, which was continuously rotated and translated to expose a fresh surface to each laser shot. The hot plasma produced by the laser vaporization was entrained in a pulse of high pressure helium carrier gas, which was then expanded as a free jet. The pulse was produced by a solenoid valve that was operated at source pressures near 30 psi, with pulse duration of 300 μs.

Resonantly enhanced multiphoton ionization (REMPI) and photoionization efficiency spectra were recorded to investigate the electronic structure and bonding of BeC. A two-color excitation scheme was used to record REMPI spectra. The transitions investigated in this study occurred in the 30500-40000 cm^{-1} range. Transitions occurring above 35400 cm^{-1} were initially

observed using one-color, two photon excitation. Lower energy transitions were recorded using a two-color excitation scheme, with the second photon provided by a KrF laser (248 nm). The two counter-propagating laser beams were overlapped in time and space in the ionization region of the TOF mass spectrometer, along an axis perpendicular to both the molecular beam and the flight tube of the mass spectrometer.

Photoionization efficiency (PIE) curves were recorded using two tunable dye lasers in order to accurately locate the ionization energy. The first dye laser was set to excite a particular resonant transition of BeC while the second dye laser was scanned to locate the onset of ionization.

Frequency doubling of the outputs from both dye lasers was used to generate tunable light in the near UV spectral range. Several different laser dyes were used to record the spectra, and the intensities have not been corrected for variations in the laser powers. For low-resolution scans the wavelength calibration of the lasers was established with reference to the known transitions of atomic Fe and Ti impurities that were present in this wavelength region. Higher resolution spectra were obtained using an intracavity etalon. For these scans the I_2 B-X LIF spectrum was recorded simultaneously to achieve an absolute calibration[23] of the dye laser fundamental wavelength on the order of 0.1 cm^{-1}.

Attempts to record laser induced fluorescence spectra for BeC were unsuccessful as intense bands of Be_2O dominated the wavelength range examined[24]. Ultra high-purity He was used in these experiments, so it is likely that the oxide originated from the beryllium rod.

IV.4 RESULTS AND ANALYSIS

Electronic spectra for BeC were discovered in REMPI survey spectra that were used to characterize the output from a Be laser vaporization source. The initial observations were made without the addition of carbon-containing reagents. BeC production was then improved by

adding a trace of C_2H_2 (0.2%) to the He carrier flow. Low-resolution REMPI spectra for BeC are presented in Fig. IV.3. This trace shows a series of vibronic bands with rather erratic spacings. Rotationally resolved spectra were recorded for ten of these features, and the structures observed were key to assigning the lower-energy bands. Figures IV.4 and IV.5 show rotational bands that are representative of two characteristic structures, that were blue- and red-shaded, respectively. The spectral simulation program PGOPHER[25] was used to simulate and analyze the rotational structures. Based on the results from the *ab initio* calculations, $^3\Pi$-$X^3\Sigma^-$ transitions were expected. The downward-going trace in Fig. IV.4 shows a simulation based on this transition type. For this simulation it was assumed that the spin-rotation splitting in the ground state would be below the resolution of the measurements.

Seven of the bands that were rotationally resolved had blue-shaded structures that were consistent with assignment to $^3\Pi$-$X^3\Sigma^-$ transitions. Molecular constants were derived from these bands by use of the fitting routine of PGOPHER[25]. In the first cycle of this analysis, the parameters varied in each fit were the band origin (ν_0), upper and lower state rotational constants (B' and B") and the upper state spin-orbit coupling constant (A_{SO}'). Exploratory fits showed that the centrifugal distortion constants, spin-rotation and lambda-doubling constants could not be determined with statistical significance. Consequently, these parameters were set to zero. It was evident that the majority of the $^3\Pi$-$X^3\Sigma^-$ bands originated from the v"=0 level which was confirmed by recording PIE curves Hence, in the second cycle of the analysis these bands were fitted with the ground state rotational constant fixed at the average value obtained from the band-by-band analyses. The results from these fits are collected in Table IV.3. The average ground state constant, B_0"=1.1624 cm^{-1}, was reasonably close to the theoretically predicted value of B_0"=1.178 cm^{-1}.

A hot band of the $^3\Pi$-$X^3\Sigma^-$ system was observed on the high-frequency side of the 31797.0 cm^{-1} band. To improve the signal-to-noise ratio for this feature, the jet expansion conditions were adjusted to produce a warmer spectrum. This was done by reducing the carrier

gas source pressure and adjusting the delay between the gas pulse and the ablation laser pulse. Molecular constants for the hot band, which was centered at ν_0= 31862.1 cm^{-1}, are included in Table IV.3.

Figure 5 shows an example of the type of red-shaded rotational structure exhibited by some of the lower energy bands. Combination difference analyses showed that these bands originated from a lower level with a rotational constant of B"= 1.229 cm^{-1}, indicating that the lower electronic state was not $X^3\Sigma^-$. This was subsequently confirmed by two-photon ionization threshold measurements (see below). From comparison with the theoretical predictions (cf. Table IV. 2), it was evident that the band rotational structures and transition energies were consistent with assignment to the $1^5\Pi$-$1^5\Sigma^-$ transition. The downward-going trace in Fig. IV.5 is a simulation that assumes this transition type, with unresolved spin-rotation splitting of the lower state, and upper state constants of B'=1.040 and A_{SO}'=-0.4 cm^{-1}. Molecular constants for the $1^5\Pi$-$1^5\Sigma^-$ bands were obtained from fits where the parameters ν_0, B", B', and A_{SO}' were treated as variables. All other constants were held at zero. The results are listed in Table IV.4 and a representative fitting of the 1-0 band has been included in the Appendix section.

The low resolution scans (Fig. IV.3) contained many other features that were not investigated at the level of rotational resolution. For the more intense members of this group, the band contour maxima are collected in Table IV.5.

Ionization thresholds for BeC were determined using two-color sequential excitation. Ionization via a $^3\Pi$-$X^3\Sigma^-$ transition was examined using the first photon to excite the band centered at 31797 cm^{-1}. A scan over the wavelength of the second photon revealed a relatively sharp threshold at a total energy of 70683±40 cm^{-1}. Correction for the effect of the 250 V cm^{-1} field in the ionization region of the mass spectrometer yielded a field-free IE of 70779±40 cm^{-1}. Ionization via the $1^5\Pi$-$1^5\Sigma^-$ transition was examined using initial excitation of the band at 30791.7 cm^{-1}. This measurement yielded a field-free threshold of 68477±40 cm^{-1}. Assuming that both ionization measurements produced ground state BeC^+ $X^4\Sigma^-$ (see discussion) the difference in

energy between the thresholds indicates that the v=0 level of $1^5\Sigma^-$ lies 2302±80 cm^{-1} above the ground state zero-point level.

IV.5 DISCUSSION

The level of agreement between the observed and predicted band origins for the v'≤3 transitions of the $3^3\Pi$-$X^3\Sigma^-$ system was sufficient to establish unambiguous assignments. Table IV.6 presents a comparison of these data. The ground state constants derived from the spectra, B_0"=1.1624(30) and $\Delta G_{1/2}$"=901.7(3) cm^{-1} are reasonably close to the calculated values of 1.178 and 918.7 cm^{-1}. Note that the calculations overestimated the vibrational frequency and the rotational constant. The calculated data for the v'≤3 levels of the $3\Pi^3$ states also yielded vibrational intervals and rotational constants that were slightly larger than the observed values (e.g., $\Delta G_{1/2}$"=980.8 (calc) vs. 966.7 (obs) cm^{-1}).

Assignment of the triplet bands becomes more difficult for the levels with v'≥4. From the data in Table IV.1 it can be seen that v'=3 (state 51) is almost the last level predicted to have predominantly $3^3\Pi$ character (above this, only state 76 has >50% $3^3\Pi$. State 55 is approximately the v'=4 state, but has only 47% $3^3\Pi$ character. The band observed at 35732.0 cm^{-1} is the best candidate for the 4-0 band, but it is 233.9 cm^{-1} above the predicted energy. As none of the other transitions predicted in this energy region have significant Franck-Condon factors we tentatively assign this as the 4-0 band in Table IV.3. If this is correct, it implies that vibronic interactions have distorted the vibrational manifold such that v'=4 is pushed up by approximately 230 cm^{-1} relative to the energy obtained by extrapolating the energy intervals of the v'≤3 levels. In a model that considers the interactions between two electronic states, this behavior mimics the crossing of vibrational term series where the perturbing state pushes down on the levels with v'≤3, and is crossed from below by the observed series. The large upward displacement of v'=4 would then signify that the crossing occurred just below this level. Due to intensity borrowing, the level that

perturbed v'=4 should also be observable in the spectrum. The unassigned band at 35274 cm^{-1} (Table IV.5) is a possible candidate. However, as there are four interacting term series, this speculation is not intended to do more than illustrate the difficulties of establishing assignments. Viewed in terms of the challenges posed for the theoretical calculations, it is evident that small changes in the energies of the vibrational levels obtained from the diabatic potential energy curves will, when two or more levels are close in energy, have dramatic effects on the adiabatic energies.

Correlations between the BeC bands at higher energies (cf. Table IV.5) and the Franck-Condon active transitions of Table IV.1 can be made, but the energy discrepancies are in the range of 100-200 cm^{-1}. Given the difficulties outlined above, we refrain from proposing assignments at this time. It is evident, however, that the erratic band intervals seen at energies above 35000 cm^{-1} are consistent with strong interactions between the four lowest energy $^3\Pi$ states.

The magnitudes of the spin-orbit coupling constants for the $3^3\Pi$ $v' \leq 3$ levels are indicative of an electronic state that contains a significant fraction of C($2p\pi$) character. The calculations of Wright and Kolbuszewski[2] predicted that the $3^3\Pi$ state is 71% $1\sigma^2 3\sigma 1\pi^3$ at R=1.48 Å and 58% $1\sigma^2 2\sigma 3\sigma^2 1\pi$ at R=1.90 Å. These characteristics are consistent with the negative sign of the spin-orbit coupling constants. To add some quantitative support for this interpretation, MOLPRO was used to calculate the spin-orbit coupling constant for the $3^3\Pi$ state at an internuclear distance of 1.5 Å (calculations carried out at the all-electron MRCI level with aug-cc-pwCVQZ basis sets). The value obtained, A_{SO}=-9.4 cm^{-1}, was remarkably close to the measure value for the v=0 level of -9.8 cm^{-1}. Given the extensive interactions that occur between the $n^3\Pi$ states, it would not have been surprising to observe an erratic dependence of the measured spin-orbit coupling constants on the vibrational quantum number. However, the first four states show coupling constants that diminish slightly with increasing v. The anomalous value of the spin-orbit coupling

constant for the state that has been tentatively assigned to v=4 is consistent with the notion that this upper state is strongly perturbed.

Several calculations for the term energy of $1^5\Sigma^-$, including the computational results presented here, are in good agreement with the experimental value[1,2,9,11,12]. Our calculations yield a shorter equilibrium distance for $1^5\Sigma^-$ as compared to the ground state, and the observed zero-point rotational constants (Tables IV.3 and IV.4) confirm this prediction. The calculated zero-point constant for $1^5\Sigma^-$ of B_0=1.250 cm^{-1} is slightly larger than the observed value of 1.229(4) cm^{-1}. We expect that the calculated harmonic vibrational constant of ω_e=1036 cm^{-1} is also overestimated. Scaling, based on the results for $X^3\Sigma^-$, yields a value of ω_e=1022 cm^{-1}.

The spectral region that should contain the origin band of the $1^5\Pi$-$1^5\Sigma^-$ transition was not examined. However, the level of agreement between the observed and calculated band origins for the v'=1-3 levels (presented in Table IV. 6), and the lower state term energy obtained from the IE measurements, establish reliable assignments. The $1^5\Pi$ state vibrational constants of ω_e=777.6 and $\omega_e x_e$=15.4 cm^{-1} are indicative of a potential energy curve that is slightly softer than the calculated potential, which yields ω_e=808.0 and $\omega_e x_e$=15.3 cm^{-1} from a fit to the v'=0-4 levels. In accordance with this difference, the measured rotational constants are systematically lower than the calculated values of Table IV.2.

The spin-orbit coupling constants for the lower levels of $1^5\Pi$ were rather poorly defined by the present data set. Negative constants produced simulations that were marginally better than those obtained with positive constants, but the sign choice given in Table IV. 4 is tentative.

The theoretical predictions made in this work for the $X^3\Sigma^-$, $1^5\Sigma^-$ and $1^5\Pi$ states of BeC are compared with the results from earlier MRSD-CI calculations in Table IV.7. Overall, the agreement between the calculations and the correspondence with the experimental results, are reasonably good. Wright and Kolbuszewski[2] provided the only other predictions for the $3^3\Pi$ state, and their results are not readily compared with current work. The problem is that the potential energy curves have significantly different characteristics. Wright and Kolbuszewski[2] obtained a

double minimum potential, with the outer minimum (near 2.15 Å) deeper than the inner minimum (near 1.59 Å). In contrast, the calculations in this work find that the inner minimum near 1.55 Å is deepest, with a secondary minimum near 2.15 Å. As transitions from the ground state zero-point level will probe the inner minimum, it is most informative to compare the calculated and experimental results for this region of the potential. The calculations in current work yield a T_0 value for $3^3\Pi$ of 31813.5 cm^{-1}, just 16.4 cm^{-1} above the observed value. The calculated T_e value for this state was 31329 cm^{-1}. The inner minimum of the potential reported by Wright and Kolbuszewski[2] was at 32262 cm^{-1}. While the agreement between the predicted energies for this state near R=1.57 Å is respectable, the very different shapes of the potential curves do not permit a meaningful comparison of the vibrational and rotational constants.

Borin and Ornellas[3] used MRSD-CI calculations with a relatively large basis set to explore the photoelectron spectrum of BeC. Their calculations, which included zero-point energies, gave an IE of 67073 cm^{-1}. This is in reasonable agreement with the measured value of 70779±40 cm^{-1}. As the $X^4\Sigma^-$ ground state of BeC^+ was predicted to have an equilibrium internuclear distance that was similar to that of BeC $X^3\Sigma^-$, Franck-Condon intensity simulations suggest that the photoelectron spectrum near the first ionization threshold will show a short vibration progression, dominated by the v^+=0-v=0 band. Ionizing transitions to low-lying states of $^2\Pi$, $^2\Delta$ and $^2\Sigma^-$ symmetry were also predicted. It is probable that all of these states could now be investigated at the level of rotational resolution using the technique of two-color pulse field ionization - zero kinetic energy photoelectron spectroscopy[26,27].

As DFT methods have been used to explore larger Be_nC_m clusters, it is of interest to see how successful these methods are for the simple diatomic molecule. The multi-configurational nature of the ground state raises some cause for concern as the DFT models are single reference. Despite this limitation, DFT models have provided results that are remarkably close to the measured properties. For example, Midda and Das[7] used the B3LYP hybrid model, with Dunning's correlation consistent polarized valence X-zeta basis sets (with X=2-5). The results

were extrapolated to the complete basis set limit. For the $X^3\Sigma^-$ state they obtained $\Delta G_{1/2}$=905.6, B_e=1.185 and IE=71122 cm^{-1}. More recently, two studies applied the B3P-W91 model. Patrick et al.[11] used a basis set of triple-zeta quality. They obtained $\Delta G_{1/2}$=905.2, B_e=1.179 and IE=70090 cm^{-1}. These calculations were also applied to the $1^5\Sigma^-$ state, yielding a term energy of 1540 cm^{-1} and rotational constant of B_e=1.232 cm^{-1}. Ghouri et al.[12] used the Pople-style 6-31+G* basis sets. They reported an equilibrium internuclear distance of R_e=1.673 Å (equivalent to B_e=1.170 cm^{-1}) and a term energy for $1^5\Sigma^-$ of 1613 cm^{-1}. It has already been noted that the agreement between the results from MRSD-CI and DFT calculations provides support for using the latter for studies of larger clusters. Comparisons with the experimental data now validate the results from both computational approaches.

REFERENCES

(1) Borin, A. C.; Ornellas, F. R. *J. Chem. Phys.* **1993**, *98*, 8761-9.

(2) Wright, J. S.; Kolbuszewski, M. *J. Chem. Phys.* **1993**, *98*, 9725-33.

(3) Borin, A. C.; Ornellas, F. R. *Chem. Phys.* **1994**, *184*, 59-66.

(4) Borin, A. C.; Ornellas, F. R. *Chem. Phys.* **1995**, *190*, 43-52.

(5) da Silva, C. O.; da Silva, E. C.; Nascimento, M. A. C. *Astrophys. J.* **1995**, *439*, 1044-5.

(6) Da Silva, C. O.; Teixeira, F. E. C.; Azevedo, J. A. T.; Da Silva, E. C.; Nascimento, M. A. C. *Int. J. Quantum Chem.* **1996**, *60*, 433-438.

(7) Midda, S.; Das, A. K. *J. Mol. Spectrosc.* **2004**, *224*, 1-6.

(8) Pelegrini, M.; Roberto-Neto, O.; Ornellas, F. R.; Machado, F. B. C. *Chem. Phys. Lett.* **2004**, *383*, 143-148.

(9) Teberekidis, V. I.; Kerkines, I. S. K.; Tsipis, C. A.; Carsky, P.; Mavridis, A. *Int. J. Quantum Chem.* **2005**, *102*, 762-774.

(10) Chen, M. D.; Li, X. B.; Yang, J.; Zhang, Q. E.; Au, C. T. *Int. J. Mass Spectrom.* **2006**, *253*, 30-37.

(11) Patrick, A. D.; Williams, P.; Blaisten-Barojas, E. *J. Mol. Struct. THEOCHEM* **2007**, *824*, 39-47.

(12) Ghouri, M. M.; Yareeda, L.; Mainardi, D. S. *J. Phys. Chem. A* **2007**, *111*, 13133-13147.

(13) Wells, N.; Lane, I. C. *Phys. Chem. Chem. Phys.* **2011**, *13*, 19036-19051.

(14) Barker, B. J.; Antonov, I. O.; Merritt, J. M.; Bondybey, V. E.; Heaven, M. C.; Dawes, R. 2012.

(15) Barker, B. J.; Antonov, I. O.; Merritt, J. M.; Bondybey, V. E.; Heaven, M. C.; Dawes, R. *J Chem Phys*, *137*, 214313.

(16) Dawes, R.; Jasper, A. W.; Tao, C.; Richmond, C.; Mukarakate, C.; Kable, S. H.; Reid, S. A. *J. Phys. Chem. Lett.* **2010**, *1*, 641-646.

(17) Dawes, R.; Wagner, A. F.; Thompson, D. L. *J. Phys. Chem. A* **2009**, *113*, 4709-4721.

(18) Werner, H.-J.

(19) NIST 2012.

(20) Vazquez, G. J.; Amero, J. M.; Liebermann, H. P.; Lefebvre-Brion, H. *J. Phys. Chem. A* **2009**, *113*, 13395-13401.

(21) Lefebvre-Brion, H.; Field, R.; Editors *The Spectra and Dynamics of Diatomic Molecules, Revised and Enlarged Edition; Second Edition*, 2004.

(22) Light, J. C.; Carrington, T., Jr. *Advances in Chemical Physics* **2001**, *114*, 263-310.

(23) Skokov, S.; Bowman, J. M.; Mandelshtam, V. A. *Phys. Chem. Chem. Phys.* **1999**, *1*, 1279-1282.

(24) Mussa, H. Y.; Tennyson, J. *Chemical Physics Letters* **2002**, *366*, 449-457.

(25) Salami, H.; Ross, A. J. *J. Mol. Spectrosc.* **2005**, *233*, 157-159.

(26) Merritt, J. M.; Bondybey, V. E.; Heaven, M. C. *J. Phys. Chem. A* **2009**, *113*, 13300-13309.

(27) Western, C. M.; University of Bristol: 2007.

(28) Antonov, I. O.; Barker, B. J.; Heaven, M. C. *J Chem Phys* **2011**, *134*, 044306.

(29) Heaven, M. C.; Bondybey, V. E.; Merritt, J. M.; Kaledin, A. L. *Chem. Phys. Lett.* **2011**, *506*, 1-14.

Table IV.1. Calculated vibronic energies, rotational constants, Franck-Condon factors and leading eigenstate fractions for the first four $^3\Pi$ states of BeC

level	E/cm^{-1}	B/cm^{-1}	FCF	% $1^3\Pi$	% $2^3\Pi$	% $3^3\Pi$	% $4^3\Pi$
1	8992.3	1.052	0.555	99.6	0.4	0.0	0.0
2	9750.0	1.035	0.302	99.3	0.6	0.0	0.0
3	10480.4	1.021	0.106	98.3	1.7	0.0	0.0
4	11153.9	1.071	0.043	84.0	16.0	0.0	0.1
5	11449.7	1.334	0.067	24.9	74.9	0.0	0.2
6	11923.0	1.014	0.009	91.5	8.5	0.0	0.0
7	12552.0	1.037	0.022	81.8	18.1	0.0	0.1
8	12768.3	1.332	0.258	21.2	78.5	0.0	0.3
9	13226.6	0.951	0.025	96.6	3.4	0.0	0.0
10	13779.5	1.097	0.115	63.1	36.8	0.0	0.2
11	13978.2	1.199	0.158	42.3	57.5	0.0	0.2
12	14464.6	0.901	0.012	96.6	3.3	0.0	0.0
13	14990.7	0.980	0.064	78.5	21.3	0.0	0.1

14	15111.1	1.257	0.142	24.6	75.1	0.0	0.4
15	15550.2	0.840	0.001	97.1	2.9	0.0	0.0
16	16032.1	0.798	*a*	98.7	1.2	0.0	0.0
17	16262.7	1.372	0.091	2.8	96.6	0.0	0.6
18	16467.8	0.755	*a*	98.7	1.3	0.0	0.0
19	16847.4	0.702	*a*	98.7	1.3	0.0	0.0
20	17157.2	0.634	*a*	98.0	2.0	0.0	0.0
21	17371.2	0.618	0.003	86.1	13.8	0.0	0.1
22	17422.6	1.083	0.019	29.0	70.5	0.0	0.5
23	17433.8	0.309	0.002	92.5	7.4	0.0	0.1
24	17457.8	0.249	0.001	98.1	1.9	0.0	0.0
25	18538.5	0.667	0.002	63.6	36.1	0.0	0.3
26	19622.8	0.666	*a*	64.2	35.4	0.0	0.4
27	20680.4	0.705	*a*	59.6	39.9	0.0	0.5
28	21716.4	0.845	*a*	45.9	53.2	0.0	0.9
29	22730.3	1.008	*a*	28.8	69.8	0.0	1.4
30	23719.6	1.125	*a*	14.5	83.3	0.0	2.2

31	24680.2	1.181	*a*	5.6	91.3	0.0	3.0
32	25608.2	1.188	*a*	1.8	94.1	0.0	4.0
33	26502.2	1.162	*a*	1.6	93.1	0.0	5.2
34	27355.8	1.119	*a*	3.4	89.9	0.0	6.7
35	28164.8	1.068	*a*	5.8	85.5	0.1	8.6
36	28923.2	1.017	*a*	8.0	80.7	0.1	11.3
37	29624.0	0.965	*a*	9.5	75.5	0.1	14.9
38	30261.7	0.915	*a*	10.5	70.1	0.1	19.3
39	30837.6	0.872	*a*	10.7	65.2	0.1	24.0
40	31364.9	0.837	*a*	10.8	61.0	0.1	28.1
41	31813.5	1.311	0.563	0.0	0.0	98.3	1.7
42	31857.0	0.810	*a*	10.8	57.8	0.1	31.3
43	32325.2	0.786	*a*	11.1	55.3	0.1	33.5
44	32776.1	0.769	*a*	11.0	53.6	0.1	35.3
45	32794.3	1.290	0.365	0.0	0.0	97.3	2.7
46	33214.6	0.753	*a*	10.9	52.2	0.1	36.7
47	33640.8	0.739	*a*	10.8	51.2	0.1	37.9

48	33741.7	1.263	0.071	0.0	0.1	95.1	4.8
49	34057.4	0.725	*a*	10.6	50.3	0.1	39.0
50	34464.1	0.713	*a*	10.3	49.7	0.1	39.9
51	34625.4	1.214	0.005	0.0	0.4	87.3	12.3
52	34860.9	0.700	*a*	10.0	49.1	0.1	40.8
53	35195.4	0.928	0.001	0.0	6.0	29.5	64.5
54	35247.7	0.684	*a*	10.0	48.5	0.1	41.4
55	35498.1	1.004	0.001	0.0	7.1	47.3	45.6
56	35624.0	0.673	*a*	9.3	48.4	0.1	42.3
57	35896.0	0.942	*a*	0.0	11.1	35.6	53.3
58	35989.2	0.659	*a*	8.7	48.2	0.1	43.0
59	36336.7	0.941	0.001	0.1	13.9	36.9	49.1
60	36342.8	0.646	*a*	8.3	47.7	0.4	43.6
61	36683.7	0.628	*a*	7.9	47.9	0.1	44.1
62	36771.1	0.948	*a*	0.0	15.8	39.6	44.6
63	37011.6	0.612	*a*	7.4	47.9	0.1	44.7
64	37213.7	0.917	0.001	0.0	19.2	34.9	45.9

65	37325.4	0.594	*a*	6.9	47.9	0.1	45.1
66	37624.0	0.576	*a*	6.3	48.0	0.2	45.5
67	37668.6	0.887	0.008	0.0	22.7	30.3	47.0
68	37907.1	0.554	*a*	5.9	48.2	0.1	45.9
69	37907.6	1.024	0.158	0.0	0.9	43.4	55.6
70	38118.6	0.864	0.017	0.0	26.1	27.5	46.4
71	38172.9	0.532	*a*	5.3	48.2	0.1	46.4
72	38420.6	0.508	*a*	4.9	47.8	0.0	47.3
73	38555.6	0.842	0.017	0.0	29.7	27.1	43.3
74	38648.5	0.481	*a*	4.3	46.9	0.0	48.7
75	38855.0	0.451	*a*	3.8	45.2	0.0	50.9
76	38927.5	1.006	0.099	0.0	11.7	54.9	33.4
77	38999.2	0.826	0.173	0.0	23.6	16.6	59.8

a. values are below 10^{-3}

Table IV. 2. Calculated vibronic energies, rotational constants, and Franck-Condon factors for BeC $1^5\Pi$

v	E^a/cm^{-1}	B/cm^{-1}	FCF^b
0	30041.7	1.100	0.451
1	30818.3	1.078	0.329
2	31565.7	1.055	0.145
3	32282.7	1.031	0.052
4	32967.6	1.005	0.017
5	33618.5	0.977	0.005
6	34232.9	0.947	0.002
7	34807.5	0.914	0.001
8	35338.2	0.877	*c*
9	35820.5	0.835	*c*

a. These energies are relative to the v=0 level of $1^5\Sigma^-$

b. Franck-Condon factors for transitions originating from the v=0 level of $1^5\Sigma^-$

c. values are below 10^{-3}

Table IV. 3. Molecular constants derived from the BeC $n^3\Pi$-$X^3\Sigma^-$ bands.

v'-v"	Upper Eigenstate [a]	ν_0 [b]	B" [d]	B' [e]	A_{SO}' [f]
0-0	41	31797.0	1.1624	1.2934	-9.78(8)
1-0	45	32763.8	1.1624	1.2705	-9.65(8)
2-0	48	33705.4	1.1624	1.2513	-9.0(1)
3-0	51	34621.0	1.1624	1.14	-9
4(?)-0	55	35732.0	1.1624	0.9195	-2.15(8)
1-1	41	31862.1	1.1592	1.2705	-9.65(8)

All constants are in units of cm^{-1}.

a. This index refers to the excited states listed in Table IV. 1.

b. Errors in the band origins are ±0.1, except for the 3-0 band. Due to the poor quality of the 3-0 band spectrum, the error for the origin was ±2. The A_{SO}' constant was fixed and the error for B_3' is ±0.02.

c. Irregular rotational structure, could not be reliably assigned.

d. The bands originating from v"=0 were fitted using a common value for B_0" (error of ±0.0030). See text for details.

e. Errors of ±0.0030 cm^{-1}.

f. Errors given in parentheses.

Table IV. 4. Molecular constants derived from the BeC $1^5\Pi$-$1^5\Sigma^-$ bands.

v'-v"	ν_0	B"[a]	B'[b]	A_{SO}'[c]
1-0	30791.7	1.229	1.040	-0.4(3)
2-0	31507.8	1.229	1.017	-0.4(3)
3-0	32193.0	1.229	1.003	-0.5(3)

All constants are in units of cm^{-1}.

a. The bands originating from v"=0 were fitted using a common value for B_0" (error of ±0.004).

b. Errors of ±0.004 cm^{-1}.

c. Errors given in parentheses.

Table IV. 5. Positions of the rotational contour maxima for unassigned bands of BeC

33074	35731
33475	36146
33948	36576
34061	37042
34624	37928[a]
34824	38942
35274	

Energies in cm^{-1}, with uncertainties of ±5 cm^{-1}.

a. A rotationally resolved spectrum for this band is shown in Fig. 13 of ref. 15, with structure that is consistent with a $^3\Pi$-$^3\Sigma^-$ transition. Note that a calibration error in the energy scale was not taken into account, and the band origin was given as 37942 cm^{-1}. The corrected value is 37927.5 cm^{-1}. The upper state is close in energy to eigenstate 69 of Table IV. 1, but the fitted rotational constant (B'=0.735 cm^{-1}) is significantly smaller.

Table IV. 6. Comparison of observed and theoretically predicted transition energies for the rotationally resolved bands of BeC

	Obs/ cm^{-1}	Calc/ cm^{-1}	Obs-Calc/ cm^{-1}	FCF
$3^3\Pi$-$X^3\Sigma^-$				
0,0	31797.1	31813.5	-16.4	0.563
1,1	31862.1	31874.8	-12.7	-
1,0	32763.8	32794.3	-30.5	0.365
2,0	33705.4	33741.7	-36.3	0.071
3,0	34621.0	34625.4	-4.4	0.005
4(?),0	35732.0	35498.1	233.9	0.001
$1^5\Pi$-$1^5\Sigma^-$				
1,0	30791.7	30818.3	-26.4	0.329
2,0	31507.8	31565.7	-57.9	0.145
3,0	32193.0	32282.7	-89.7	0.052

Table IV. 7. MRSD-CI theoretical predictions and observed spectroscopic constants for BeC

$X^3\Sigma^-$

T_0	ω_e	$\Delta G_{1/2}$	R_e	B_0	Ref
0	905	-	1.69	-	[2]
0	951	934	1.67	1.173	[1]
0	938	919	1.66	1.178	[15]
0	-	902	-	1.162	Exp.

$1^5\Sigma^-$

2295	978	-	1.64	-	[2]
1823	1035	1021	1.62	1.242	[1]
2060	1036	1020	1.60	1.250	[15]
2302	-	-	-	1.229	Exp.

$1^5\Pi$

31437	707	-	1.76	-	[2]
32503	808	777	1.70	1.101	[15]
32316	778	747	-	1.058[a]	Exp.

All constants are in cm^{-1} units, with the exception of R_e, which is given in Å

a. Extrapolated from the constants for the v'=1,2, and 3 levels.

Figure IV.1. Electronic states of BeC plotted in adiabatic (on left) and diabatic (on right) representations. The zero of energy is the minimum of the $X^3\Sigma^-$ ground state (black), with the four lowest $^3\Pi$ states appearing above (in color).

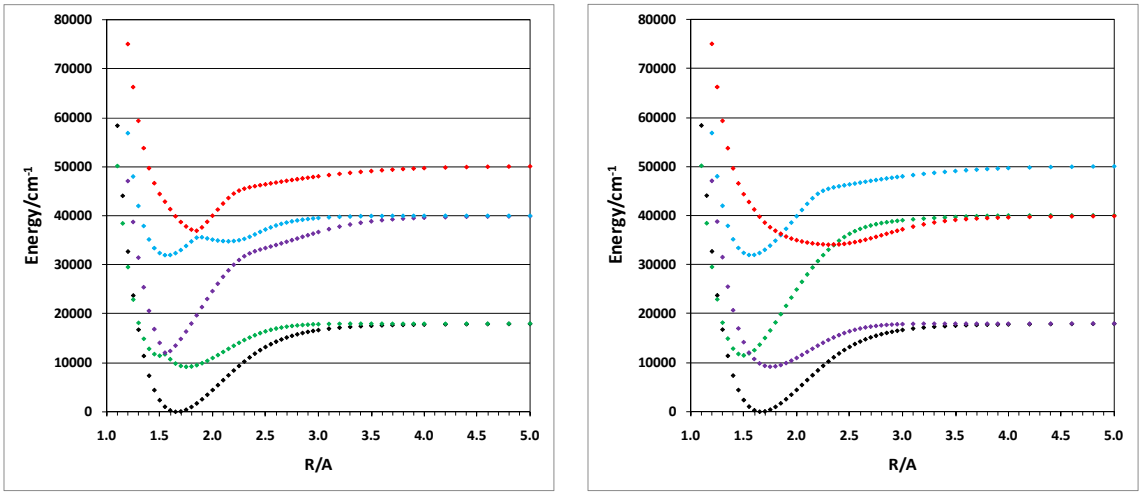

Figure IV.2. Calculated adiabatic potential energy curves for the $X^3\Sigma^-$ (black) $1^5\Sigma^-$ (blue) and $1^5\Pi$ (red) states.

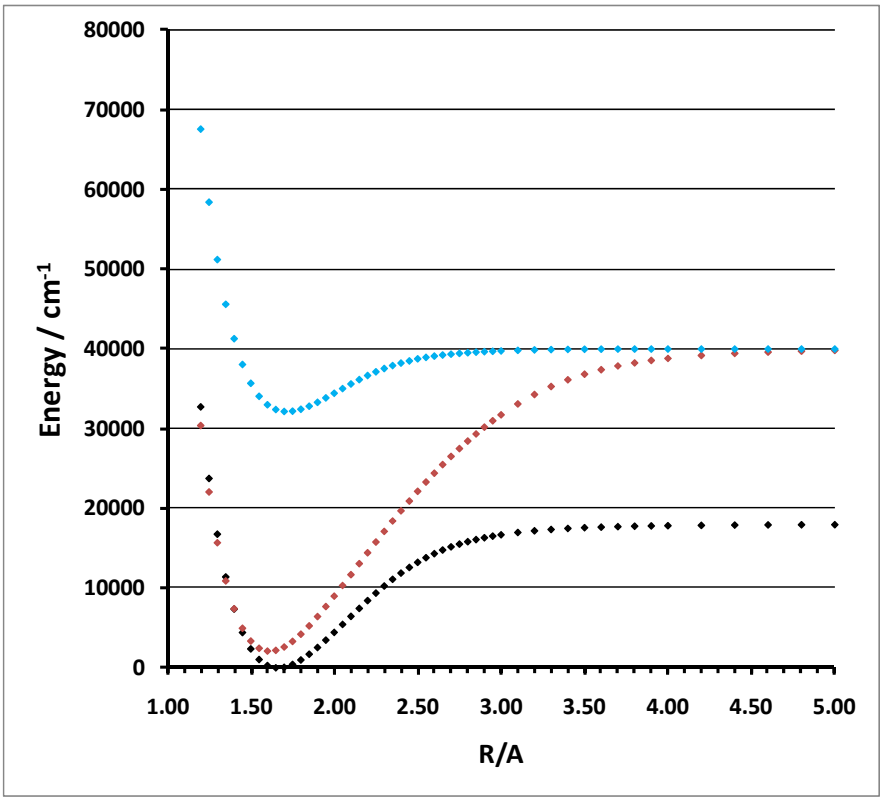

Figure IV.3. Low resolution REMPI spectrum for BeC, recorded with detection of the ion at m/*z*=21. This trace is composed of multiple scans that were obtained using several laser dyes. The relative intensities have not been corrected for variations in the laser power. For the assigned features, T and Q indicate the $3^3\Pi$-$X^3\Sigma^-$ and $1^5\Pi$-$1^5\Sigma^-$ transitions, respectively.

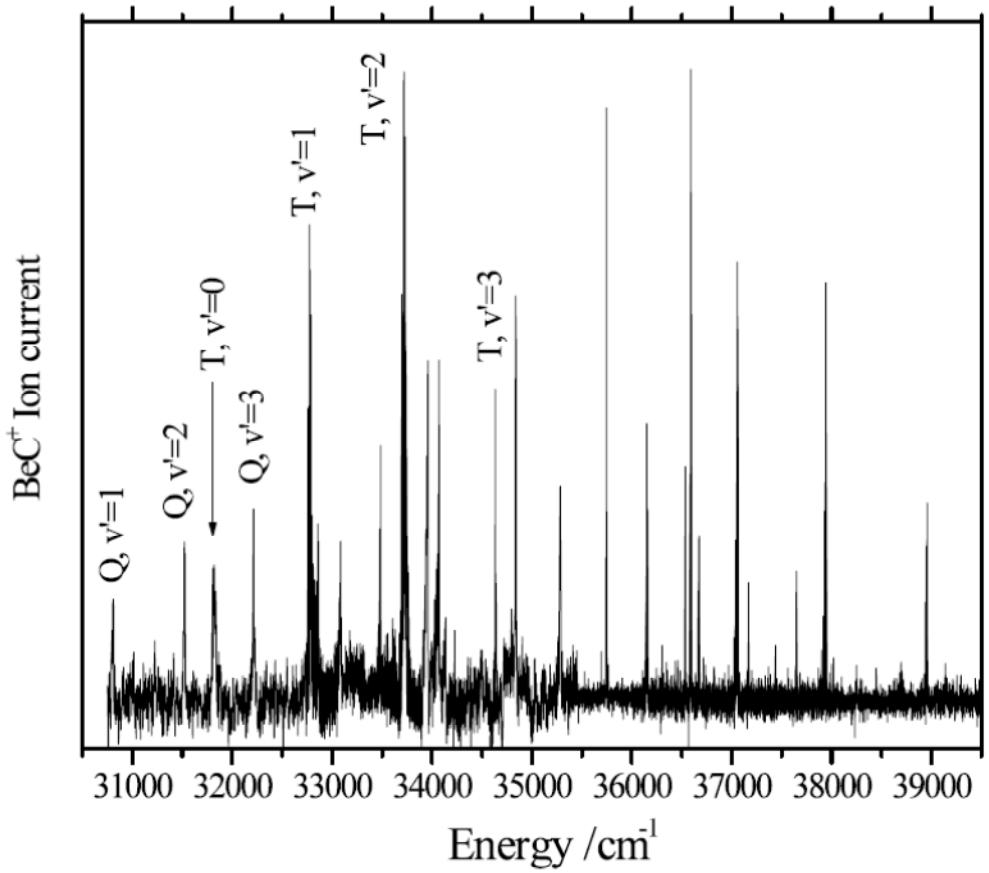

Figure IV.4. Rotationally resolved spectrum of the $3^3\Pi$- $X^3\Sigma^-$ 1-0 band. The downward going trace is a simulation with an assumed rotational temperature of 90K.

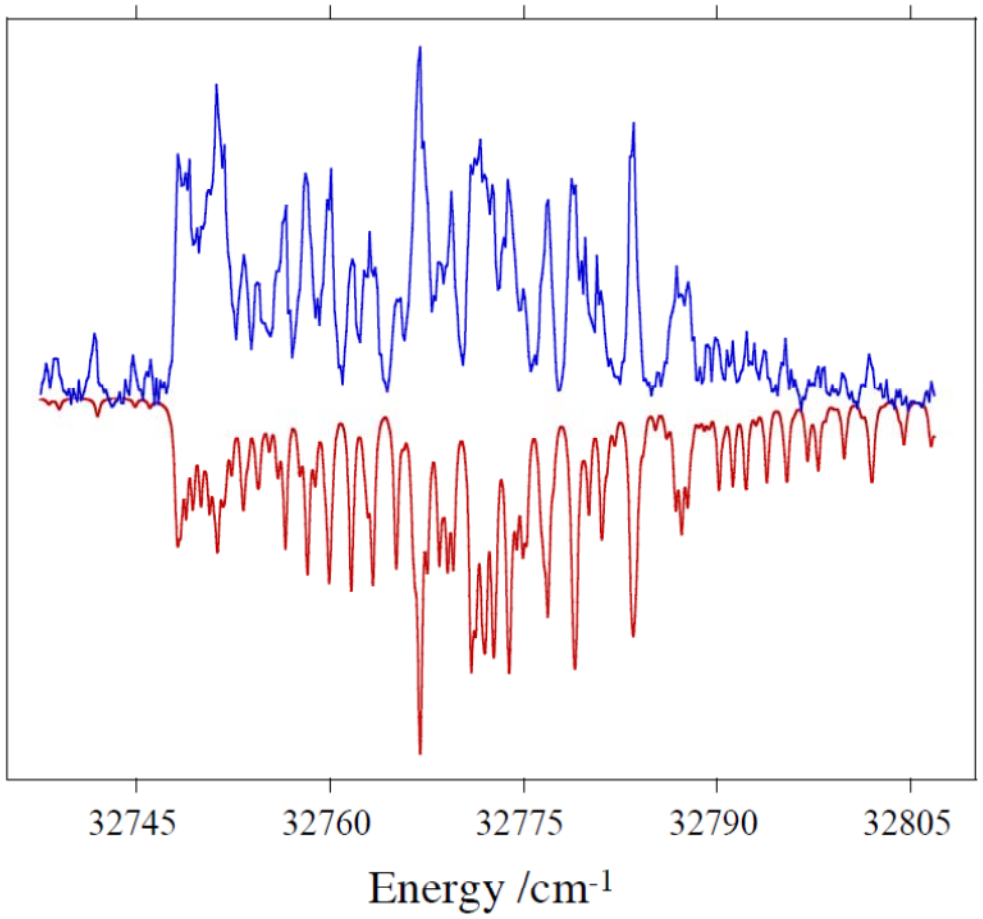

Figure IV.5. Rotationally resolved spectrum of the $1^5\Pi$- $1^5\Sigma^-$ 1-0 band. The downward going trace is a simulation with an assumed rotational temperature of 90K.

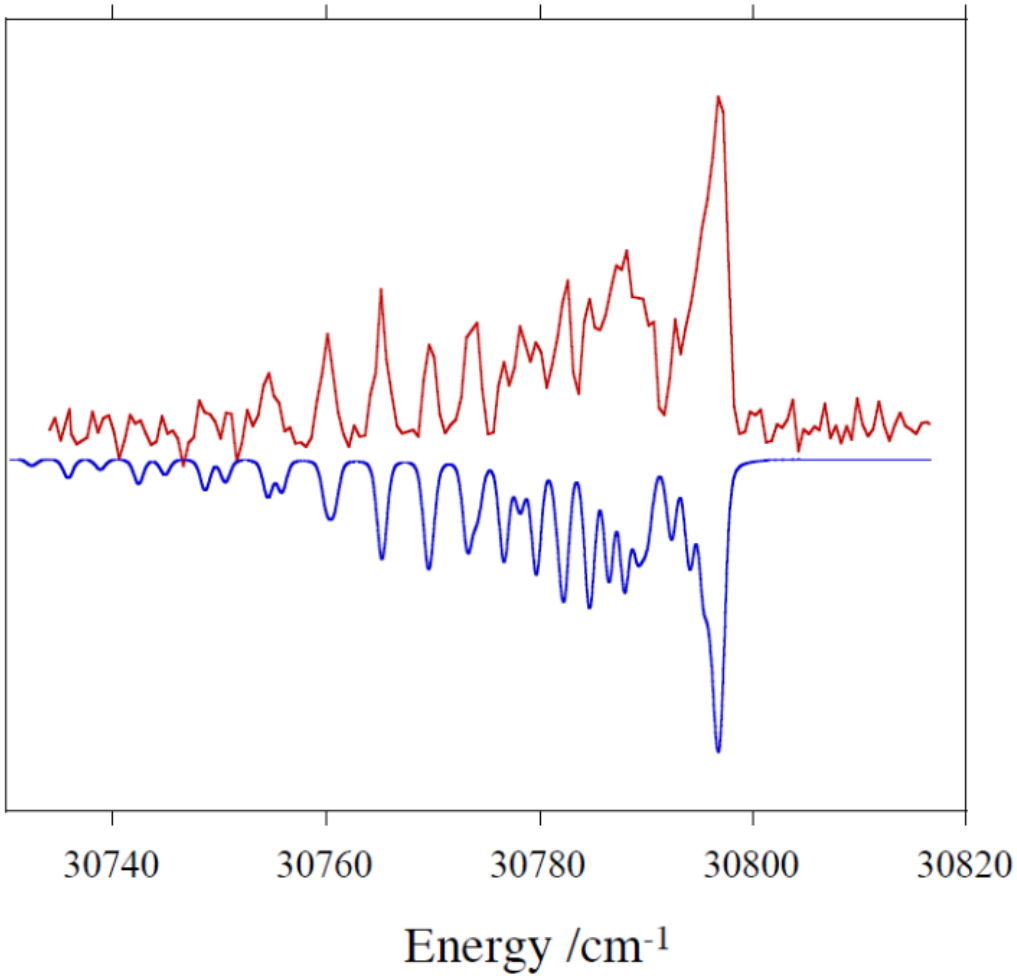

CHAPTER V

LOW-LYING STATES OF HFS^+ AND THE IONIZATION ENERGY OF HFS

V.1 INTRODUCTION

The group IVb metal binary sulfides have been studied for more than 20 years. One reason for the interest in these molecules is the presence of TiS and ZrS in the spectra of S-type stars [1-4]. They also present relatively simple systems where the extent to which the d-orbitals participate in bonding may be examined. The primary motivation for the study of Hf species in our laboratory derives from the similarity between the electronic structures of atomic Th [5-7] and Hf [8-11]. The ground state electron configuration of atomic Th $7s^26d^2$ is isoelectronic with Hf $6s^25d^2$. Previously we had found that ionization of both HfO and ThO caused the vibrational frequencies to increase, and the bond lengths to contract. These changes suggest that the binding energies increase, but ionization energy measurements show that the binding energies actually decrease (by 1 eV in the case of HfO) [6,11]. Our recent studies of the HfF/HfF^+ and ThF/ThF^+ pairs have revealed the same behavior for the fluorides [8,9]. The present study extends this investigation of the effects of ionization on Hf-X bonds to HfS. Spectroscopic constants for the low-energy states of HfS^+ and the ionization energy of HfS are reported.

HfS has been studied by several groups since 1994, when the gas phase emission spectrum was first recorded by Jonsson et al. [1] They identified six band systems in the region 11000-21000 cm^{-1}, that were initially assigned as singlet-singlet transitions. Subsequently, Launila et al. [12] examined emission in the 4700-6900 cm^{-1} range, and concluded that two of the excited states observed by Jonsson et al. [1] should be re-assigned as triplet states (b $^3\Pi_{0^+}$ and b $^3\Pi_1$). They also confirmed that the ground state was Hf $6s\sigma^2$ X $^1\Sigma^+$, with the first excited states

(a $^3\Delta_\Omega$) arising from the Hf 6sσ5dδ configuration. High-resolution laser induced fluorescence (LIF) spectra for the b $^3\Pi$-X $^1\Sigma^+$ bands were reported by Leung et al. [13]. Microwave data for seven isotopologues of HfS were obtained by Cooke and Gerry[4], providing highly accurate molecular constants for the *v*=0-6 vibrational levels of the electronic ground state. Two-color laser ionization measurements have been used to determine the radiative lifetime [3] and dipole moment [14] of the D$^1\Pi$ state. Infrared absorption spectra of HfS in solid argon and DFT/B3LYP level theory calculations were carried out by Liang et al.[15] To our knowledge, there are no published experimental data or *ab initio* theoretical calculations for HfS^+.

V.2 EXPERIMENTAL

The apparatus used in this study has been described in Section II so only a brief description will be given here. HfS was produced using a laser ablation source. The 1064 nm output of a pulsed Nd/YAG laser was focused onto the surface of a hafnium rod. The rod was continuously rotated and translated to expose a fresh surface for each shot. A pulsed solenoid valve, located behind the hafnium rod, produced a gas pulse which served to entrain the ablated material into a carrier gas consisting of He + 0.1% CS_2. The mixture was then subjected to supersonic expansion, thereby cooling the ablation products. The backing pressure and gas pulse duration were typically 20-25 PSI and 270 μs.

Laser induced fluorescence (LIF) spectra were recorded with the excitation laser positioned approximately 5 cm downstream from the expansion nozzle orifice. The output from a Continuum ND 6000 dye laser/Nd:YAG laser system was propagated perpendicularly to the direction of the gas expansion. Fluorescence was collected along an axis that was perpendicular to both the laser and gas expansion axes. The fluorescence was detected by a Photonis XP2020 photomultiplier tube.

Downstream of the LIF detection region, the core of the jet expansion entered a second differentially pumped chamber via a conical skimmer with a 5 mm orifice. This chamber housed a time-of-flight mass-spectrometer (TOFMS) operating with a 250 V/cm field between the repeller and extractor plates. In the TOFMS the molecular beam was crossed by two counter-propagating beams from tunable dye lasers (Continuum ND6000 and a Coherent ScanMate Pro). Two-color two-photon (1+1') resonantly enhanced multiphoton ionization (REMPI) spectra were recorded by scanning the Coherent ScanMate Pro dye laser to search for resonant intermediate excited states, ionizing the excited molecules with the ND6000 dye laser and recording the resulting mass spectrum. One color (1+1) REMPI spectra were recorded with the Continuum ND6000 dye laser alone when the energy of the first photon was greater than 1/2 of the molecule's ionization energy. For the two-color spectra the laser beams were temporally overlapped and synchronized with the pulsed molecular beam using digital delay generators.

Photoionization efficiency (PIE) spectra were recorded to determine the ionization energy of HfS using the same experimental arrangement as that for REMPI. The only difference being that the pump laser wavelength was fixed on a known transition of neutral HfS, and the ionization laser was scanned until the onset of HfS^+ ion signal was observed in the mass spectrometer.

Pulsed field ionization zero electron kinetic energy (PFI-ZEKE) spectra[16] were recorded for the HfS^+ molecular ion using a two-color scheme via a resonant intermediate state. For these measurements the repeller and the extractor electrodes were held at -4.0V to give field free conditions during photo-excitation. After a 1.5 μs time delay a voltage pulse was applied to the extractor electrode to give an electric field of 1.43 V/cm causing ionization of the remaining molecules in long-lived high-*n* Rydberg states and accelerating the electrons towards the MCP detector located 10 cm below the repeller electrode. Transitions in the PFI-ZEKE spectra were confirmed to belong to HfS by detuning the pump laser from resonance with the intermediate state.

The LIF and REMPI spectra typically displayed a resolution of about 0.10-0.15 cm^{-1}, while rotationally resolved PFI-ZEKE spectra displayed a resolution of about 1.5 cm^{-1}. LIF and REMPIE spectra were calibrated from observed atomic Hf or Zr lines**.** PFI-ZEKE data were calibrated by recording either the I_2 B-X LIF spectrum using the fundamental output from the dye laser or for spectra taken at higher energies, the B $^2\Pi$-X $^2\Pi$ transition of NO was recorded using the second harmonic.

V.3 AB INITIO CALCULATIONS

Calculations were carried out at the CASSCF/MRCI+Q level (complete active space self-consistent field multi-reference configuration interaction with the Davison size extensive correction) of theory as implemented in the MOLRPO 2010.2 suite of programs [17]. Our calculations employed the aug-cc-pVTZ basis set of Woon et al. [18] for the sulfur atom as taken from the MOLRPO 2010.2 basis set library. The basis set used for Hf was the effective core potential denoted as aug-cc-pVTZ-PP ECP60MDF developed by Figgen et al. [19] The ECP has a 60 electron, $[Kr]4d^{10}4f^{14}$, core. It contained parameters for calculating the spin-orbit interaction energy and was optimized to recover the scalar relativistic effects.

The CASSCF/MRCI + Q calculations for HfS^+ were carried out in several steps. The $X^2\Sigma^+$, $^2\Pi$ and $^2\Delta$ electronic states were included in the state-averaged CASSCF, with equal weighting. The state averaged CASSCF wavefunction was then used as the reference for the internally contracted MRCI + Q calculation which included the Davidson correction. Finally the SOC (spin-orbit coupling) was calculated using the Breit-Pauli operator. The off-diagonal SO-matrix elements were determined using the converged CASSCF wavefunctions, and the diagonal elements were set to the MRCI+Q energies. Potential energy curves (PEC) were calculated up to about 20,000 cm^{-1} above the minimum for each electronic state. To derive spectroscopic

constants, the nuclear Schrödinger equation was solved variationally for each PEC using the program LEVEL 8.0.[20]

Calculations for the ground electronic state of the neutral were preformed at the CASSCF/MRCI+Q level for the $X^1\Sigma^+$ state. The calculation had an active space of 8 electrons distributed among 10 orbitals. The remaining molecular orbitals were kept doubly occupied, but fully optimized. The orbitals used to define the active space were S-3sσ, -3pσ and -3pπ and Hf -6sσ, -5dσ, -5dπ and -5dδ. Expanding the active space beyond this group increased the cost of the calculation substantially. As the ground state is a closed-shell singlet, interactions with other low-lying electronic states such as $^3\Pi$ or $^3\Delta$ were expected to have only a minimal effect. Examination of the electronic wavefunction at the equilibrium distance shows that the $X^1\Sigma^+$ state is somewhat multi-configurational, with a leading configuration that is 82% Hf $6s\sigma^2$, S $3p\sigma^2 3p\pi^4$.

For HfS^+, CASSCF/MRCI+Q calculations were performed on the ground and lowest energy doublet states ($X^2\Sigma^+$; $^2\Delta_{3/2}$; $^2\Delta_{5/2}$; $^2\Pi_{1/2}$; $^2\Pi_{3/2}$). The active space was the same as that used for the neutral molecule. Tests were preformed that included the low-lying quartet states ($^4\Sigma^-$ and $^4\Pi$) and excited doublet states. These were found to be well above ground and first two electronically excited states of HfS^+, with energies that were at least a few hundred cm^{-1} higher than the $^2\Pi_{3/2}$ state. Including the quartet and additional excited doublet states revealed a high density of states above the $^2\Pi_{3/2}$ state. Consequently, only the doublet states were included in the final calculations. The PEC's of the ground and first two electronically excited states within at least 15,000 cm^{-1} of the ground state minimum, were of satisfactory quality without including the quartet or excited doublet states. However, it is likely that the PEC's for the $^2\Pi$ states could be improved by including the quartet states.

The results of the CASSCF/MRCI+Q+SOC calculations for HfS^+ and HfS are summarized in Table V.1.

V.4 EXPERIMENTAL RESULTS

Figure V.1 displays a rotationally resolved LIF spectrum for the origin band of the $D^1\Pi$-$X^1\Sigma^+$ transition of HfS. The lower trace is a simulated spectrum generated by the program PGPOHER[21] with an estimated rotational temperature of 17 K. The molecular constants used in this simulation were taken from reference [14]. Note that Hf has six naturally occurring isotopes (^{180}Hf (35.1%), ^{179}Hf (13.6%), ^{178}Hf (27.3%), ^{177}Hf (18.6%), ^{176}Hf (5.3%), and ^{174}Hf (0.2%)). However, the isotopic splitting was not resolved for the origin band due to the similarity of the upper and lower state molecular constants.

Photoionization efficiency (PIE) measurements were carried out by scanning the ionization laser over the range 44200-45600 cm^{-1}, with the pump laser set to excite the unresolved R-branch bandhead feature the $D^1\Pi$-$X^1\Sigma^+$ transition at 17054 cm^{-1}. Figure V.2 shows the PIE curve, which indicates an ionization threshold at 44800 cm^{-1}. Adding the energy of the intermediate state to the onset, and correcting for the lowering of the ionization energy (IE) due to electric field in the mass spectrometer ($\Delta E = 6\sqrt{F(V/cm)}$)[16], the PIE curve yielded a value of 61930(40) cm^{-1} for the ionization energy. The error range reflects the uncertainty in identifying the threshold position for the curve and the excitation of several R-branch bandhead rotational lines by the pump laser.

Rotationally resolved PFI-ZEKE spectra of the origin band of HfS^+ are shown in Fig. V.3. These spectra were taken using intermediate excitation of resolved P-branch (or R-branch for J=2) lines of the $D^1\Pi$-$X^1\Sigma^+$ transition. A notable characteristic of the PFI-ZEKE spectra is that they show lines with J values that are close to that of the intermediate excited state. This behavior is evident in Fig.V.4. As the resolution of the low-J lines was incomplete, it was necessary to observe lines with higher J values, in order improve the definition of the rotational constant. To obtain these data the expansion conditions were adjusted to increase the rotational

temperature. It was found that temperatures up to 70 K could be achieved by adjusting the pulse duration of the solenoid valve, yielding significant populations in levels as high as J=25.

Fitting the PFI-ZEKE line positions to the rigid rotor energy level expression,

$$E = T_{e,v} + B_{e,v}J(J+1)$$

yielded a reasonably well defined rotational numbering for the spectrum, but the variance of the fit was such that changing the numbering by ±1 unit produced acceptable results. However, the disagreement with the constant predicted by the ab initio calculations (c.f. Table V.1) was unreasonably large when the optimal numbering was changed. Ionization energies of individual J states were determined using the blue edge of each feature. The blue edge was determined by adding the FWHM of each peak to its line center. This analysis gave an IE of 61934(3) cm^{-1} and a ground state rotational constant for the HfS^+ cation of B_0^+=0.130(8) cm^{-1}.

A different intermediate state was used to obtain PFI-ZEKE spectra of the low-lying electronically excited states of HfS^+. Because the $D^1\Pi$-$X^1\Sigma^+$ transition is at a relatively low energy, a second photon energy of about 44900 cm^{-1} (222.7 nm) was needed to ionize HfS. Going to higher energy photons, the generation of background electrons in our apparatus became an increasingly problematic source of noise. Consequently, we searched for higher energy excited states of neutral HfS that would be suitable intermediates for accessing the excited states HfS^+, without having to increase the second photon energy above 45000 cm^{-1}. Previous studies of neutral HfS focused on the visible spectral range. A search for a suitable electronic state near half the IE (about 31000 cm^{-1}) was carried out using REMPI and LIF. The spectrum of HfS was rather dense in this region, but an intense band that was free from overlapping transitions was found at 31683.7 cm^{-1}. This band shown in Fig.V.4 had a rotational envelope consistent with a $^1\Pi$-$^1\Sigma^+$ transition. PIE spectra confirmed that this transition originated from the ground electronic state, and we label this transition as $[31.68]^1\Pi$-$X^1\Sigma^+$. Multiple unresolved Q-branch features are evident, due to the different band origins of the 5 major HfS isotopologues. Rotational structure

could not be resolved using LIF due to the isotopic splitting, but an estimate of B_e' was found from simulations made using PGOPHER simulations with $B_{e,v}' \approx 0.112$ cm^{-1}. REMPI spectra were collected while monitoring each isotopologue and the splitting observed in Fig.V.5 was demonstrated to correlate with the major isotopologues of HfS. The vibrational quantum number of the upper state was estimated using the vibrational isotope shift, given by the approximate relationship

$$\Delta E = (1-\rho)\omega_e(v+1/2)$$

where v is vibrational quantum number, ω_e is the harmonic vibrational constant of the reference isotopologue and $\rho = \sqrt{\mu/\mu_i}$. μ and μ_i are the reduced masses of reference and shifted isotopologues, respectively. The value of ω_e for the upper electronic state was not measured, but we assume that it is similar to other $^1\Pi$ excited electronic states (ω_e=470-500 cm^{-1}, see reference 1). For two adjacent HfS isotopologues, e.g., ^{179}HfS and ^{180}HfS, the splitting between the Q-branches was about ~0.9 cm^{-1} for ρ=0.99956. Using these values in the above equation indicates v=4 as the upper state vibration quantum number.

PFI-ZEKE spectra of the $^{180}HfS^+$ cation were recorded with the pump laser tuned to the Q-branch of the [31.68]$^1\Pi$-X$^1\Sigma^+$ transition at 31684.7 cm^{-1}. The ionization laser was scanned from the onset of ionization to about 9600 cm^{-1} above threshold. Figure V.5 shows the lower energy part of the scan, with intense bands that correspond to v=0 to 6 levels of the ground electronic state. The sharp features near v=2 and v=6 have not been identified. They could be observed without the pump laser and most likely arise from Hf + 2hν $\rightarrow$ Hf^+ + e^- resonant two-photon processes. Rotationally resolved PFI-ZEKE spectra were not obtained using the [31.68]$^1\Pi$-X$^1\Sigma^+$ transition because several rotational levels were excited simultaneously.

The vibration progression observed in the PFI-ZEKE spectrum was highly non-Frank-Condon in nature, and a total of 19 vibrational levels of the $X^2\Sigma^+$ state, and the v=0-8 and v=0-2 vibrational levels first and second electronically excited states were found and assigned. Table

V.2 presents vibronic term energies for the low-lying states, determined by fitting the "center-of-mass" of each band. The vibronic term energies were fitted to the anharmonic oscillator equation to obtain vibrational constants,

$$T_{e,v} = T_{e,0} + \omega_e v - \omega_e x_e v(v+1)$$

Spectroscopic constants obtained from the PFI-ZEKE spectra are summarized in Table V.3, along with spectroscopic constants for the ground electronic state of the neutral HfS [14].

V.5 DISCUSSION

Overall the results from the *ab initio* calculations agree well with the experimental data. The calculations unambiguously support assignment of the ground electronic state observed in the PFI-ZEKE spectra as $X^2\Delta$, and the two observed excited electronic states are readily identified as the Ω=3/2 and 5/2 components of the $^2\Delta$ state. The calculated energy difference between the $X^2\Sigma$ and $^2\Delta_{3/2}$ states is within 100 cm^{-1} of the experimental value (5187 vs. 5265 cm^{-1}), and the spin-orbit splitting between the Ω components of the $^2\Delta$ states are also in good agreement (2800 vs. 2754 cm^{-1}). The latter result indicates that the SO-ECP basis set describes the spin-orbit interaction adequately for Hf. While the predicted vibrational frequencies are too low by about 15 cm^{-1}, the increase in vibrational frequency between the ground electronic states of the neutral and the ion (about 27 cm^{-1}) is reproduced. For the cation, the difference in vibrational frequencies between the $X^2\Sigma$ and $^2\Delta$ states is also reproduced. Note also that the calculated adiabatic ionization energy is in reasonably good agreement with the experimental value.

The dissociation energies have not been measured for the neutral or the cation, but the difference in bond energies can be found by using the ionization energy of the neutral molecule and atom, and is defined by expression

$$IE(HfS) - IE(Hf) = D_0^+ - D_0$$

The most recent value for IE of Hf atom[22] is 6.82507(4) eV and the IE(HfS) measured in this work is 7.6788(2) eV. Therefore the HfS is more deeply bound than the HfS^+ by 0.8537 eV. At the same time, the vibrational frequency increases in the ion by 23.2 cm^{-1} and the bond shortens by 0.05 Å. As noted in the introduction, the same trends have been observed in ThX/ThX^+ [6,8] and HfX/HfX^+ [9,11] pairs (X=O, F), where the bond shortens and the vibrational frequency increases on ionization, but the dissociation energy decreases. The changes in force constants $k^+/k=(\omega_e^+/\omega_e)^2$, bond energies and bond lengths for HfS/HfS^+, ThO/ThO^+ and HfO/HfO^+ are collected in Table V.4. The effect of ionization on the bonding properties of HfS was comparable to that seen for HfO. By comparison, ThO has smaller change in bond energy and bond length, but a more significant change in the force constant ($k^+/k=(\omega_e^+/\omega_e)^2$). In future work it will be of interest to compare the properties of ThO/ThO^+ with those of ThS/ThS^+. Gas phase spectra have not yet been reported for ThS or ThS^+, but it is probable that these molecules will be observable using the techniques used here for HfS/HfS^+.

REFERENCES

(1) Jonsson, J.; Edvinsson, G.; Taklif, A. G. *Phys. Scr.* **1994**, *50*, 661-5.

(2) Bernath, P. F. *Int. Rev. Phys. Chem.* **2009**, *28*, 681-709.

(3) Aldener, M.; Hansson, A.; Pettersson, A.; Sassenberg, U. *J. Mol. Spectrosc.* **2002**, *216*, 131-135.

(4) Cooke, S. A.; Gerry, M. C. L. *J. Mol. Spectrosc.* **2002**, *216*, 122-130.

(5) Heaven, M. C. *Phys. Chem. Chem. Phys.* **2006**, *8*, 4497-4509.

(6) Goncharov, V.; Heaven, M. C. *J. Chem. Phys.* **2006**, *124*, 064312/1-064312/7.

(7) Goncharov, V.; Han, J.; Kaledin, L. A.; Heaven, M. C. *J. Chem. Phys.* **2005**, *122*, 204311/1-204311/6.

(8) Barker, B. J.; Antonov, I. O.; Heaven, M. C.; Peterson, K. A. *J. Chem. Phys.* **2012**, *136*, 104305/1-104305/9.

(9) Barker, B. J.; Antonov, I. O.; Bondybey, V. E.; Heaven, M. C. *J. Chem. Phys.* **2011**, *134*, 201102/1-201102/4.

(10) Stoll, H.; Peterson, K. A.; Merritt, J. M.; Heaven, M. C. *J. Phys. Chem. A* **2009**, *113*, 12353-12355.

(11) Merritt, J. M.; Bondybey, V. E.; Heaven, M. C. *J. Chem. Phys.* **2009**, *130*, 144503/1-144503/9.

(12) Launila, O.; Jonsson, J.; Edvinsson, G.; Taklif, A. G. *J. Mol. Spectrosc.* **1996**, *177*, 221-231.

(13) Leung, J. W. H.; Tam, W. S.; Ran, Q.; Cheung, A. S. C. *J. Mol. Spectrosc.* **2003**, *217*, 93-95.

(14) Hansson, A.; Pettersson, A.; Royen, P.; Sassenberg, U. *J. Mol. Spectrosc.* **2004**, *224*, 157-163.

(15) Liang, B.; Andrews, L. *J. Phys. Chem. A* **2002**, *106*, 6295-6301.

(16) Muller-Dethlefs, K.; Schlag, K. *Ann. Rev. Phys. chem.* **1991**, *42*, 109-136.

(17) Werner, H.-J.

(18) Woon, D. E.; Dunning, T. H., Jr. *J. Chem. Phys.* **1993**, *98*, 1358-71.

(19) Figgen, D.; Peterson, K. A.; Dolg, M.; Stoll, H. *J. Chem. Phys.* **2009**, *130*, 164108/1-164108/12.

(20) LeRoy, R. J.

(21) Western, C. M.; University of Bristol: 2007.

(22) Callendar, C. L.; Hackett, P. A.; Rayner, D. M. *J. Opt. Soc. Am. B* **1988**, *5*, 1341.

Table V.1. Term energies and molecular constants from CASSCF/MRCI+Q calculations.

	HfS, $X^1\Sigma^+$	HfS^+, $X^2\Sigma^+$	$^2\Delta_{3/2}$	$^2\Delta_{5/2}$	$^2\Pi_{1/2}$	$^2\Pi_{3/2}$
T_o	-60167[a]	0	5187	7986	14224	14696
ω_e	512.5	539.3	511.5	512.5	413.0	412.5
$\omega_e x_e$	1.17	1.34	1.30	1.31	0.72	0.99
R_e	2.1911	2.1537	2.1834	2.1810	2.3310	2.3348
B_e	0.1293	0.1339	0.1303	0.1305	0.1143	0.1139
R_0	2.1927	2.1553	2.1851	2.1829	2.3310	2.3368
B_o	0.1292	0.1337	0.1301	0.1303	0.1141	0.1137

a. The first data column gives results for neutral HfS, with the term energy referenced to the ground state zero-point level of HfS^+. Subsequent columns give the results for the ion. The energies are given in cm^{-1} units, and the distances in Å.

Table V.2. Vibronic term energies for the low-lying states of $^{180}HfS^{+}$.

v	$X\,^2\Sigma^+$	$^2\Delta_{3/2}$	$^2\Delta_{5/2}$
0	0	5265	8019
1	552	5791	8545
2	1101	6313	9068
3	1648	6832	9589
4	2191	7349	
5	2732	7863	
6	3270	8374	
7	3805	8884	
8	4337	9391	
9	4867		
10	5394		
11	5919		
12	6440		
13	6957		
14	7473		
15	7985		
16	8494		
17	9001		
18	9508		

Energies are given in units of cm^{-1}, with errors of ± 3 cm^{-1}.

Table V.3. Spectroscopic constants for ^{180}HfS and ^{180}HfS$^+$.

	HfS, $X^1\Sigma^+$	HfS^+, $X^2\Sigma^+$	HfS^+, $^2\Delta_{3/2}$	HfS^+, $^2\Delta_{5/2}$
v range	-	0-18	0-8	0-3
T_0	-61933(3)	0	5265(3)	8019(3)
ω_e	526.8480(12)	554.9(5)	527.4(10)	529(3)
$\omega_e\chi_e$	1.23453(21)	1.41(10)	1.3(1)	1.5(5)
B_0	0.13336(4)	0.130(8)	-	-

Units are cm^{-1}.

Table V.4. Effect of ionization on the vibrational constants and bond lengths of HfS, HfO and ThO.

	HfS/HfS$^+$	HfO/HfO$^+$	ThO/ThO$^+$
ΔD_0 (eV)	-0.8537	- 1.092	- 0.3
$(\omega_e^+/\omega_e)^2$	1.110	1.092	1.137
Δr_0 Å	- 0.05	- 0.038	- 0.033

Data for HfO and ThO are from references [11] and [6].

Figure V.1. Laser induced fluorescence spectrum of the $D^1\Pi$-$X^1\Sigma^+$ 0-0 band. The downward-going trace is a simulation with an assumed rotational temperature of 17 K.

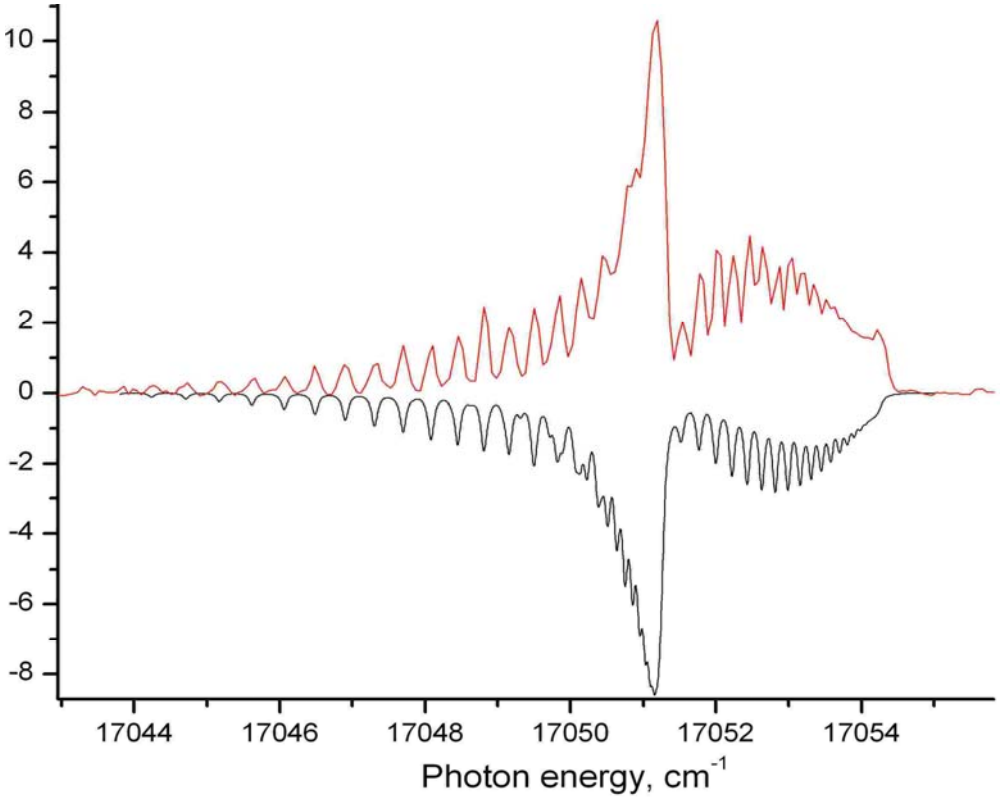

Figure V.2. Photoionization efficiency curve recorded with the first laser tuned to the R-branch bandhead feature of the $D^1\Pi$-$X^1\Sigma^+$ 0-0 band at 17054 cm^{-1}. The lines drawn through the data indicate the method used to estimate the onset of ionization.

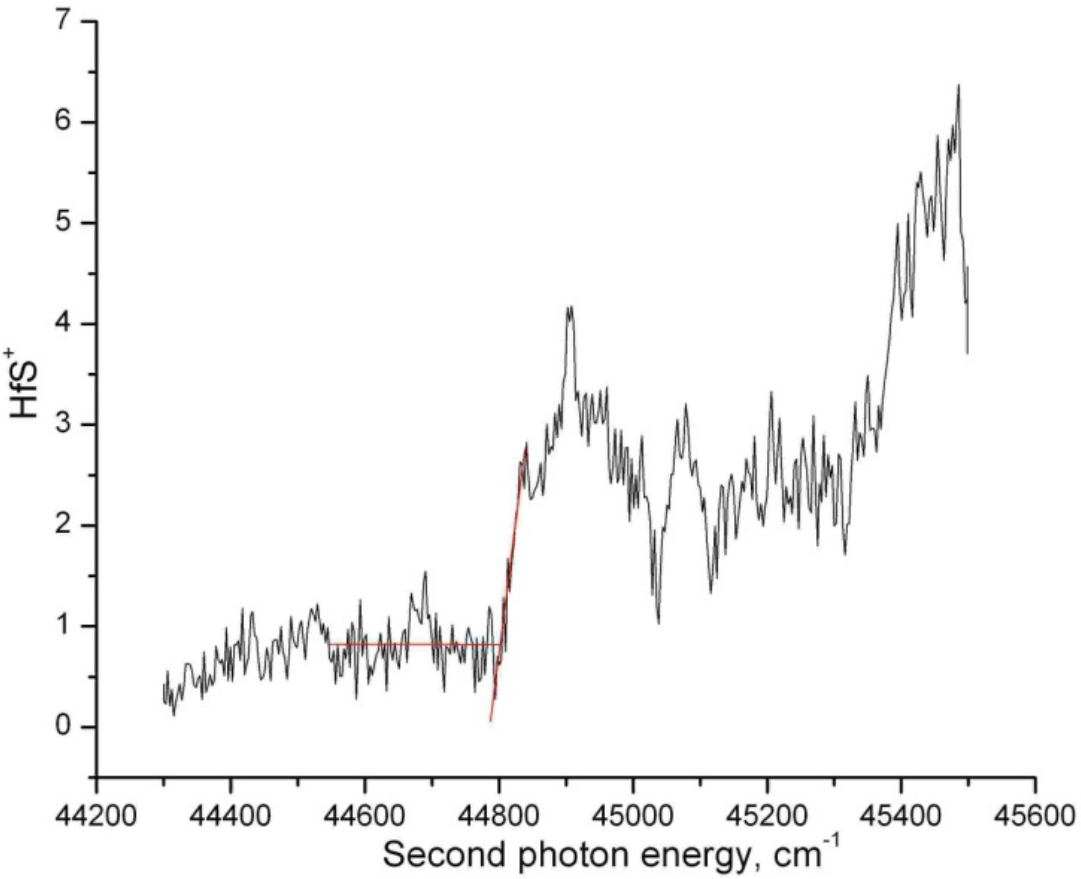

Figure V.3. PFI-ZEKE spectra for the $X^2\Sigma^+$, v=0 state of the HfS^+ ion. These traces were recorded using initial excitation of the P(J+1) or R(J-1) lines of the $D^1\Pi$-$X^1\Sigma^+$ 0-0 band. Transitions terminating on the J=2 – J=24 levels the $D^1\Pi$ state were used.

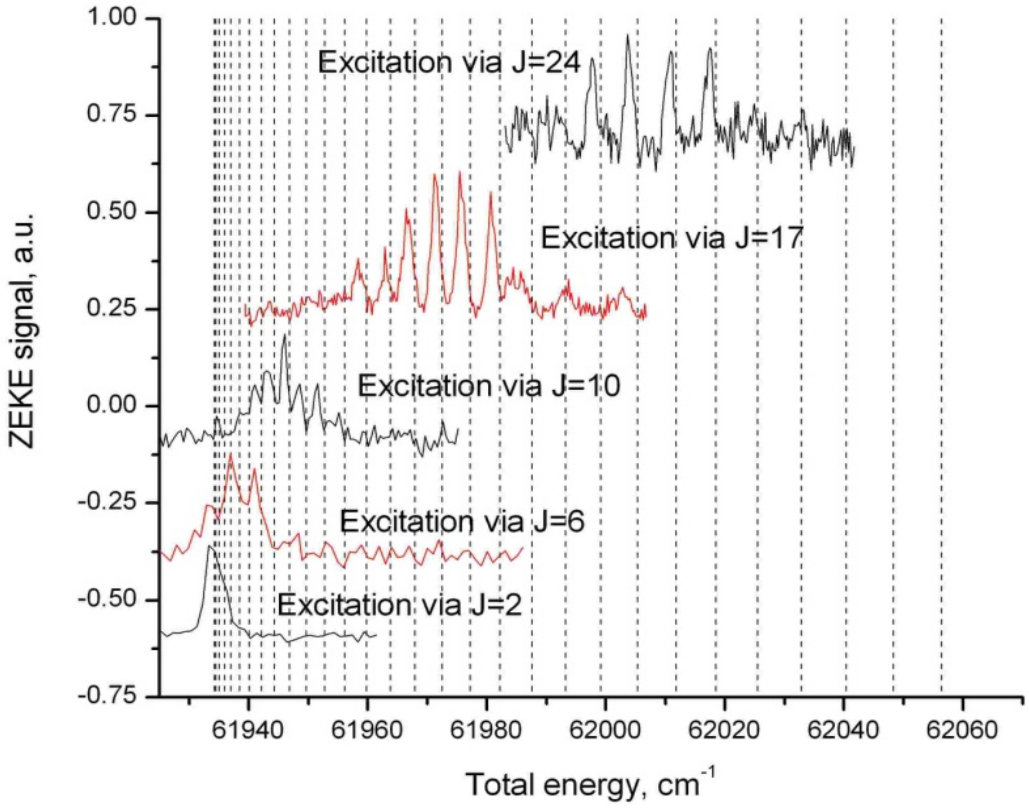

Figure V.4. Laser induced fluorescence spectrum of the $[31.68]^1\Pi$-$X^1\Sigma^+$ band. The downward-going trace is a simulation that includes the five most abundant isotopologues with an assumed rotational temperature of 7 K.

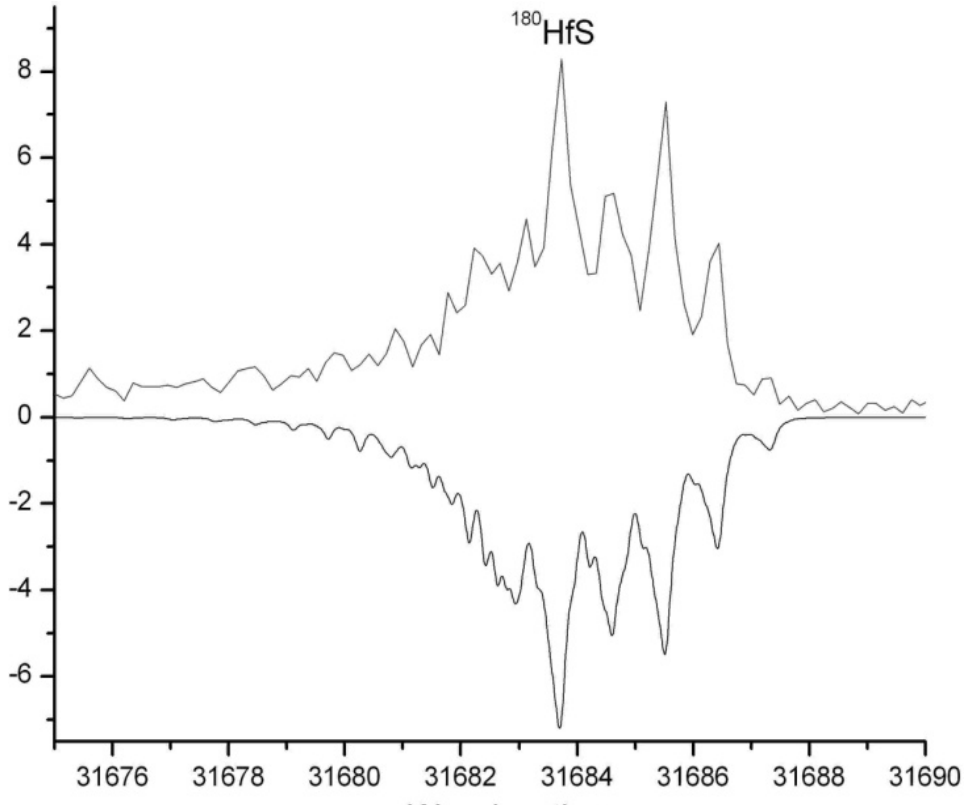

Figure V.5. PFI-ZEKE scans of the $^{180}HfS^{+}$ $X^{2}\Sigma^{+}$ state vibrational levels with v=0-6. These traces were recorded using initial excitation of the ^{180}HfS $[31.68]^{1}\Pi$-$X^{1}\Sigma^{+}$ band Q-branch feature at 31684.7 cm^{-1}.

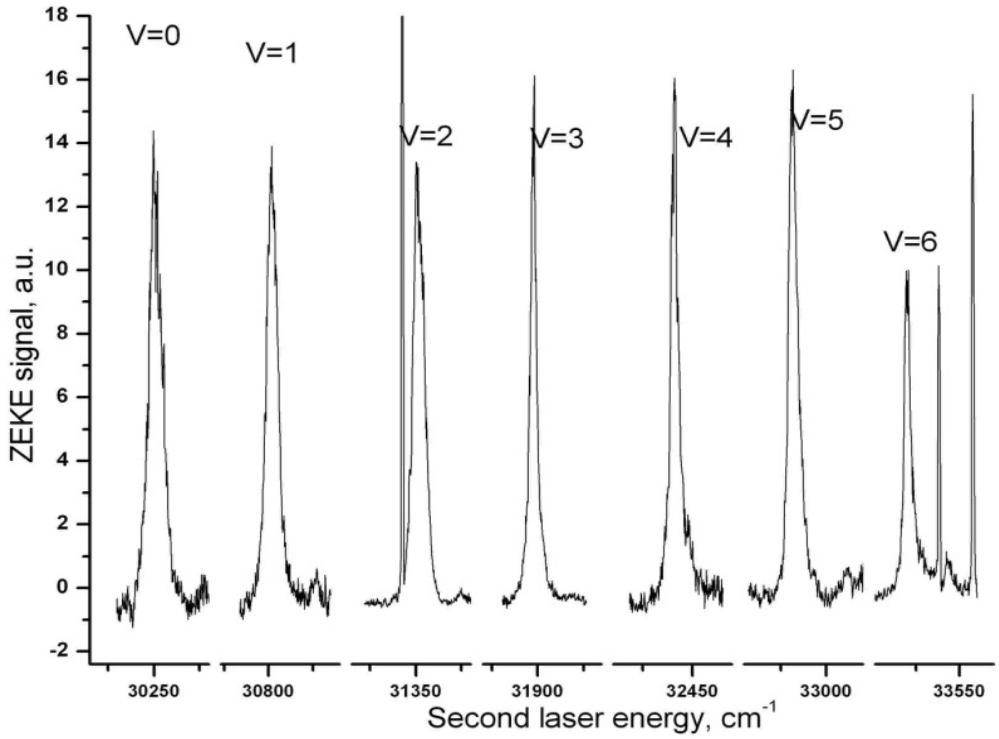

CHAPTER VI

SPECTROSCOPIC INVESTIGATIONS OF ThF, ThF^+ AND HfF^+

VI.1 INTRODUCTION

Theoretical calculations identify the HfF^+ and ThF^+ cations as promising candidates for experiments designed to measure the electric dipole moment of the electron (eEDM) [1-4] and search for time variation of the fine structure constant [5,6]. The ground state of the HfF^+ ion is predicted to be $Hf^{2+}(6s^2)F^-$ $X^1\Sigma^+$, and there is low-lying $^3\Delta$ state that is derived from the $Hf^{2+}(6s5d)F^-$ configuration [3,4]. ThF^+ is isoelectronic to HfF^+ and also predicted to possess a low-lying $^3\Delta$ and $^1\Sigma^+$ states. However, it is difficult to anticipate the ground state in ThF^+. Here the $^1\Sigma^+$ and $^3\Delta$ states may be so close in energy that the spin-orbit interaction could push the $^3\Delta_1$ state below $^1\Sigma^+$. It is the Ω=1 component of the $^3\Delta$ state in both HfF^+ and ThF^+ that is suitable for the eEDM measurement. The critical properties of $^3\Delta_1$ are the relatively high nuclear charge (Z=72 for Hf and Z=90 for Th), penetration of the s electron to the nucleus, and the polarizability of the d electron[3]. There is also a fortuitous near cancellation of the orbital and spin magnetic moments. Electronic structure calculations predict that an internal electric field of approximately 30 GV/cm can be achieved when $HfF^+(^3\Delta_1)$ is subjected to a modest external field [3,7]. In principle, this is sufficient to produce measurable level shifts due to the eEDM. ThF^+ offers even higher internal electric field, predicted to be around 90 GV/cm when the $^3\Delta_1$ state is polarized by a modest external electric field[8]. Thorium also has the advantage of having just one naturally occurring isotopomer.

With regard to measurements of the fine structure constant, Flambaum and Kozlov [5] argue that the sensitivity to temporal variations may be strongly enhanced in transitions between long-lived levels of different states that are close in energy. Measurements using HfF^+ were

proposed based on a near coincidence of energy levels of the $^3\Delta_1$ and $X^1\Sigma^+$ states [5,6]. High-level electronic structure calculations yield an energy difference between the $X^1\Sigma^+$ v=3 and $^3\Delta_1$ v=1 levels of 13 cm^{-1} [4,6]. This near proximity, combined with the narrow linewidths resulting from the electric dipole forbidden $^3\Delta_1$-$X^1\Sigma^+$ transition, appears to be favorable for determination of the fine structure constant. However, Skripnikov et al. [6] note that the calculated energy interval may be subject to considerable uncertainty.

Electronic spectra for HfF have been reported [9,10], but prior to our work no studies on HfF^+ have been published. As the designs for proposed experiments have relied on molecular constants derived solely from theoretical calculations it become important to probe the electronic structure of HfF^+ experimentally.

The data for the low-lying states of the ThF and ThF^+ species are of value for developing a better understanding of the bonding in elementary actinide compounds. Spectra recorded in the gas phase provide benchmark data against which high-level theoretical models can be rigorously evaluated[11-18]. In addition, ThF^+ is isoelectronic with ThO, a molecule for which there is a considerable body of gas phase spectroscopic data. Comparisons of the electronic structures of ThF^+ and ThO may be useful in assessing the applicability of ligand field theory (LFT) models[19] as a means for predicting the low-lying states of actinide containing molecules[15,16,20].

A mass spectrometric study by Lau et al.[21] provides the only published gas phase data available for ThF. Electron impact ionization measurements yielded an ionization energy (48400(2400) cm^{-1}). A bond dissociation energy of 54200(810) cm^{-1} was derived from temperature dependent species concentration measurements.

There are no previously published spectra for either ThF or ThF^+. However, Steimle and co-workers[22] have recorded a low-resolution laser induced fluorescence (LIF) spectrum showing multiple bands of ThF in the 17440-18512 cm^{-1} range. In this work we recorded rotationally resolved spectra for ThF with LIF and resonantly enhanced multi-photon ionization (REMPI) spectroscopy. Low-resolution dispersed fluorescence spectra were used to examine the lower

energy vibronic states. Spectra for ThF^+ were obtained using LIF and pulsed field ionization - zero kinetic energy (PFI-ZEKE) photoelectron spectroscopy. Kirk Peterson performed *ab initio* electronic structure calculations[23] that were used to facilitate the assignment of the low-energy electronic states – the results from these calculations will be also presented

VI.2 EXPERIMENTAL METHOD

As the spectrometer used in this study has been previously described in the Section II, only a brief description will be given here. ThF and HfF were produced using a laser ablation source. The 1064 nm output of a Nd/YAG laser was focused onto a Th or Hf metal sample shaped as disk or rod which was continuously rotated and translated to expose a fresh surface for each laser shot. The ablated material was entrained in a carrier gas which was a mixture of He + 0.1% SF_6. The carrier gas was emitted from a pulsed solenoid valve (Series 9, Parker-Hannifin, 0.8 mm diameter orifice). The solenoid valve and ablation laser were operated at 10 Hz. The source pressure and gas pulse duration were typically 20-25 PSI and 270 μs. The mixture undergoes a supersonic expansion which serves to cool the plasma generated from ablation. The expanding gas jet first passed under a set of optics for LIF collection, along an axis that was perpendicular to the both the spectroscopy laser and direction of the expansion. The laser beam crossed the expansion about 5 cm downstream from the nozzle orifice. The core of the gas jet then passed into a second differentially pumped chamber through the 5 mm orifice of a conical skimmer. The second chamber housed a time of flight-mass spectrometer (TOF-MS) that was used for recording resonantly enhanced multi-photon ionization (REMPI) and photo-ionization efficiency (PIE) spectra. This chamber was also equipped with a second set of grids and a micro-channel plate used for the recording of pulsed field ionization-zero electron kinetic energy (PFI-ZEKE) spectra.

LIF, REMPI and PFI-ZEKE spectra where obtained using an Nd/YAG pumped dye laser Coherent Scanmate Pro (SMP) and/or Continuum ND6000 dye laser. The LIF and REMPI spectra typically displayed a resolution of about 0.15 cm^{-1}. Higher resolution spectra were collected for selected bands by inserting an intracavity etalon into the SMP, which reduced the linewidth of the laser to about 0.05 cm^{-1}.

LIF and dispersed florescence spectra were collected by focusing the fluorescence onto the slits of a 0.25 m Ebert monochromator (Jarrell-Ash model 82-410, 1180 line/mm grating, 0.7 mm slit width). Scattered light was reduced by placing baffles on the entrance and exit windows as well as long-pass filters placed in front of the photomultiplier tube. Additionally, scattered light and LIF from other molecular species was reduced by the use of wavelength-selected fluorescence detection. For the two-color REMPI and PFI-ZEKE spectra, counter propagating laser beams were spatially overlapped in the ionization region of the TOF-MS. Digital delay generators were used to temporally overlap the two laser beams and to have them coincide with the arrival of ThF in the molecular beam. PFI-ZEKE and PIE spectra were collected using a two-color scheme, involving a resonant intermediate state. Here the first dye laser was tuned to a well resolved rotational-vibrational state of the neutral and the second was scanned to locate ionization thresholds.

For PFI-ZEKE measurements the extractor and repeller plates were held at -4.0 V to provide approximately field free conditions during photo-excitation. After a delay of about 1.5 μs, to allow the direct electrons to leave the ionization region, the voltage on the repeller plate was lowered to give a 0.71 V cm^{-1} electric field. This ionized the molecules trapped in high-*n* Rydberg states and accelerated the electrons to the detector. Resolution of the PFI-ZEKE spectra was between 1.25-1.50 cm^{-1}. In ThF experiments LIF and REMPI spectra were calibrated by observing Th atomic transitions. Accurate Th line positions were taken from the reference [24]. PFI-ZEKE spectra of ThF^+ and HfF^+ were calibrated by recording the I_2 B-X LIF spectrum using the fundamental output from the dye laser. Absolute calibrations were good to ± 0.1 cm^{-1}. The

monochromator was calibrated using emission lines from an Hg lamp. Band centers for the emission data were accurate to about 15 cm^{-1}

LIF and dispersed fluorescence spectra where recorded for ThF^+. ThF^+ was produced in the first vacuum chamber by ionizing ThF with a lightly focused ArF excimer laser (193 nm, 25 mJ/pulse). This was a single photon process as the photon energy was about 230 cm^{-1} above the ionization energy (see below). The excimer laser was counter propagated with the spectroscopy laser, perpendicular to both the molecular beam and light collection optics. The excimer laser was fired about 1.2-1.5 μs before the spectroscopy laser to allow the strong fluorescence caused by the excimer laser to decay.

VI.3 NOTATION

In the following the higher energy (>10000 cm^{-1}) excited states of ThF, HfF and ThF^+ are labeled using notation previously applied to lanthanide diatomic molecules[19]. When the 0-0 band origin for a given electronic transition has been established, the upper electronic state is labeled by $[T_0/10^3]$, where T_0 is the term energy given in wavenumbers. Here we include three digits for HfF bands and four digits for ThF and ThF^+ bands to obtain adequate specification. For bands where the upper state vibrational numbering is unknown, we use the labels $\{\nu_0/10^3\}$, where ν_0 is the vibronic band origin in wavenumbers.

VI.4 RESULTS

VI.4.1 SPECTROSCOPY OF HFF^+

Although electronic spectra for HfF have been reported[9,10], there were no data available for the energy range of interest (near 29000 cm^{-1}). Consequently, survey scans were made using resonantly enhanced two photon ionization spectroscopy to locate a suitable excited state of

neutral HfF. A prominent transition with a band origin at 28592.6 cm^{-1} was found. The rotational structure of this band is shown in Fig. VI.1, along with a simulated trace generated from fitted molecular constants. ^{180}HfF has a $X^2\Delta_{3/2}$ ground state with a rotational constant of B_0"=0.2837 cm^{-1} and electronic angular momentum coupling that is close to the Hund's case (a) limit (i.e., the spin-orbit coupling constant is far greater than the rotational constant) [9]. The rotational structure of Fig. VI.1 was assigned with these parameters held constant. The rotational linestrengths were consistent with an Ω=3/2 upper state (B_0'=0.255(4) cm^{-1}) that was close to the Hund's case (a) or case (c) limit. This state is designated as [28.6]3/2 in the following.

An approximate value for the IE of HfF (to within ±40 cm^{-1}) was obtained using initial excitation of [28.6]3/2, with the second laser scanned over the energy range where the threshold was expected. Mass selected detection of the HfF^+ ion was used at this stage. A more accurate value for the IE, and the energy levels of HfF^+ were then determined using the technique of pulsed field ionization - zero kinetic energy (PFI-ZEKE) photoelectron spectroscopy [14]. This scheme discriminates against autoionizing resonances and, due to the reliance on electron detection, can employ weak electric fields (≈0.1 V cm^{-1}) for the ionization step. Fig. VI.2 shows a section of a low resolution PFI-ZEKE spectrum for HfF^+. This trace is a composite assembled from multiple shorter range scans. Several laser dyes were needed to cover this range, and the intensities have not been corrected for the variation of the laser power with wavelength.

Vibronic assignment of the spectrum was straightforward. The progression of vibrational levels belonging to the electronic ground state was immediately apparent. Data were obtained for the levels *v*=0-6. Progressions originating from three electronically excited states were also observed. Levels *v*=0-3 were observed for the first two, and the v=0 and 1 levels were detected for the third.

Low resolution scans were recorded with excitation of the R-branch band head of the [28.6]3/2-X transition, such that multiple rotational levels of the intermediate state were excited.

Rotationally resolved data for the ion were obtained using initial excitation of individual J levels using the well-resolved P-branch lines (c.f., Fig. VI.1). As an example, Fig. VI.3 shows spectra for the $X^1\Box^+$ v=0 level, recorded using excitation of intermediate rotational levels with J= 2.5-10.5. The spectra show a tendency towards the conservation of the rotational angular momentum on ionization, but levels with lower rotational angular momentum appear in the spectra due to rotational channel coupling [25].

The rotational line positions were fitted to the expression,

$$\nu = T_{e,v} + B_{e,v}J(J+1) \qquad (1)$$

where e and v denote the electronic and vibrational levels of the ion. The ionization energy determined from the data for $X^1\Sigma^+$ v=0 is 59464(2) cm^{-1} for J=0 of the ion, relative to HfF $X\,^2\Delta_{3/2}$ v=0, J=3/2. The term energies ($T_{e,v}$) from fitting to Eq. 1 are listed in Table VI.1, where they are specified relative to the ground state zero-point energy. Vibrational constants were derived from these results by fitting to the anharmonic oscillator expression

$$T_{e,v} = T_{e,0} + \omega_e v - \omega_e x_e v(v+1) \qquad (2)$$

Rotational and vibrational constants for HfF^+ are collected in Table VI.2.

VI.4.2 REMPI AND LIF SPECTRA OF NEUTRAL THF

Figure VI.4 shows a low resolution REMPI spectrum recorded using detection of ThF^+ (mass 251 amu). The spectral range 19500-21300 cm^{-1} was examined because preliminary theoretical calculations suggested this would be approximately 40-50% of the IE of ThF, and because atomic Th displays strong *s-p* transitions above 20,000 cm^{-1}. The ionization laser was set to a wavelength such that the 1 + 1' photon energy exceeded the ionization energy (IE) of ThO[16] by at least 2500 cm^{-1}. This was thought to be well above the IE of not only ThF, but also other previously unobserved molecular species that could be produced in the laser ablation source. In addition to ThF, the other species observed in the mass spectrometer were Th^+, ThO^+, ThF_2^+, and $ThOF^+$. Despite the presence of SF_6 in the carrier gas, ThS^+ was not observed. The bands labeled

in Fig. VI.4 ({19.92}, {20.44}, {20.95}) were rotationally resolved using LIF. These transitions were intense, free of other overlapping ThF bands, and relatively straightforward to analyze (ie. free of local perturbations). Well-resolved P-branches were observed, which allowed for the selection of a single ro-vibronic level in the first step of two-color PIE and PFI-ZEKE measurements. Figure VI.5 shows an LIF spectrum of the {20.95} band taken with the intra-cavity etalon present in the dye laser. The lower trace is a simulated spectrum generated using the program PGOPHER.[26] The {19.92} and {20.44} bands displayed similar structure to the {20.95} band. As can be seen in Fig. VI.5, the lowest J values for the P- and R-branch lines were 2.5 and 1.5 respectively, indicating that Ω=1.5 for both the lower and upper electronic states. Spectroscopic constants were derived using the fitting routine in PGPOPHER.[26] All three transitions where simultaneously fit assuming a common lower state. The Hund's coupling case (a) or (c) limit (where the spin-orbit coupling constant is much greater than the rotational constant) was assumed for both the upper and lower electronic states. Only the band origin, lower and upper rotational constants were allowed to vary. The rotational temperature used for these fits was 25K. Including additional parameters in the fit, such as the centrifugal distortion constants did not improve the quality of the fit and the standard deviations for these parameters were large. Molecular constants for these bands are summarized in Table VI.3.

Time-resolved fluorescence decay curves were recorded for the {19.92}, {20.44} and {20.95} states. Single exponential decays were observed, with lifetimes of 351(5), 396(5), and 374(5) ns, respectively.

Figure VI.6 shows dispersed fluorescence spectra obtained by pumping the R-branch band heads of the {20.44} and {20.95} transitions. Emission back to the ground electronic state was observed for both transitions, while an additional transition to a low-lying excited electronic state was observed only from the {20.44} state. The $\Delta G_{1/2}$ value for the ground electronic state was determined to be 605(15) cm^{-1}. The first electronically excited state was found at T_0=2575(15) cm^{-1} above the ground state, with a vibrational interval of $\Delta G_{1/2}$=570(15) cm^{-1}. As

the standard deviations for these intervals almost overlap, it was not established that the difference between the intervals is meaningful. To a first approximation it is expected that the vibrational intervals for the two spin-orbit components would be closely similar.

VI.4.3 MEASUREMENT OF THE THF IONIZATION ENERGY AND THE SPECTROSCOPY OF THF^+

An approximate value for the ionization energy (IE) of ThF was determined by recording PIE curves. Measurements were performed with the first laser set to excite the R-branch band heads of the {19.95}, {20.44} or {20.95} transitions. The wavelength of the second laser was scanned and the signal for ThF^+ in the mass spectrometer was monitored. In the analyses of these data, the effect of the electric field in the TOF-MS, which reduces the measured IE relative to the field free value by $\Delta E(cm^{-1}) = 6\sqrt{F(V/cm)}$, was taken into account. The IE obtained using this method was 51550(40) cm^{-1}. A further correction was needed to compensate for the fact that a range of rotational levels were excited. The R-branch band head contains the lines R(10.5) to R(14.5), which reduces the IE by 25-45 cm^{-1} (relative to J=1.5). An IE value of 51585(50) cm^{-1} was obtained by including this correction.

Low-resolution PFI-ZEKE spectra were also recorded using excitation at the {20.44}-X(Ω=1.5) R-branch band-head. Figure VI.7 shows a representative survey scan. The relative intensities of the transitions shown by this spectrum, while not corrected for variations in the laser power, are qualitatively correct. The origin band was the most intense transition in the spectrum. Generally the signal-to-noise (S/N) ratio of the transitions decreased with increasing energy above the origin band. Because of this, rotationally resolved PFI-ZEKE spectra of the ion could only be collected for 10 of the first 11 transitions shown in Fig. VI.7. The remaining transitions had S/N ratios that were too small for the recording of rotationally resolved spectra.

The transitions of Fig. VI.7 were examined using intermediate excitation of individual ro-vibronic levels of the neutral molecule; typically a fully resolved P-branch line. An example of a

rotationally resolved PFI-ZEKE spectrum for the ν=0 band of the ground electronic state of ThF^+ is shown in Fig. VI.8. This trace was taken using initial excitation of the {20.9}-X(Ω=1.5) P(7.5) transition. While the PFI-ZEKE spectra showed some tendency towards conservation of the rotational angular momentum upon ionization, levels with lower rotational angular momentum than that of the intermediate ro-vibronic state appeared due to rotational channel coupling.[25] The ionization energy determined from the lowest energy feature (51581(3) cm^{-1}) corresponds to the energy difference between the X ν=0 J=0 level of the ion and the X(Ω=1.5) ν=0 J=1.5 level of the neutral, under the assumption that the ground electronic state of the ion is $X^1\Sigma^+$.

Vibronic assignment of the survey scans (Fig. VI.7) was straightforward and vibronic progressions belonging to the electronic ground state, and four excited electronic states, were identified. Rotationally resolved spectra where obtained for the ν=0-3 levels for the ground electronic state and the ν=0-2 levels for the first two electronically excited states (labeled A and B). The *v*=0 and 1 levels of the two highest energy electronic states (labeled C and D) were observed, but rotationally resolved spectra for these weak transitions could not be obtained

The expression (1) was fitted to the rotational line positions, where *e* and ν denote the electronic and vibrational levels of the ion. Ionization energies of individual J states were determined using the blue edge of each feature. The blue edge was determined by adding the FWHM of each peak to its line center. Positions for the bands of states C and D determined from the band centers of the PFI-ZEKE survey spectrum (Fig. VI.7). These bands were rather broad (15 cm^{-1} FWHM) and the error bars for the term energies for these states are estimated to be about ±15 cm^{-1}.

Vibrational constants were derived by fitting the anharmonic oscillator expression (2) to the band origins. Vibrational frequencies and rotational constants for the first three electronic states are collected in Table VI.4.

Attempts were made to resolve the rotational structures down to the lowest J value in the *v*=0 band for each electronic state. Unfortunately, due to limited resolution of the low-J lines, this

was only possible for the third electronically exited state (system B in Fig. VI.7), for which the lowest value of J=2 establishes Ω=2. The resolution of the PFI-ZEKE study was not high enough (1.25-1.50 cm^{-1}) to unambiguously assign the lowest J value for the ground or first electronically excited state, where the lowest rotational levels are either J=0 or 1. PFI-ZEKE spectra of the *v*=0 band of the ground electronic state were taken using a lower pulsed field (0.178 V/cm) to improve the resolution. The results suggest that a J=0 level is present, but the resolution was still not sufficient to make this assignment certain.

Photo-ionization of ThF at 193 nm was used for studies of ThF^+ that relied on LIF detection. Figure VI.9 shows a low resolution survey scan taken in the 18000-21200 cm^{-1} range. Labeled peaks are LIF from ThF^+, while the remaining peaks are from neutral ThF, ThO or atomic Th/Th^+. Spectral features were assigned to ThF^+ based on three types of observation. First, spectra taken with and without the 193 nm laser operating were compared. Transitions originating from ThF^+ and atomic Th^+ were absent when the 193 nm excimer laser light was not present. Next, dispersed fluorescence spectra were collected from transitions suspected of originating from ThF^+. In each case emission was observed to multiple vibrational levels of the ground electronic state. The vibrational frequency determined from the emission spectra agreed well with that determined from the PFI-ZEKE spectra. Note that the vibrational frequencies of other Th containing species such as ThO and ThO^+ are much larger[16,17] than that for ThF^+. Lastly, rotational constants determined by fitting the rotational resolved bands (see below) agreed well with rotational constants determined from the PFI-ZEKE spectra. LIF from neutral ThF could also be differentiated from that of ThF^+ by tuning the monochromator to the □=1 feature in the emission spectrum of ThF^+, as the vibrational frequencies of the neutral and ion differ by about 50 cm^{-1}.

Figure VI.10 shows the LIF spectrum of the band at 21062 cm^{-1} taken with the intra-cavity etalon in the dye laser. The lower trace is a simulated spectrum generated using PGOPHER[26] and the upper trace is the experimental spectrum. The rotational structures of the

other observed bands were very similar to that shown in Fig. VI.10. The 21062 cm^{-1} band was the only transition examined using the etalon, as the lower resolution spectra indicated that this band had the least interference from weaker overlapping transtions. The rotational linestrengths, and in particular the relative intensities of the Q-branch lines, indicated that there is a change of $\Delta\Omega = \pm 1$ between the lower and upper electronic states. Unfortunately, it was not possible to unambiguously assign the Ω values of the lower or upper states using the LIF spectra. The lowest Q and R branch lines that could be positively identified were Q(2) and R(1). It is difficult to rule out the presence of a Q(1) or R(0) line because the spectrum has a relatively high rotational temperature (85 K) and the intensities of the R(0) and Q(1) lines at this temperature are predicted to be low; the Q(1) line also suffers from the problem that it is difficult to resolve it from the Q(2) line. Close inspection of Fig. VI.10 reveals the presence of a weak feature that could be the R(0) line.

Molecular constants were derived using the fitting routine in PGPOPHER.[26] Fitting each band in isolation yielded results that were consistent with the assignment of the transitions to a common lower level. The line-strengths were well represented by assuming a $^1\Pi_1$-$^1\Sigma^+$ transition type, but the comparison with simulations based on the assumption of a $^3\Pi_0$-$^3\Delta_1$ transition type indicated that the intensity distribution data were not of sufficient quality to differentiate between these possibilities. In modeling the triplet transitions it was assumed that the limiting form of Hund's case (a) or (c) for angular momentum coupling was appropriate for both the upper and lower states.

To obtain a consistent set of molecule constants, all five transitions were simultaneously fit assuming the $^1\Pi_1$-$^1\Sigma^+$ transitions type. Only the band origins and rotational constants were allowed to vary, with the rotational temperature fixed at 85 K. Fits using additional parameters (such as the centrifugal distortion constant) did not significantly increase the quality of the fit, and standard deviations for these parameters were large. The optimized molecular constants are presented in Table VI.5. Also listed are the positions of the R-band branch heads. This

information is provided because the band origins are slightly dependent on the choice of electronic transition type.

Four of the ThF^+ bands indicated in Fig. VI.9 have been assigned to a vibrational progression to a specific electronic state (labeled as [19.36] in the following). This assignment was based on the excellent fit of Eq. 2 to the band origins, and the intensity patterns observed in dispersed fluorescence spectra (described below). The band at 19361 cm^{-1} was identified as the electronic origin (0-0) as there were no spectral features at lower energy that could fit with the progression. In addition, the dispersed fluorescence spectrum from this level displayed a typical v=0 Franck-Condon intensity pattern. The upper state vibrational constants obtained from this progression were ω_e=572.8(10) cm^1 and $\omega_e x_e$=1.43(25) cm^{-1}.

The dispersed fluorescence spectra all displayed emission to the ground electronic state of ThF^+ with no other electronic states observed. Figure VI.11 shows a typical example. This trace was recorded for excitation of the [19.36] *v*=3 level. The intensity patterns of these spectra were compared with Franck-Condon factors that were generated using Morse potential energy curves. The potential function parameters were determined from the vibrational and rotational constants. The observed intensity patterns were qualitatively reproduced by the Franck-Condon calculations, with a level of agreement that was sufficient to confirm the upper state vibrational numbering.

The fourth band of ThF^+, observed at 20718 cm^{-1}, involves a different electronically excited state. The dispersed fluorescence spectrum for this upper level indicates that it is vibrationally excited, but as other vibrational levels of this state were not identified, the vibrational quantum number could not be determined.

VI.5 ELECTRONIC STRUCTURE CALCULATIONS OF THF AND THF^+

Low-energy electronic states of ThF and ThF^+ were investigated using multi-reference configuration interaction (MRCI) and coupled-cluster calculations. These calculations were performed by our collaborator Kirk Peterson and fully described in ref. 23. Only a brief description will be given here. The calculation were carried out using the MOLPRO 2010 suite of programs[27]. The basis set used for Th consisted of a 60 electron effective core potential with the atomic natural orbital basis for the valence electrons (ECP60MWB_ANO).[28] The augmented correlation consistent valence triple zeta basis set (aug-cc-pVTZ) was used for the F atom.[29,30]

The MRCI calculations were applied to study the ThF molecule. The calculations yielded $\Delta G_{1/2}$ vibrational intervals for the $^2\Delta_{3/2}$ and $^2\Delta_{5/2}$ states of 573.8 and 573.9 cm^{-1}. These results are in good agreement with the value measured for the $^2\Delta_{5/2}$ component, and compatible with the interval for the $^2\Delta_{3/2}$ state, given the experimental error range. The calculated spin-orbit interval was 1939 cm^{-1}, which is approximately 640 cm^{-1} lower than the observed value. The predicted ground state zero-point rotational constant, B_0=0.2264 cm^{-1}, was lower than the measured value of 0.237(5) cm^{-1}, indicating that the calculations had slightly underestimated the equilibrium bond length. The first excited states above the components of $^2\Delta$ were $^2\Pi_{1/2}$ and $^2\Pi_{3/2}$ that arise from the $Th^+(7s^2 6d_\pi)F^-$ configuration. The term energies predicted for these states (T_e) were 4253 and 6134 cm^{-1}, respectively.

Coupled-cluster methods were used to examine the $^1\Sigma^+$ and $^3\Delta$ states of ThF^+. Spin-free calculations were carried out using CCSD(T) (perturbative triples),[31-33] CCSDT (full triples),[34-37] and CCSDT(Q) (perturbative quadruples).[34,38-40] The latter calculations utilized a slightly smaller [5s5p4d3f2g] contraction of the ECP60MWB_ANO basis set on Th. A quadruples correction, obtained from CCSDT and CCSDT(Q) calculations with this smaller basis set, was then added to the CCSDT results as an approximation to CCSDT(Q) with the full basis. Energy shifts due to spin-obit coupling, calculated at the double-group MRCI level[41] using the COLUMBUS

program,[42] were calculated at each internuclear distance considered and added to the coupled-cluster energies.

A summary of the results from these calculations is presented in Table VI.6. Compared to CCSD(T), full inclusion of triple excitations via CCSDT has a significant effect on the $^1\Sigma^+$ - $^3\Delta_1$ energy interval and the vibrational constants. Details of particular significance are that the $^1\Sigma^+$ - $^3\Delta_1$ spacing decreases and the differences between the vibrational constants also decrease when the higher level correlation method is employed. Approximate inclusion of connected quadruple excitations via CCSDT(Q) calculations further decreases the singlet-triplet energy gap with the $^1\Sigma^+$ state becoming slightly lower in energy than the $^3\Delta_1$. It should also be noted that without the inclusion of SO coupling effects, the singlet state is lower in energy than the triplet with all three methods, reaching just over 1000 cm^{-1} at the CCSDT(Q) level of theory. In all cases the calculated equilibrium bond distances are consistent with the average value of R_0=1.98(2) Å determined from the measured B_0 rotational constants.

In order to assess the accuracy of the pseudopotential approximation in the present work, all-electron 2nd-order Douglas-Kroll-Hess calculations[43,44] were also carried out at the CCSD(T) level of theory using the aug-cc-pV*n*Z-DK (*n*=T, Q) basis on F and the ANO-RCC basis set of Roos et al.[45] on Th. When paired with the aug-cc-pVTZ-DK set, the *h*-type functions of the ANO-RCC basis set were omitted. These latter calculations, which should be comparable to the pseudopotential work, yielded bond lengths about 0.005 Å longer, harmonic frequencies within 2 cm^{-1}, and a lowering of the triplet state relative to the singlet by about 70 cm^{-1}. Use of the full ANO-RCC basis set with aug-cc-pVQZ-DK on F resulted in a further shortening of the bond lengths by 0.002 – 0.003 Å, an increase in ω_e by 2-4 cm^{-1}, and a further lowering of the triplet relative to the singlet by 236 cm^{-1}. Taking these latter results into account, the best prediction of the present calculations still places the $^3\Delta_1$ state lower than the $^1\Sigma^+$ by about 240 cm^{-1}.

VI.6 DISCUSSION

VI.6.1 HFF^+ SPECTRAL ASSIGNMENT

The rotational structures for the two highest energy electronic states of HfF^+ could be resolved down to the lowest value of J for each band, from which it could be seen that the Ω values were 2 and 3. This observation is consistent with the electronically excited states being the Ω=1, 2, and 3 components of a $^3\Delta$ state, as predicted by the ab initio calculations[4]. Additional support for this assignment is provided by the observation that the vibrational constants for the excited states are very similar, and significantly smaller than that of the ground state. The calculated ground state constant (790 cm^{-1})[4] is in excellent agreement with the measured value, while the calculated constants for the $^3\Delta$ state were underestimated by approximately 11 cm^{-1}. Fig. VI.12 shows the energy levels characterized in this study. Data for the v=4 level of $^3\Delta_1$ are not reported because this feature was obscured by an intense one-color, two photon resonance.

For direct comparison with theoretical calculations, the term energies for the minima of the potential energy curves have been calculated from the measured constants. These values are collected in Table VI.7, where the energy is referenced to the minimum of the ground electronic state. The spin-orbit intervals from both the measurements and calculations are in respectable agreement, and are indicative of coupling that tends towards Hund's case (a). Of particular interest, the term energy for $^3\Delta_1$ is appreciably lower than the calculated value. From the perspective of eEDM experiments this is good news as it leads to a longer excited state lifetime. Petrov et al. [4] predicted a v'=0 lifetime 0.389 s. Assuming that their transition moment calculations are reasonably accurate, the effect of shifting the transition energy on the radiative lifetime can be estimated using $\tau = (T_0(calc)/T_0(obs))^3 \tau(calc)$. This yields a lifetime of 1.7 s.

The experimental value for $T_0(^3\Delta_1)$ is less favorable for the proposed measurements of the fine structure constant [5,6]. As can be seen in Fig. VI.12, none of the observed levels of $^3\Delta_1$ are particularly close to those of $X^1\Sigma^+$. The smallest interval is a gap of 116.5 cm^{-1} between the v'=3 and v''=4 levels.

VI.6.2 THF AND THF^+ SPECTRAL ASSIGNMENT

The Ω=3/2 ground state of ThF is consistent with the expected $Th^+(7s^2\ 6d_\delta)F^-\ X^2\Delta_{3/2}$ configuration. Dispersed fluorescence spectra revealed an excited state at 2575(15) cm^{-1}. This is most probably the upper spin-orbit component, $X^2\Delta_{5/2}$. The theoretical calculations described above yielded a spin-orbit interval of 1939 cm^{-1}, while the next electronically excited doublet state ($^2\Pi_{1/2}$) was predicted to be at 4253 cm^{-1}. Hence, assignment of the first excited state as $X^2\Delta_{5/2}$ seems reasonable, and implies that the theoretical calculations have underestimated the observed spin-orbit interaction energy by about 640 cm^{-1}. In this context it is of interest to note that the $X^2\Delta_{5/2}$ state of HfF was tentatively identified by Adam et al.[9], and the term energy for this state indicated a spin-orbit interaction energy of 2850 cm^{-1}.

Electronic transitions of ThF in the 19500-21300 cm^{-1} range were investigated. Owing to the high density of excited states expected in this region, we can only speculate on the nature of the excited states that were accessed. Given the relatively strong LIF signals observed, and the fluorescence decay lifetimes (350-390 ns), we conclude that the oscillator strengths for these transitions were quite large (≈0.16). As the changes in bond length on excitation were modest, it is most likely that the transitions listed in Table VI.3 are formally metal-centered $7p\leftarrow 6d$ and/or $7p\leftarrow 7s$ promotions.

Due to the potential suitability of ThF^+ for eEDM measurements, it is of particular interest to establish the term energy of the $^3\Delta_1$ state. While the spin-free calculations reported here yielded a $^1\Sigma^+$ ground state, inclusion of spin-orbit coupling pushed the $^3\Delta_1$ below the $^1\Sigma^+$. Increasing the quality of the correlation treatment from CCSD(T) to CCSDT(Q) reduced the energy gap, reversing the order, but larger basis sets and DK corrections reversed the order again. While of respectable quality, the ab initio calculations reported here were still not sufficiently accurate for a definitive identification of the ground state.

The PFI-ZEKE spectrum shows an electronically excited state just 315.0(5) cm^{-1} above the ground state. These lowest energy states are no doubt $^1\Sigma^+$ and $^3\Delta_1$, but the spectral resolution

achieved in the present measurements was not good enough to determine Ω values for states with Ω<2. In the analogous example of HfF^+ the vibrational constants were helpful in establishing that the ground state is $^1\Sigma^+$. The vibrational constant for $Hf^{2+}(6s^2)F^-$ $^1\Sigma^+$ (791 cm^{-1}) was clearly greater than that of $Hf^{2+}(6s5d)F^-$ $^3\Delta$ (761 cm^{-1}). This difference can be attributed to the fact that the 6*s* orbital is more polarizable than the 5*d*, allowing a reduction of the repulsive interaction between the metal-centered valence electrons and the F^- ligand. Unfortunately, this idealized ionic model does not appear to describe the low-lying states of ThF^+, which all have very similar vibrational constants (c.f., Table VI.5). As described above, our highest level *ab initio* calculations also find very similar vibrational constants for the $^1\Sigma^+$ and $^3\Delta$ states.

While the experimental data do not yield a definitive answer, there are two observations that favor assignment of the ground state as $^1\Sigma^+$. The first is provided by the approximate spectral intensity data. The lowest energy band in the PFI-ZEKE spectrum is far more intense than any other feature. This suggests that it arises from a unique configuration. The PFI-ZEKE spectrum for HfF^+ exhibits transitions to the $^3\Delta_1$, $^3\Delta_2$, and $^3\Delta_3$ states that have similar intensities (c.f., Fig. VI.2). If the ground state of ThF^+ is $^3\Delta_1$, it is difficult to explain why the intensities are so much weaker for the $^3\Delta_2$, and $^3\Delta_3$ states.

Though less compelling, an analysis of the spin-orbit intervals also favors the $^1\Sigma^+$ ground state assignment. In the limit that the Th 6*d* orbital retains its atomic character, the intervals between the $^2\Delta_{5/2}$-$^2\Delta_{3/2}$ states of ThF, and the $^2\Delta_3$-$^2\Delta_1$ states of ThF^+ will be approximately twice the atomic spin-orbit interaction constant. Assignment of the ThF^+ ground state to $^1\Sigma^+$ or $^3\Delta_1$ gives intervals of 2835 and 3150 cm^{-1}, respectively. Both are greater than the spin-orbit interval for ThF (2575 cm^{-1}), so the discrepancy is least assuming a $^1\Sigma^+$ ground state. For comparison, the corresponding spin-orbit intervals for HfF and HfF^+ are 2850[9] and 2959 cm^{-1}.

The observation that the term energy for $^3\Delta_1$ is no more than 315 cm^{-1} is very favorable for eEDM investigations. Assuming that $^3\Delta_1$ is the first excited state, the radiative transition back to the ground state will be very slow, giving rise to sharply defined energy levels. Once

populated, the long lifetime of the state will also facilitate a variety of measurement strategies. We cannot exclude the possibility that $^3\Delta_1$ is the ground state, which would be even more favorable for eEDM measurments.

VI.6.3 IONIZATION AND BOND DISSOCIATION ENERGIES

The IE measured using PFI-ZEKE (51581(3) cm^{-1})) for ThF is slightly higher than the previous gas phase value determined using an electron impact mass spectrometric method (48400(2400) cm^{-1}).[21] This is likely to due to ionization from thermally excited states in the electron impact study, as ThF was produced in the gas phase using a heated effusion beam source (note that the difference is close to the spin-orbit interval for ThF). Large differences between IE's measured using electron impact and PFI-ZEKE have also been observed in other metal containing dimers such as HfO[46,47], ThO[16,17] and UO[15,18].

The difference between the IE's of atomic and fluoride species provides a direct experimental measurement of the difference between the bond energies of MhF and MhF^+, from the thermodynamic relationship:

$$IE\ (MF) - IE\ (M) = D_0\ (MF) - D_0^+\ (MF^+), \qquad (3)$$

where M is Hf or Th. The difference between the ionization energies for HfF (IE = 59464 cm^{-1}) and Hf (IE = 55049 cm^{-1}) shows that the bond energy of HfF^+ is 4414 cm^{-1} weaker than that of the neutral molecule. Using the values for the IE of atomic Th (50867 cm^{-1})[48] and ThF (51851(3) cm^{-1}) in Eq. 3 shows that the bond energy of the neutral exceeds that of the ion by 984 cm^{-1}. Using the bond dissociation value from Lau et al.[21] for ThF (D_0=54200(810) eV) gives a bond dissociation energy for the ion of D_0^+ = 53230(810) eV.

Despite the fact that the bond energy decrees upon ionization, the vibrational frequencies of both ions are larger and the bond lengths are shorter than in the neutral HfF and ThF. This trend was also observed in the ThO[16] and HfO[46,47].

REFERENCES

(1) Meyer, E. R.; Bohn, J. L.; Deskevich, M. P. *Los Alamos Natl. Lab., Prepr. Arch., Phys.* **2006**, 1-25, arXiv:physics/0604205.

(2) Petrov, A. N.; Mosyagin, N. S.; Isaev, T. A.; Titov, A. V. *Los Alamos Natl. Lab., Prepr. Arch., Phys.* **2006**, 1-3, arXiv:physics/0611254.

(3) Leanhardt, A. E.; Bohn, J. L.; Loh, H.; Maletinsky, P.; Meyer, E. R.; Sinclair, L. C.; Stutz, R. P.; Cornell, E. A. *arXiv.org, e-Print Arch., Phys.* **2010**, 1-36, arXiv:1008 2997v1 [physics atom-ph].

(4) Petrov, A. N.; Mosyagin, N. S.; Titov, A. V. *Phys. Rev. A At., Mol., Opt. Phys.* **2009**, *79*, 012505/1-012505/7.

(5) Flambaum, V. V.; Kozlov, M. G. *Phys. Rev. Lett.* **2007**, *99*, 150801/1-150801/4.

(6) Skripnikov, L. V.; Mosyagin, N. S.; Petrov, A. N.; Titov, A. V. *JETP Lett.* **2009**, *88*, 578-581.

(7) Petrov, A. N.; Mosyagin, N. S.; Isaev, T. A.; Titov, A. V. *Phys. Rev. A At., Mol., Opt. Phys.* **2007**, *76*, 030501/1-030501/4.

(8) Meyer, E. R.; Bohn, J. L. *Phys. Rev. A At., Mol., Opt. Phys.* **2008**, *78*, 010502/1-010502/4.

(9) Adam, A. G.; Hopkins, W. S.; Tokaryk, D. W. *J. Mol. Spectrosc.* **2004**, *225*, 1-7.

(10) Moskvitina, E. N.; Kuzyakov, Y. Y. *Spectrosc. Lett.* **1999**, *32*, 719-728.

(11) Heaven, M. C.; Gibson, J. K.; Marcalo, J. In *The chemistry of the actinide and transactinide elements*; Morss, L. R., Edelstein, N. M., Fuger, J., Eds.; Springer: 2010; Vol. 6, p 4079-4156.

(12) Wang, F.; Le, A.; Steimle, T. C.; Heaven, M. C. *J. Chem. Phys.* **2011**, *134*, 031102/1-031102/3.

(13) Heaven, M. C.; Goncharov, V.; Steimle, T. C.; Ma, T.; Linton, C. *J. Chem. Phys.* **2006**, *125*, 204314/1-204314/11.

(14) Heaven, M. C. *Phys. Chem. Chem. Phys.* **2006**, *8*, 4497-4509.

(15) Goncharov, V.; Kaledin, L. A.; Heaven, M. C. *J. Chem. Phys.* **2006**, *125*, 133202/1-133202/8.

(16) Goncharov, V.; Heaven, M. C. *J. Chem. Phys.* **2006**, *124*, 064312/1-064312/7.

(17) Goncharov, V.; Han, J.; Kaledin, L. A.; Heaven, M. C. *J. Chem. Phys.* **2005**, *122*, 204311/1-204311/6.

(18) Han, J.; Kaledin, L. A.; Goncharov, V.; Komissarov, A. V.; Heaven, M. C. *J. Am. Chem. Soc.* **2003**, *125*, 7176-7177.

(19) Field, R. W. *Ber. Bunsenges. Phys. Chem.* **1982**, *86*, 771-9.

(20) Kaledin, L. A.; McCord, J. E.; Heaven, M. C. *J. Mol. Spec.* **1994**, *164*, 27-65.

(21) Lau, K. H.; Brittain, R. D.; Hildenbrand, D. L. *J. Chem. Phys.* **1989**, *90*, 1158-64.

(22) Steimle, T. C., LIF Spectrum of ThF.

(23) Barker, B. J.; Antonov, I. O.; Heaven, M. C.; Peterson, K. A. *J. Chem. Phys.*, *136*, 9.

(24) Giacchetti, A.; Stanley, R. W.; Zalubas, R. *J. Opt. Soc. Amer.* **1970**, *60*, 474-89.

(25) Linton, C.; Simard, B.; Loock, H. P.; Wallin, S.; Rothschopf, G. K.; Gunion, R. F.; Morse, M. D.; Armentrout, P. B. *J. Chem. Phys.* **1999**, *111*, 5017-5026.

(26) Western, C. M.; University of Bristol: 2007.

(27) Werner, H.-J.

(28) Cao, X.; Dolg, M.; Stoll, H. *J. Chem. Phys.* **2003**, *118*, 487.

(29) Dunning, T. H., Jr. *J. Chem. Phys.* **1989**, *90*, 1007-1023.

(30) Kendall, R. A.; Dunning, T. H., Jr.; Harrison, R. J. *J. Chem. Phys.* **1992**, *96*, 6796-6806.

(31) Knowles, P. J.; Hampel, C.; Werner, H.-J. *J. Chem. Phys.* **1993**, *99*, 5219-5227.

(32) Scuseria, G. E. *Chem. Phys. Lett.* **1991**, *176*, 27-35.

(33) Watts, J. D.; Gauss, J.; Bartlett, R. J. *J. Chem. Phys.* **1993**, *98*, 8718-8733.

(34) Kállay, M.; Surján, P. R. *J. Chem. Phys.* **2001**, *115*, 2945.

(35) Noga, J.; Bartlett, R. J. *J. Chem. Phys.* **1987**, *86*, 7041.

(36) Scuseria, G. E.; Schaefer, H. F. *Chem. Phys. Lett.* **1988**, *132*, 382.

(37) Watts, J. D.; Bartlett, R. J. *J. Chem. Phys.* **1993**, *93*, 6104.

(38) Kucharski, S. A.; Bartlett, R. J. *Theoretica Chimica Acta* **1991**, *80*, 387.

(39) Kucharski, S. A.; Bartlett, R. J. *J. Chem. Phys.* **1992**, *97*, 4282.

(40) Oliphant, N.; Adamowicz, L. *J. Chem. Phys.* **1991**, *94*, 1229.

(41) Yabushita, S.; Zhang, Z.; Pitzer, R. M. *J. Phys. Chem. A* **1999**, *103*, 5791-5800.

(42) COLUMBUS 2001.

(43) Douglas, M.; Kroll, N. M. *Ann. Phys. (New York)* **1974**, *82*, 89-155.

(44) Jansen, G.; Hess, B. A. *Phys. Rev. A* **1989**, *39*, 6016-6017.

(45) Roos, B. O.; Lindh, R.; Malmqvist, P. A.; Veryazov, V.; Widmark, P. O. *Chemical Physics Letters* **2005**, *409*, 295-299.

(46) Stoll, H.; Peterson, K. A.; Merritt, J. M.; Heaven, M. C. *J. Phys. Chem. A* **2009**, *113*, 12353-12355.

(47) Merritt, J. M.; Bondybey, V. E.; Heaven, M. C. *J. Chem. Phys.* **2009**, *130*, 144503/1-144503/9.

(48) Kohler, S.; Deissenberger, R.; Eberhardt, K.; Erdmann, N.; Herrmann, G.; Huber, G.; Kratz, J. V.; Nunnemann, M.; Passler, G.; Rao, P. M.; Riegel, J.; Trautmann, N.; Wendt, K. *Spectrochimica Acta, Part B: Atomic Spectroscopy* **1997**, *52B*, 717-726.

Table VI.1. Vibronic term energies for the low-lying vibronic states of HfF^+

v	$X^1\Sigma^+$	$^3\Delta_1$	$^3\Delta_2$	$^3\Delta_3$
0	0.0	978.0	2151.7	3935.9
1	785.8	1735.7	2909.4	4697.4
2	1565.4	2487.2	3658.4	
3	2339.0	3236.1	4404.5	
4	3105.5			
5	3867.4			
6	4624.2			

Units of cm^{-1}. The 1-σ errors are 0.5 cm^{-1}.

Table VI.2. Molecular constants for HfF^+

	$X^1\Sigma^+$	$^3\Delta_1$	$^3\Delta_2$	$^3\Delta_3$
T_0	0.0	978.0(10)	2151.7(10)	3935.9(10)
ω_e	791.2(5)	761.3(10)	762.3(10)	[761.5(5)][a]
$\omega_e x_e$	2.95(10)	2.18(25)	2.88(25)	-
B_0	0.304(5)	0.301(5)	0.300(5)	0.308(5)

Units of cm^{-1}. 1-σ errors are given in parentheses.

a. $\Delta G_{1/2}$ is given as only the v=0 and 1 levels were recorded for this state.

Table VI.3. Spectroscopic constants for neutral ThF from LIF measurements.

State	Ω	ν_0 (cm^{-1})	B (cm^{-1})
$X^2\Delta$	1.5	0.0	0.237(5)
{19.92}	1.5	19924.6(2)	0.224(5)
{20.44}	1.5	20443.7(2)	0.220(5)
{20.95}	1.5	20951.5(2)	0.219(5)

Table VI.4. Spectroscopic constants for ThF^+ from PFI-ZEKE measurements

State[1]	ν	E (cm^{-1})	B_v (cm^{-1})	ω_e (cm^{-1})	$\omega_e x_e$ (cm^{-1})
$X\ ^1\Sigma^+$	0	0, {IE=51581(3)}	0.245(5)	656.8(10)	1.85(25)
	1	653.2(5)	0.244(5)		
	2	1302.5(5)	0.244(5)		
	3	1948.3(5)	0.242(5)		
$A\ ^3\Delta_1$	0	315.0(5)	0.246(5)	658.3(10)	2.3(5)
	1	968.7(5)	0.244(5)		
	2	1617.9(5)	0.242(5)		
$B\ ^3\Delta_2$	0	1052.5(5)	0.243(5)	656.5(10)	1.9(5)
	1	1705.2(5)	0.243(5)		
	2	2354.3(5)	0.244(5)		
$C\ ^3\Delta_3$	0	3150(15)		665(15)[2]	
	1	3815(15)			
D ($^3\Pi_0$)	0	3395(15)		640(15)[2]	
	1	4035(15)			

1. It is possible that the ground and first electronic state assignments could be reversed. See text for details. The alphabetic labels correspond to those used in Fig. 4. The assignment for state D is tentative.

2. $\Delta G_{1/2}$ values.

Table VI.5. Spectroscopic constants for ThF^+ from LIF measurements

State	ν_0 (cm^{-1})	B (cm^{-1})	R-Bandhead (cm^{-1})
$X(^1\Sigma^+$ or $^3\Delta_1)$	0	0.245(5)	---
[19.36] ν=0	19361.1(2)	0.227(5)	19364.2(5)
[19.36] ν=1	19930.9(2)	0.226(5)	19933.6(5)
[19.36] ν=2	20498.1(2)	0.225(5)	20500.7(5)
{20.72}	20718.2(2)	0.224(5)	20720.8(5)
[19.36] ν=3	21062.2(2)	0.223(5)	21064.7(5)

Table VI.6. Calculated spectroscopic constants for ThF^+

State	E_e/cm^{-1}	ω_e/cm^{-1}	$R_e/Å$
$^1\Sigma^+$	0.0	659.8	1.981
	[143.3]	[663.6]	[1.979]
	(500.7)	(672.3)	(1.975)
$^3\Delta_1$	65.5	651.1	1.993
	[0.0]	[652.6]	[1.993]
	(0.0)	(654.1)	(1.992)
$^3\Delta_2$	955.3	651.9	1.993
	[889.7]	[653.4]	[1.992]
	(889.5)	(654.9)	(1.991)
$^3\Delta_3$	2222.9	652.7	1.992
	[2157.1]	[654.2]	[1.991]
	(2156.8)	(655.7)	(1.990)

For each state the values in the first row are from CCSDT(Q) calculations (see the text). The values in the second row, given in square brackets, are from CCSDT calculations, while those in the third row, given in parentheses, correspond to CCSD(T). Spin-orbit coupling is included in each case. See the text.

Table VI.7. Measured and calculated term energies for HfF^+

	Exp.	Theory $(10e)^a$	Theory $(20e)^b$
$X^1\Sigma^+$	0	0	0
$^3\Delta_1$	993	1599	1633
	[1173]	[1208]	[1195]
$^3\Delta_2$	2166	2807	2828
	[1785]	[1517]	[1445]
$^3\Delta_3$	3951	4324	4273

Units of cm^{-1}. The numbers in square brackets are the energy differences between successive components of the $^3\Delta$ state.

a. Reference [4] with explicit treatment of 10 valence electrons.

b. Reference [4] with explicit treatment of 20 valence electrons.

Figure VI.1. Resonantly enhanced two photon ionization spectrum showing the rotational structure of the HfF [28.6]3/2-$X^2\Delta_{3/2}$ 0-0 transition. The downward going trace is a simulation, as described in the main text. The rotational temperature for the simulation was 25 K.

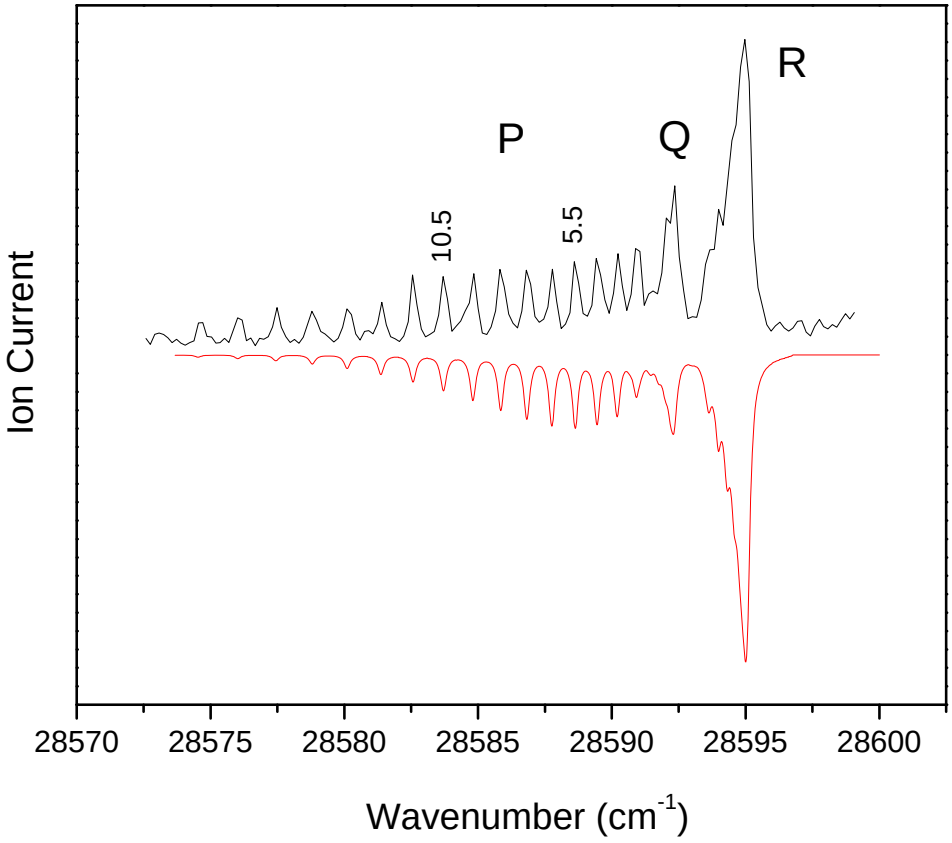

Figure VI.2. PFI-ZEKE survey scan of the lower energy states of HfF^+.

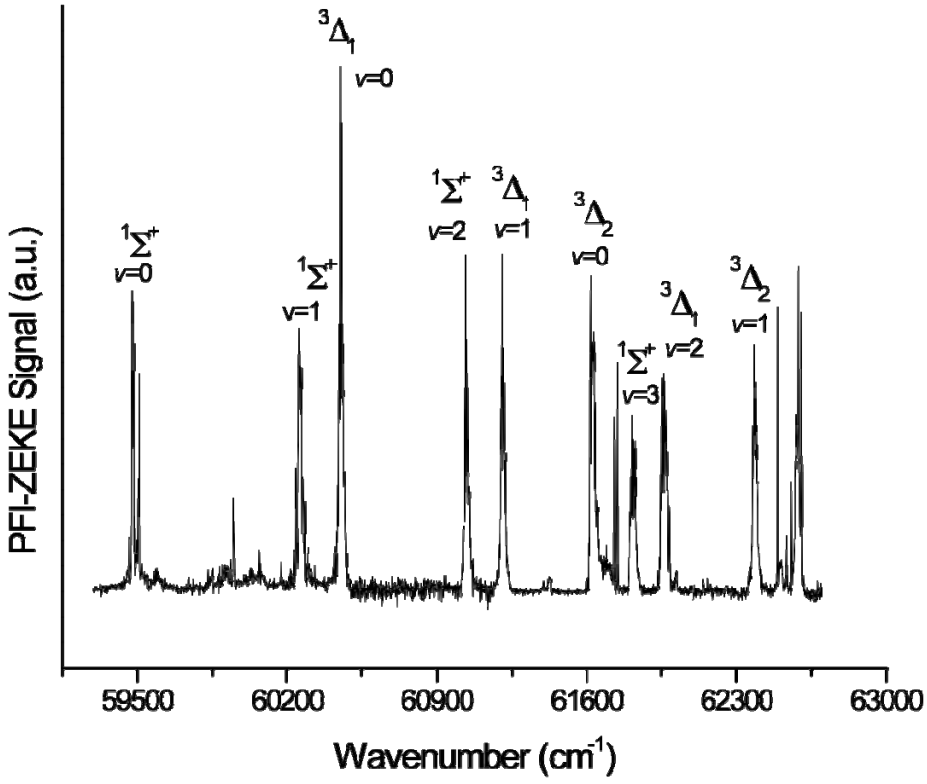

Figure VI.3. Rotational structure of the $X^1\Sigma^+$, v=0 level of HfF^+. The features marked with asterisks are accidental one-color, two photon resonances.

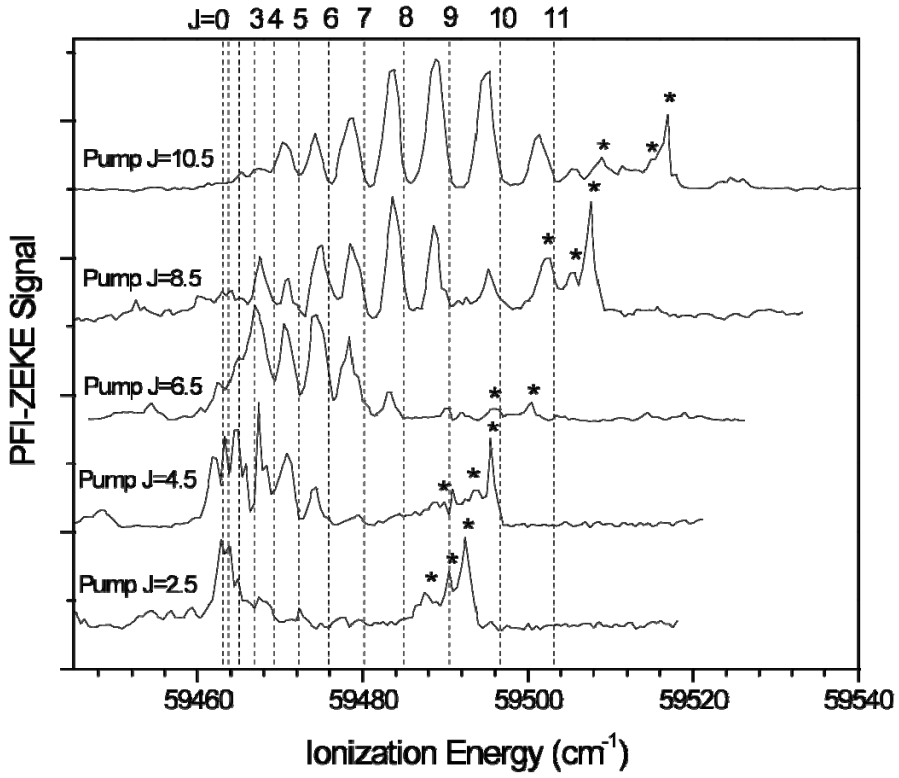

Figure VI.4. Low resolution survey spectrum of ThF recorded using 1+1' REMPI with mass-selected ion detection.

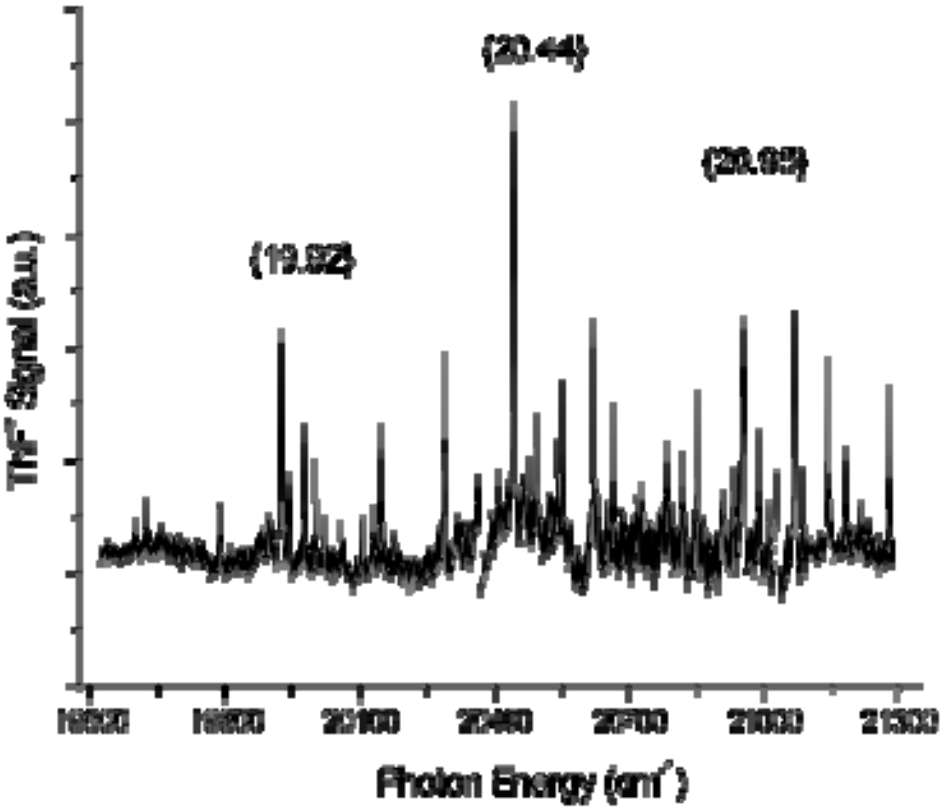

Figure VI.5. Laser induced fluorescence of the ThF {20.95}3/2-$X^2\Delta_{3/2}$ band. The upper trace is the experimental data and the lower trace is a simulation. The simulation is for a linewidth of 0.06 cm^{-1} and a rotational temperature of 35K. The spectrum clearly defines the lowest R- and P-branch lines. The {19.92} and {20.44} bands showed similar rotational structures.

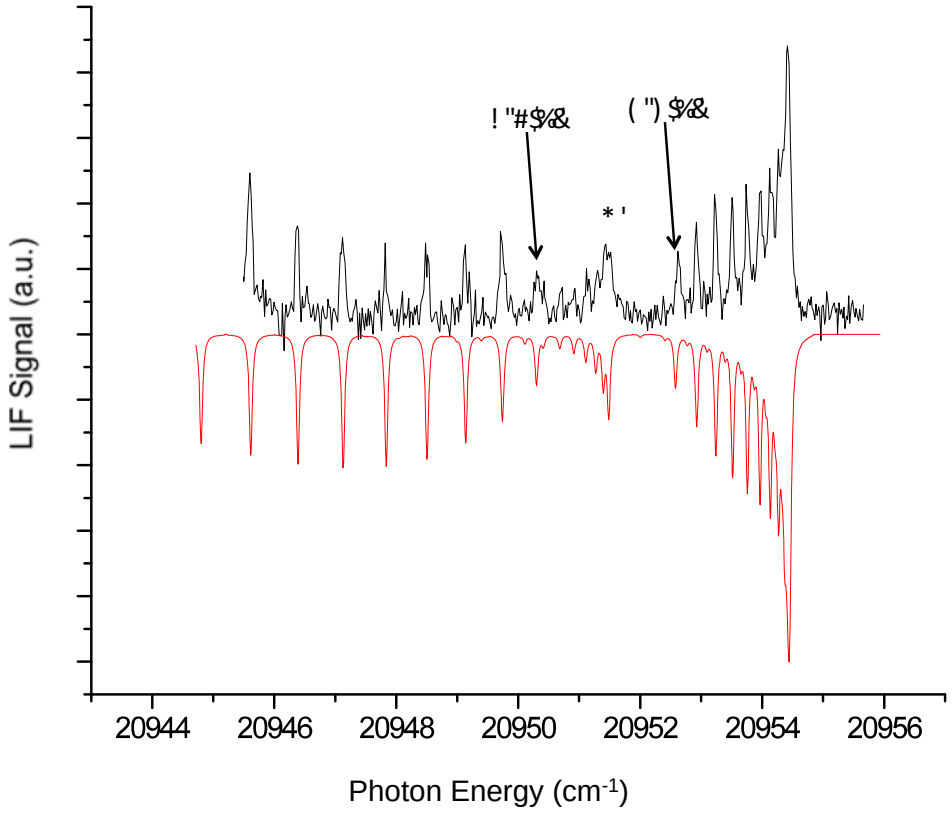

Figure VI.6. (a). Dispersed fluorescence spectrum taken by exciting the R-branch band head of the ThF {20.95}3/2-$X^2\Delta_{3/2}$ transition. Emission is observed only to vibrational levels of the ground $X^2\Delta_{3/2}$ electronic state. (b). Dispersed fluorescence taken while pumping the R-band branch head of the ThF {20.44}3/2- $X^2\Delta_{3/2}$ band. Emission is observed to the ground $X^2\Delta_{3/2}$ electronic state and an excited electronic state that is most probably $X^2\Delta_{5/2}$.

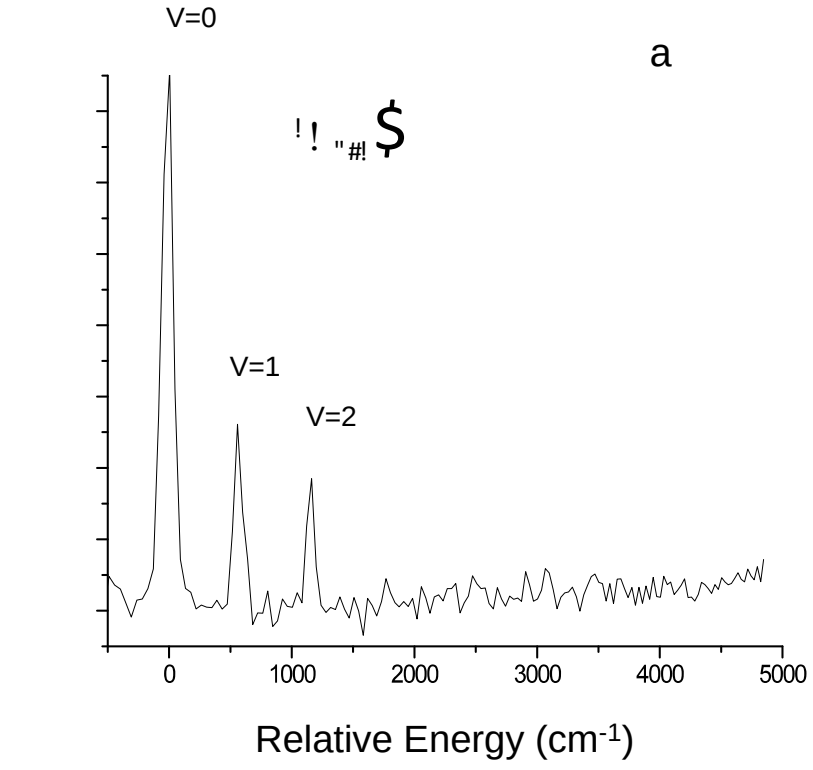

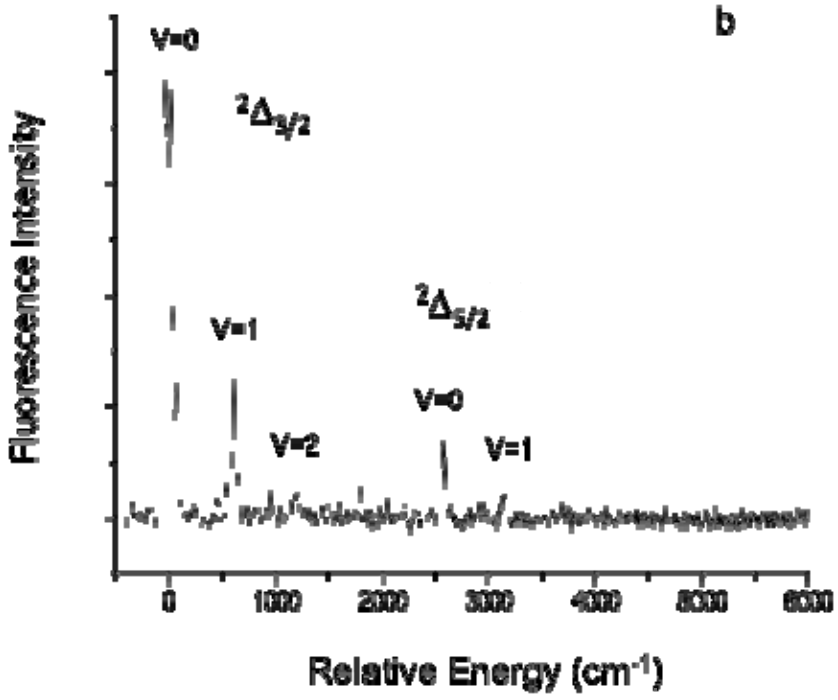

Figure VI.7. Low resolution PFI-ZEKE survey scan of ThF^+. Note that the vertical scale on trace (b) has been decreased by a factor of 4 as compared to trace (a). The intensity of the origin band was much larger than that of other bands. The amplifier gain used in recording trace (a) was such that the most intense part of the origin band was off-scale.

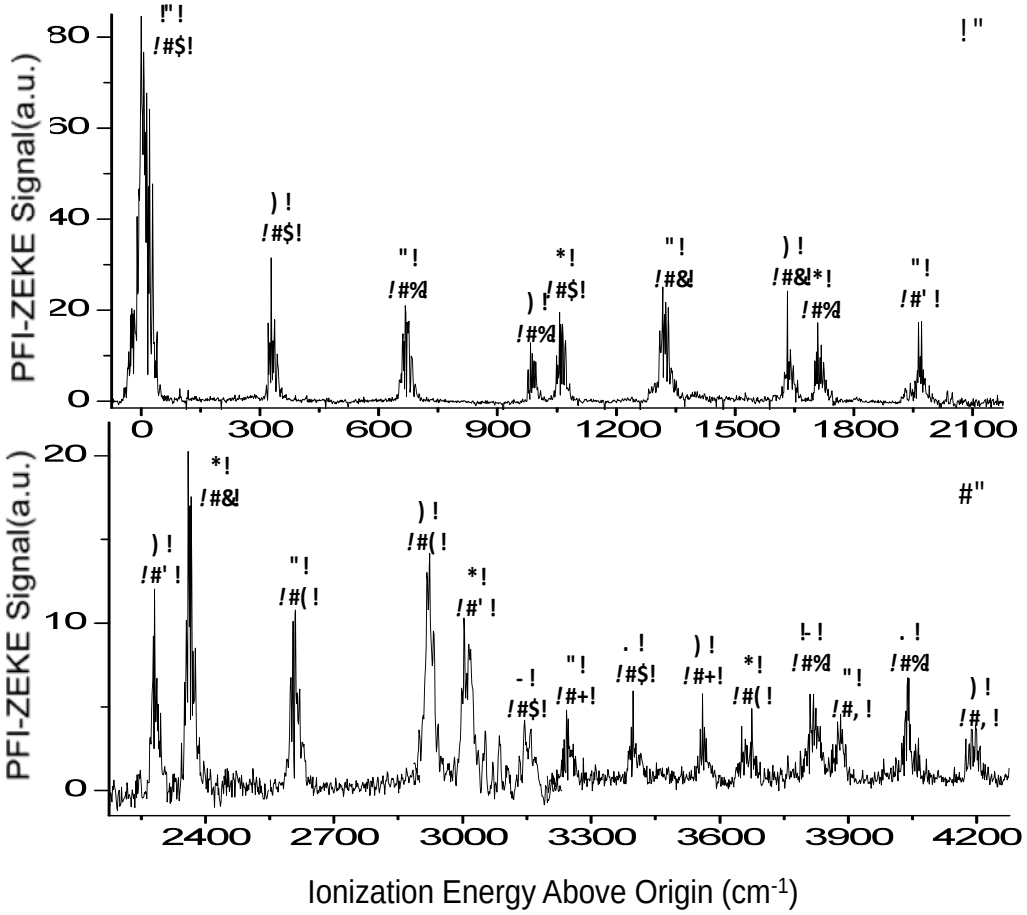

Figure VI.8. Rotationally resolved PFI-ZEKE spectrum of the ThF^+ origin band taken using initial excitation of the [20.95]3/2 – $X^2\Delta_{3/2}$ P(7.5) line.

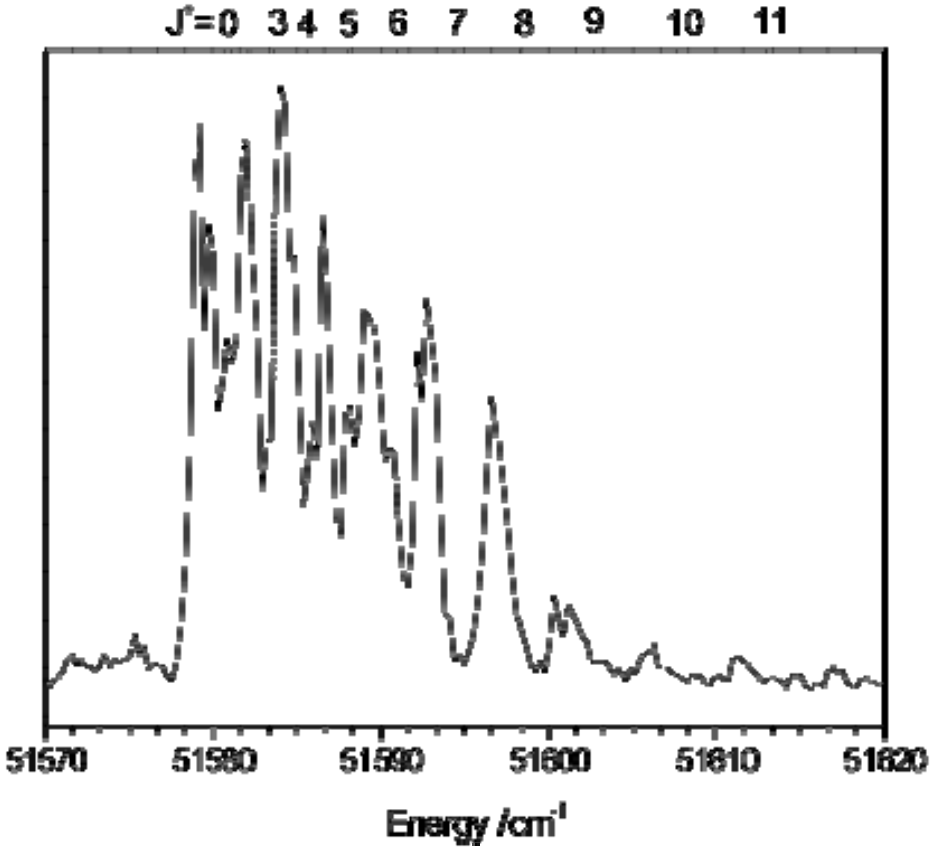

Figure VI.9. Low-resolution LIF survey scan showing transitions of Th, Th^+, ThF, ThO and ThF^+. In this measurement a pulsed 193 nm laser was used to ionize species in the expanding ablation plume. Labeled features are from the ThF^+ ion.

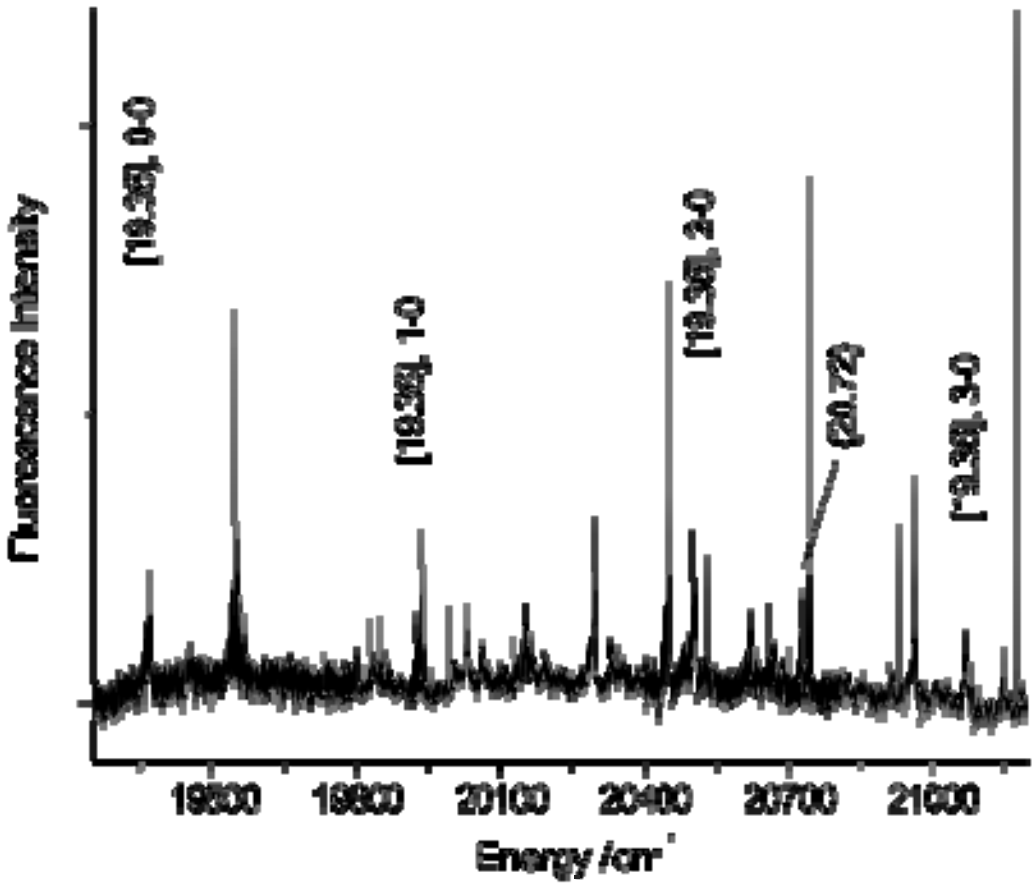

Figure VI.10. Laser induced fluorescence spectrum of the ThF^+ [19.36] ν'=3 - X band. The upper trace is experimental and the lower trace is a simulation. The latter had a linewidth of 0.06 cm^{-1} and a rotational temperature of 85K. A $^1\Pi_1$-$^1\Sigma^+$ transition type was assumed, but it is difficult to verify this choice as the assignment of the lowest R, Q or P branch lines is ambiguous. A $^3\Pi_0$-$^3\Pi_1$ simulation also gives satisfactory agreement with experiment.

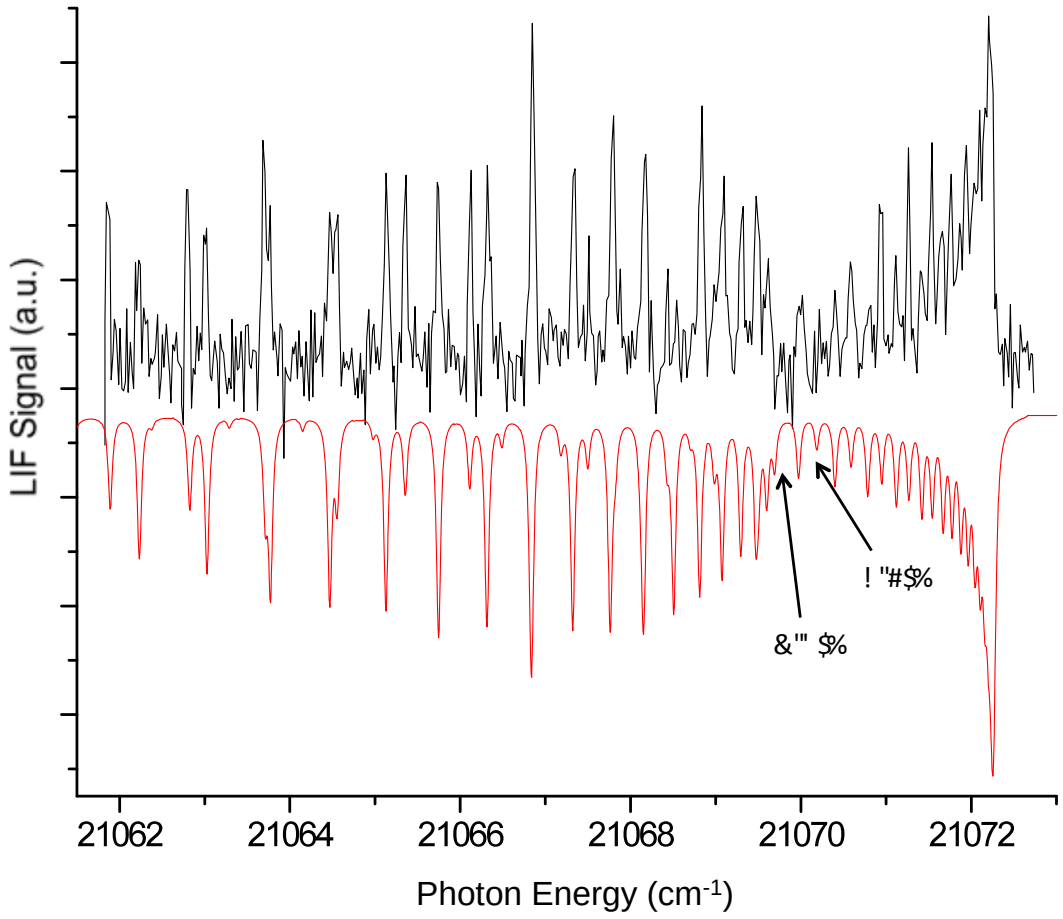

Figure VI.11. Dispersed fluorescence taken by exciting the R-branch head of the ThF^+ [19.36] ν'=3 - X band. Emission was to vibrational levels of the ground electronic state of ThF^+ only. The transitions to ν"=2 and 4 were below the noise level due to their small Franck-Condon factors.

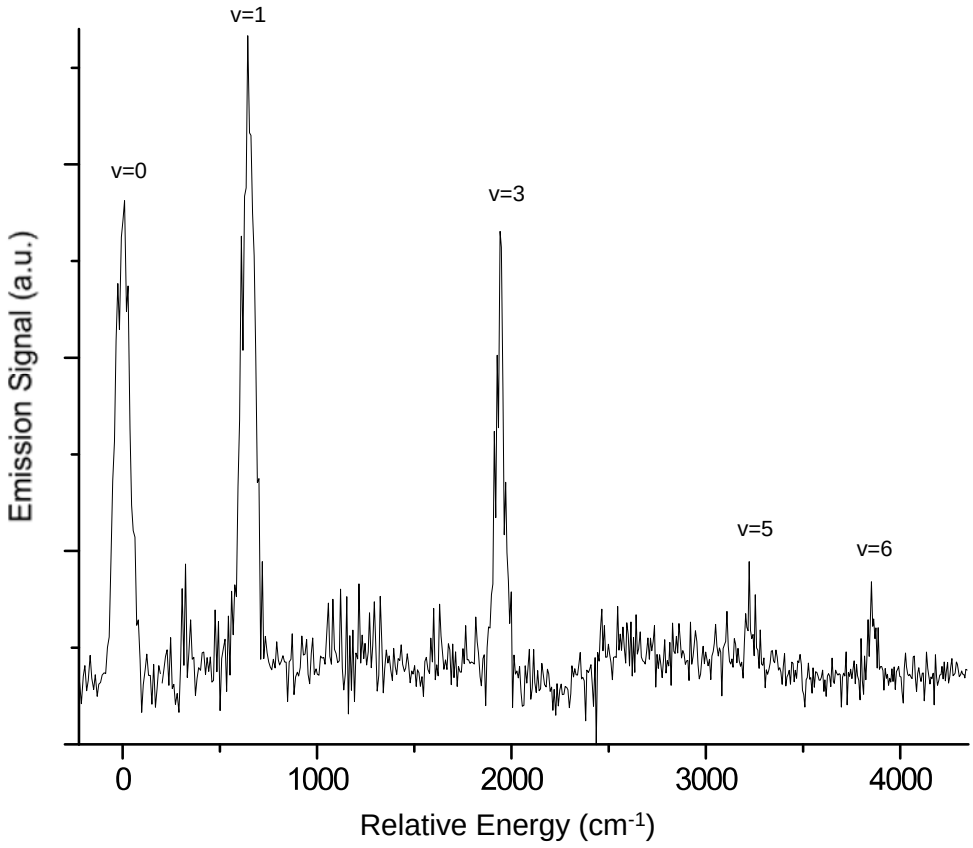

Figure VI.12. Energy level diagram for the low-lying vibronic states of HfF^+.

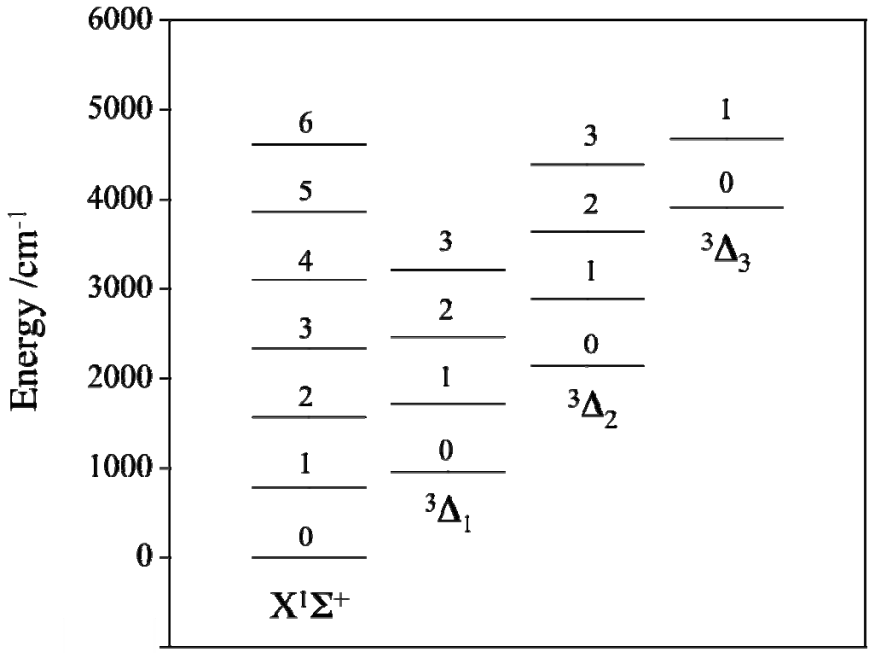

CHAPTER VII

SPECTROSCOPIC AND THEORETICAL INVESTIGATIONS OF UF AND UF^+

VII.1 INTRODUCTION

Diatomic molecules that contain actinides provide valuable model systems for studies of the electronic structures of heavy-element compounds, and the degree to which the 5*f* orbitals participate in actinide chemistry[1-23]. These molecules are suitable for investigations in the gas-phase, using moderate and high-resolution spectroscopic techniques, and for theoretical analyses using high-level, relativistic quantum chemistry models.

Previously, we have studied the electronic structures of UO[4,9,10,24], UO^+[6], ThO[2,8], ThO^+[7], ThF and ThF^+[1]. For these molecules we have found that the patterns of low-lying electronically excited states can be reliably anticipated and rationalized using ligand field theory (LFT) models[10,25]. The present study reports experimental and theoretical characterizations of UF and UF^+. In addition to having their own intrinsic merit, these molecules are of interest from the perspective of their relationship to other UX diatoms. UF is comparable to UH in that they are both expected to be ionic U^+X^- molecules, with the atomic metal cation perturbed by a closed-shell anion[23]. Due to the presence of a common 5f-orbital occupation, $U^+(5f^37s^2)F^-$ is closely related to the $U^{3+}(5f^3)O^{2-}$ cation. A similar connection exists between $U^{2+}(5f^37s)O^{2-}$ and the isoelectronic $U^{2+}(5f^37s)F^-$ cation.

While the electronic angular momentum states of UO^+ and UF are both dictated by the $5f^3$ configuration, the strength of the ligand field perturbation is expected to be greater for UO^+. Hence, comparisons of the electronic energy level patterns should yield insights regarding the electric field destabilization of the free-ion orbitals. Similarly, comparisons of UO and UF^+ will illuminate the effect of the ligand on the $5f^37s$ configuration under conditions where the oxidation state of the metal is unchanged. A significant difference between the electronic structures is

expected. For UO we have found that states from the $5f^37s$ and $5f^27s^2$ configurations are interleaved and mutually perturbing[10]. The smaller charge of F^- will not destabilize $U^{2+}(5f^37s)$ as strongly as the O^{2-} ligand does, so $5f^37s$ is expected to be further below $5f^27s^2$ in UF^+.

There have been no previous spectroscopic studies of UF^+, and the only observation attributed to UF describes a single IR absorption band at 400 cm^{-1}, recorded in a cryogenic Ar matrix[26]. An electron impact ionization study of UF yielded an ionization energy of 6.0±0.3 eV[27].

Early theoretical studies of UF and UH, performed by Krauss and Stevens[23], indicated that these molecules would have complicated patterns of low-lying excited states, making identification of the ground state a difficult matter. The 5f orbitals of U were shown to retain their atomic character and to not participate significantly in bonding. Higher-level calculations were carried out by Fedorov et al.[22], who predicted term energies, bond lengths and Morse potential energy curve parameters for 18 states in the 0-8300 cm^{-1} range. The ground state was predicted to be Ω=4.5 (where Ω is the unsigned projection of the electronic angular momentum along the bond axis) derived from the $5f^37s^2\ {}^4I_{4.5}$ atomic ion core.

Here we report rotationally resolved spectra for UF that were obtained using LIF and resonantly enhanced multi-photon ionization (REMPI) spectroscopy. Low-resolution dispersed fluorescence spectra were used to examine the lower energy vibronic states. Spectra for UF^+ were obtained using pulsed field ionization - zero kinetic energy (PFI-ZEKE) photoelectron spectroscopy. Results from ab initio electronic structure calculations, which were used to facilitate the assignment of the low-energy electronic states, are presented. Finally, the patterns of low-lying states for UF^+ and UF are compared to the results from previous studies of UO and UO^+.

VII.2 EXPERIMENTAL

The apparatus used in this study has been described in Section II, so only a brief description will be given here. UF was produced using a laser ablation source. The 1064 nm output of a pulsed Nd/YAG laser (~25 mJ, pulse duration 6 ns, Continuum Minilite II) was focused onto the surface of a uranium rod. The rod was continuously rotated and translated to expose a fresh surface for each shot. A solenoid valve, located behind the uranium rod, produced a gas pulse which served to entrain the ablated material into a carrier gas consisting of He + 0.1% SF_6. The mixture was then subjected to supersonic expansion, thereby cooling the ablation products. The backing pressure and gas pulse duration were typically 3.5 atm and 300 μs.

Laser induced fluorescence (LIF) spectra were recorded with the excitation laser positioned approximately 5 cm downstream from the expansion nozzle orifice. The output from a Coherent ScanMate Pro dye laser/Nd:YAG laser system was propagated perpendicularly to the direction of the gas expansion. Baffle arms were installed on the windows of the source chamber to reduce the amount of the scattered laser light. Fluorescence was collected along an axis that was perpendicular to both the laser and gas expansion axes. The fluorescence was detected by a Photonis XP2020 photomultiplier tube. When recording dispersed fluorescence (DF) spectra the emitted light was focused onto the slits of 0.25 m Ebert monochromator (Jarrell-Ash model 82-410, 1180 line/mm grating, 0.6 mm slit width).

Downstream of the LIF detection region, the core of the jet expansion entered a second differentially pumped chamber via a conical skimmer with a 5 mm orifice. This chamber housed a time-of-flight mass-spectrometer (TOFMS) operating with a 250 V/cm field between the repeller and extractor plates. In the TOFMS the molecular beam was crossed by two counter-propagating beams from tunable dye lasers (Continuum ND6000 and a Coherent ScanMate Pro). Two-color two-photon (1+1') resonantly enhanced multiphoton ionization (REMPI) spectra were recorded by scanning the Coherent ScanMate Pro dye laser to search for resonant intermediate excited states, and ionizing the excited molecules with the light from the ND6000 dye laser.

Spectra were recorded using mass-resolved ion detection. For the two-color spectra the laser beams were temporally overlapped and synchronized with the pulsed molecular beam using digital delay generators (Stanford Research Systems DG 535). One color (1+1) REMPI spectra were recorded with the Coherent ScanMate Pro dye laser alone, when the energy of the first photon was greater than half of the UF ionization energy.

Photoionization efficiency (PIE) spectra were recorded to determine the ionization energy of UF using the same experimental arrangement as that for REMPI. The only difference being that the pump laser wavelength was fixed on an established transition of neutral UF, and the ionization laser wavelength was scanned until the onset of the UF^+ ion signal was observed in the mass spectrometer.

Pulsed field ionization zero electron kinetic energy (PFI-ZEKE) spectra were recorded for the UF^+ molecular ion using a two-color scheme via a resonant intermediate state. For these measurements the repeller and the extractor electrodes were both held at -4.0V to give field free conditions during photo-excitation. The electric field used for ionization was applied 2.5 μs after the laser pulses. The voltage on the extractor electrode was pulsed to give an electric field of 0.43 V/cm, causing ionization of the molecules in long-lived high-*n* Rydberg states, and acceleration of the electrons towards a microchannel plate (MCP) detector located 10 cm below the repeller electrode. Transitions in the PFI-ZEKE spectra were confirmed to be from UF^+ by detuning the pump laser from resonance with the intermediate state.

The REMPI and the LIF spectra typically displayed resolutions of 0.4-0.5 cm^{-1} and 0.15 cm^{-1}, respectively. Installing an intracavity etalon in the ScanMatePro laser improved the resolution of the LIF spectra to 0.05 cm^{-1}. Rotationally resolved PFI-ZEKE spectra displayed a resolution of about 1.0 cm^{-1}. LIF and REMPI spectra were calibrated using observed atomic U lines**.** PFI-ZEKE data were calibrated by recording the I_2 B-X LIF spectrum[30] using the fundamental output from the dye laser. The monochromator was calibrated using emission lines from a Hg lamp. Band centers for the emission data were accurate to about ~15 cm^{-1}.

VII.3 NOTATION

In the following we label the higher energy (>10000 cm^{-1}) excited states of UF and UF^+ using notation previously applied to lanthanide diatomic molecules[25]. The upper electronic states are labeled by $[T_0/10^3]\Omega$ and T_0 is the term energy given in wavenumbers. Here we include three digits to obtain adequate specification. For states below 10000 cm^{-1} the notation (n)Ω is used, where n designates the n-th state for given value of Ω, in ascending energy order. The electronic ground state is uniquely identified as X(1)Ω.

VII.4 CALCULATIONS

All electronic structure calculations for UF and UF^+ were performed using the MOLPRO 2010 package[31]. To account for relativistic effects, a 60 electron pseudopotential developed by Dolg et al.[17] was used. For the electrons treated explicitly, a (14s13p10d8f6g)/[6s6p5d4f3g] ANO contracted basis set[17] was centered on the U atom, and the aug-cc-pVTZ Dunning correlation consistent basis set[32] was used for the F atom. Both UF and UF^+ are open-shell molecules with 3 and 4 unpaired electrons. Potential energy curves (PEC's) were calculated for the range of internuclear distances R=1.7-5.0 Å using the state-averaged CASSCF method. MOLPRO uses the C_{2v} point group for a heteronuclear diatomic molecule. The active space for the UF^+ and UF calculations was chosen to include 13 orbitals, with 5 functions of a_1 symmetry, $3b_1$, $3b_2$ and $2a_2$. They have predominantly atomic U 7s (a_1), 5f ($2a_1$, $2b_1$, $2b_2$, $1a_2$), 6d(a_1, a_2) and 6d7p (a_1, b_1, b_2) character. Inclusion of 3 more a_1, b_1 and b_2 low-energy orbitals, with mostly U 6d7p, character did not appreciably change the results of the CASSCF calculations. The highest energy doubly-occupied orbitals had predominantly F 2*s* (a_1) and 2p (a_1, b_1, b_2) character and were not included in the active space. It was expected that excitations from these orbitals would be unimportant for the ground and low-lying states of UF and UF^+, at least near the equilibrium bond length. The same or similar active spaces were used in previous high-level studies[17,18,22,33]of UF, UH and

UH_2. The states included in the state-averaged CASSCF calculations for UF^+ were quintets and triplets with Λ=0-6, correlating with the f^3s configuration of U^{2+}, and Λ=0-8 quintets correlating with the f^3d configuration. For the UF calculations, quartet states with Λ=0-6 and sextets with Λ=0-8 were included. These states correlated with the f^3s^2 and f^3ds configurations of U^+. The program package LEVEL 8.0[34] was used to solve the nuclear Schrödinger equation for each PEC to determine the vibrational and rotational constants.

In calculations for atomic U^{2+}, only the f^4 ^{5}I and f^3s, ^{5}I and ^{3}I terms were included. An active space that originally included 13 orbitals (7s, 6d and 5f sub-shells of U) was reduced to 8 (7s and 5f sub-shells) because the energies of the f^4 and f^3s levels after CI were insensitive to inclusion of the 6d orbitals.

The state-averaged CASSCF wavefunctions were used as a reference for CASPT2 calculations (rs2 and rs2c options in MOLPRO). An Ionization Potential-Electron Affinity (IPEA) level shift[35] of 0.25 a.u. (option IPEA=0.25) was used to remove intruder state problems and facilitate convergence. In calculations for UF, a slightly different value for the IPEA shift of 0.27 a.u. was used. For atomic U^{2+} calculations, multireference configuration interaction with single and double excitations and the Davidson correction for quadruple excitation (MRCI-SD + Q) was used instead of CASPT2.

CASPT2 energies were obtained for only one value of bond length, near the ground state potential energy minimum. For UF^+ the energies were calculated at R=2.000 Å and for UF at R=2.015 Å. The spin-orbit (SO) interaction was calculated using ECP SO parameters and CASSCF wavefunctions to calculate the SO matrix elements. The spin-free components of the diagonal elements of the matrix for the spin-orbit operator were set to the CASPT2 energies.

The term energies and molecular constants of the spin-free states of UF^+ at the CASSCF and CASPT2 levels of theory are given in Table VII.1. The first column contains the term symmetry and leading configuration at the atomic ion limit. The second and the third columns list

the CASSCF and CASPT2 term energies, and the last three columns list the vibration frequency, anharmonicity and equilibrium bond length.

Table VII.2 contains calculated spin-orbit energies of low-lying electronic states of UF^+ and U^{2+}. The first column lists the level assignment and the second column has the CASPT2-SO energy for each level. The third and fourth columns list experimental data for UF^+ (current work) and UO[10] for comparison. The fifth and sixth columns contain experimental[36] and calculated (this work) energies for the U^{2+} ion. The seventh column lists the state assignments for U^{2+}.

Table VII.3 presents the spin-orbit energies for low-lying electronic states of UF. The first column has the level assignment and the second column contains the calculated CASPT2-SO energies. The third column lists results from the calculations by Fedorov et al.[22] the fourth column presents the experimental data for UF (current work) and the fifth column has the experimental energies of UO^+ from Goncharov et al.[6]. The last three columns list the term energies and level assignments of U^{3+} and U^+ ions, where the U^{3+} energies were calculated by Ruiperez et al.[37] and U^+ data was taken from the Steinhaus et al.[38]

VII.5 RESULTS

UF^+ ions were readily observed in the mass spectrometer using non-resonant two-photon photoionization with unfocused UV light in the wavelength range 250-300 nm, with ~1 mJ power and 6-7 mm beam diameter. The ablation source conditions (backing pressure, composition of the carrier gas, duration of the gas pulse, power of the ablation laser and relative timings of the gas pulse, ablation and probe lasers) were varied to optimize the production of uranium fluoride.

The large non-resonant multiphoton photoionization cross-section of UF allowed for easy detection, but at the same time complicated the recording of REMPI spectra by increasing the background signal. Several regions were found where REMPI spectra of UF showed resonant enhancement of the signal, although with poor signal-to-noise ratios. Better quality spectra were

obtained using LIF detection. Figure VII.1 displays a rotationally resolved LIF spectrum of UF taken over the 18615-18630 cm^{-1} region. The lower trace is a simulation generated with the PGOPHER program[39]. In the simulation, Ω′ and Ω″ were determined to be 3.5 and 4.5 respectively, and rotational temperature T was set to 9K.

Another region were the REMPI spectrum had shown resonant enhancement was centered at 19945 cm^{-1}. Unfortunately, as Fig. VII.2 demonstrates, an intense transition of UO occurred at the same energy and overlaid the UF band, thus preventing the recording of a clean high-resolution LIF spectrum of UF in this region. Consequently, only a lower-resolution REMPI spectrum was recorded for this transition, which provided a rotational band contour. A contour simulation was performed for this transition (bottom trace), and the intensity envelope was found to be consistent with Ω'= 5.5←Ω"=4.5. In the following we label this excited state as [19.9]5.5.

The DF spectrum of UF shown in Fig. VII.3 was collected with the ScanMate Pro laser tuned to the Q-branch of [18.6]3.5-X(1)4.5 transition. Two intense bands were observed with red-shifts of 0 cm^{-1} and 650 cm^{-1} relative to the excitation energy, and a weaker band was found at 435 cm^{-1}. The monochromator only allowed for resolution of the vibronic structure. The wavelength range of the DF spectrum was limited by the PMT sensitivity, which decreased rapidly beyond 600 nm. Hence, the lower energy states that could be observed were limited to those lying no more than 2500 cm^{-1} above the ground state of UF.

Fig. VII.4 shows a low-resolution PFI-ZEKE survey spectrum for UF^+. This trace is composed of multiple shorter range scans for which several laser dyes were used. For the lower energy part of the spectrum (<53900 cm^{-1}), the first laser was tuned to the [18.6]3.5 excited state of UF. For higher total energies (>53900 cm^{-1}), the [19.9]5.5 state of UF was used as the intermediate. The intensities have not been corrected for variations of the laser power with wavelength.

In order to record rotationally resolved PFI-ZEKE spectra for UF^+ it was essential to prepare excited UF molecules in a specific rotational state. The [18.6]3.5 transition facilitated

single rotational state excitation via the well-resolved P-branch lines. Typically the P(4.5) line was utilized, but a few experiments were performed using excitation of the P(5.5) or P(6.5) lines. When the [19.9]5.5 transition was used as an intermediate state the pump laser was tuned to the red edge of the R-branch to excite the R(4.5) line. This approach allowed for selective excitation of the J′=5.5 level, as confirmed by PFI-ZEKE spectra.

The rotational structure of the UF^+ ground state v=0 level is displayed in Fig. VII.5. The bottom trace was recorded via the J'=3.5 intermediate rotational level of the neutral UF and the top trace via J'=4.5. The energy scale on this graph is relative to the energy of the UF X(1)4.5 v''=0, J''=4.5 level.

VII.6 ANALYSIS AND DISCUSSION

VII.6.1 UF

The UF transitions to the [18.6]3.5 and [19.9]5.5 states both originated from the ground state zero-point level, as confirmed by IE measurements. The observation of Ω"=4.5 for the ground state was in agreement with the prediction by Fedorov et al.[22] for a $^4I_{4.5}$ ground state. The rotational constants were determined using the least squares fitting routine in PGOPHER[39]. In the fit, Ω″=4.5 and Ω′=3.5 with Hund's case (c) angular momentum coupling was assumed for both the ground and excited states. The centrifugal distortion constants and Ω-doubling parameters were too small for determination using these low-temperature data. Consequently, only the band origin and the B rotational constants were treated as variables, with all other constants set to zero. The bond lengths derived from the rotational constants were R'=2.020 Å and R"=2.044 Å. Given the small difference between these lengths, it was expected that Δv=0 bands would dominate the spectrum of the [18.6]3.5 - X(1)4.5 transition.

The [19.9]5.5 -X(1)4.5 transition was not fully resolved, but the gap between the Q- and R-branches was sufficiently well-defined that the PGOPHER[39] rotational simulations clearly

indicated the value of Ω=5.5 for the excited state. In the simulation, the ground state rotational constants was fixed at B″=0.2348(2) cm^{-1}, as determined previously from the [18.6]3.5 -X(1)4.5 transition. The molecular constants determined from the simulations of these two bands are collected in Table VII.4.

The pattern of low-lying electronic states for UF can be anticipated using a LFT model. The molecule is formally considered as a U^+ ion, with electronic angular momentum J_a, perturbed by the electric field of a closed-shell F^- ligand. For a given value of J_a the lowest energy molecular state has the maximum projection of J_a on the diatomic axis ($\Omega=J_a$). When the J_a vector is tipped away from the intermolecular axis, the value of Ω decreases and the region of higher electron density surrounding the metal center is rotated towards the negatively charged ligand. Hence, the states with lower Ω values that correlate to the same J_a atomic level have higher energies. The ground state of UF is expected to be the X(1)4.5 state arising from the $U^+(f^3s^2, {}^4I_{4.5})F^-$ configuration. In support of this assignment, the ground state was confirmed to be an Ω=4.5 state. Based on the LFT model described above, the first series of excited states should show Ω decreasing from (1)3.5 to (1)0.5. This pattern is evident in the theoretical energies presented in Table VII.3. Similar ladders of states were observed previously for the low energy states of UO and UO^+ [6,9].

The bands in the DF spectrum were assigned as the [18.6]3.5 → X(1)4.5 transition at the origin, the [18.6]3.5 → (1)3.5 transition at 435 cm^{-1} and [18.6]3.5 → (1)2.5 transition at 650 cm^{-1}. The v″=1 band of the [18.6]3.5 → X(1)4.5 transition was not observed, presumably because it had small Franck-Condon factor and was most likely obscured by the strong [18.6]3.5 → (1)2.5 band. To check this interpretation, Franck-Condon (FC) calculations for the 0-0 and 0-1 bands of the [18.6]3.5 → X(1)4.5 transition were performed in which the ground and excited states were approximated by Morse potentials with parameters calculated by Fedorov et al.[22] for the UF $^4I_{9/2}$ ground state (D_e=37316 cm^{-1}, α=1.5832 $Å^{-1}$), R_e=2.020 Å for the ground state, and 2.044 Å for

the excited state. The potential energy curve of the [18.6]3.5 state was unknown and it was assumed that it could be approximated near the equilibrium by the Morse curve of the ground state. The FC calculation was carried out using the LEVEL 8.0 package[34]. The calculated FC probabilities were 91.4% and 7.8% for 0-0 and 0-1 vibrational bands, respectively. The vibrational frequency of the ground state derived from the Morse parameters calculated by Fedorov et al.[22] was 597 cm^{-1}.

The electronic structure calculations performed in this study were in good agreement with the DF spectrum. The 1(3.5) and 1(2.5) excited states were predicted at 415 cm^{-1} and 678 cm^{-1} respectively (Table VII.3). The previous high-level calculations by Fedorov et al.[22] predicted these states at 61 and 805 cm^{-1}, respectively. The latter intervals are clearly inconsistent with the LFT model.

As noted in the introduction, there was only one other attempt to obtain spectra for UF. Hunt et al.[26] produced uranium fluorides by laser ablation of a uranium target into a flow of Ar seeded with F_2 or ClF. The products were trapped in solid Ar matrices. IR absorption spectra revealed bands at 400 and 446 cm^{-1} that were assigned to UF and UF_2, respectively. This very low vibrational frequency for UF is difficult to explain. Both the present calculations and those of Fedorov et al.[22] yielded ground state vibrational frequencies in excess of 590 cm^{-1}. If the 400 cm^{-1} band was associated with UF, it would indicate a remarkably large Ar matrix perturbation. In this context it should be noted that large Ar matrix shifts of the vibrational frequencies of CUO and UO_2 have been reported[40-43]. In these instances the shifts were attributed re-orderings of the low-lying electronic states caused by strong guest-host interactions. However, this model does not appear to be applicable to UF as the low-lying states are all predicted to have vibrational frequencies above 550 cm^{-1}. The DF spectrum for gas phase UF shows an electronically excited state at 435 cm^{-1}, so it is plausible that it was the (1)3.5-X(1)4.5 transition that was seen for matrix isolated UF. However, with this assignment it would be difficult to explain why an electric dipole forbidden transition would be observed, while the vibrational fundamental was not

detected. Hence, the present results cast some doubt on the species assignment for the matrix spectrum.

Of particular interest is the comparison between the energy levels of UF and UO^+ (Table VII.3), because the ground and lowest excited states of these molecules have the same $5f^3(^4I_{4.5})$ open-shell component of the atomic ion core. In UO^+ the ligand has higher effective negative charge than in UF, and repels the non-bonding 5f electrons of U more strongly. This effect is evident in Table VII.3, where it can be seen that the J_a=4.5, Ω=4.5 - 0.5 states of UF span 790 cm^{-1}, while the corresponding states of UO^+ are spread over 1325 cm^{-1}.

VII.6.2 UF^+

PFI-ZEKE measurements for UF yielded an IE value of 51148.4±0.5 cm^{-1} (6.34159(6) eV). This was consistent with the value of 6.0±0.3 eV determined previously by electron impact techniques. Combined with the IE for atomic uranium (6.194 eV[6]), the IE for UF shows that the UF^+ ion is 0.148 eV less deeply bound than the neutral molecule. This small change indicates that the 7s orbital is mostly non-bonding.

Above the ionization threshold, the PFI-ZEKE survey scan contained over 50 bands that were assigned as vibronic states of the UF^+ ion. Several bands at energies >54000 cm^{-1}, marked with asterisks in Fig. VII.4, belonged to another U containing species, most likely the UO^+ ion. Note that the [19.9]5.5-X(1)4.5 band of UF, used to access the intermediate state for this part of the survey scan, was overlapped by the UO [19.950]4-X(1)4 band[9]. UO^+ was previously examined using the PFI-ZEKE technique for the energy range that was 0-5200 cm^{-1} above ionization[6]. Transitions to UO^+ observed in the current work started at 5300 cm^{-1} above the ground state zero-point level. We did not attempt to assign these bands. Instead, the PFI-ZEKE spectrum with UO^+ only (without the addition of SF_6 to the carrier gas) was recorded and subtracted from the survey to identify the features that belonged to UF^+.

Rotationally resolved PFI-ZEKE spectra were recorded for all vibronic states of UF^+ observed in the survey, with exception of the bands of the Ω=0 states. The blue edges of rotational lines were fitted to the simple rigid rotor energy expression

$$\nu = IE + T_{\Omega,v} + B_{\Omega,v}J(J+1)$$

where *IE* is the ionization energy of UF, $T_{\Omega,v}$ is the vibronic term energy, $B_{\Omega,v}$ is the rotational constant and *J* is the rotational quantum number. Additionally, the lowest observed rotational level *J* of each band identified the Ω value for the electronic state of UF^+. For the vibronic bands of the 1(1) state a pronounced splitting of the Ω-doublet was observed. The rotational structure was fitted using the PGOPHER[39] package as an ($\Omega'=\Omega^+$)←($\Omega''=4$) transition. In the simulation only the *J*=4 rotational level was populated in the lower state. To allow for the relaxed ΔJ selection rules typically observed in PFI-ZEKE spectra, the transitions were simulated with L=6, $|M_L|=|\Omega'-\Omega''|$ spherical harmonic representing the transition moment. The energy difference between *e*- and *f*- parity levels was represented by the formula

$$\Delta\nu_{e/f}=qJ(J+1).$$

The simulation of the v=0 band of the (1)1 state is presented in the Fig. VII.6, where the upper and lower traces are the observed and simulated spectra, respectively. The strong feature to the red of the simulated transition was not included, but we assign it as the v=0 band of the (1)0 electronic state. Due to a small energy gap between the two bands (~4 cm^{-1}), strong parity-dependent interaction between (1)1 and (1)0 states occurs which is the primary cause of the large Ω-doublet splitting observed in the (1)1 state. Ω-doubling was not observed for vibronic bands of the (2)1 state, where the closest Ω=0 band was separated by ~20 cm^{-1}.

The vibronic term energies obtained for UF^+ were fitted to the anharmonic oscillator expression

$$T_{\Omega,v} = T_{\Omega,0} + \omega_e^{\Omega}v - \omega_e x_e^{\Omega}v(v+1)$$

to obtain vibrational frequencies, anharmonicities and the electronic term energies for each Ω state observed in the PFI-ZEKE spectrum. The results are listed in Table VII.5.

The energy level diagram shown in Fig. VII.7 illustrates the underlying structure of the electronic states of UF^+, and facilitates comparisons with the results from the theoretical calculations. In this diagram the UF^+ electronic term energies ($T_{v,0}$) are presented in stacks that share a common value for Ω. The black circles and red trianglespointing up are the experimental data and single-point CASPT2 energies, respectively. The energies of low-lying electronic states of UO are shown for comparison as blue triangles pointing down. The half-filled black circles to the right are the calculated MRCI-SD+Q energies of the 4 lowest levels of the $5f^37s$ configuration of U^{2+}. Experimental data are only available for the two lowest levels of the $5f^37s$ configuration. The calculated energies for these levels are in very close agreement with experiment (Table VII.2).

The energy level patterns of Fig. VII.7 can be readily understood in terms of a LFT model. The lowest energy configurations of the U^{2+} ion are $5f^37s$, $5f^36d$ and $5f^4$. The destabilizing effect of the ligand field is the least for the $5f^37s$ configuration because the diffuse 7s orbital can polarize away from the ligand. For example, the 7s and 5fδ orbitals are shown in Fig. VII.8. Both orbitals are plotted as isodensity surfaces (D=0.02) that contain ~82% of 7s and ~97% of 5fδ electron density. The 7*s* orbital is much larger and much more diffuse than 5*fδ*. Due to mixing with the 7pσ and 6dσ orbitals, 7*s* readily polarizes and has a low electron density near the ligand.

The lowest two atomic levels of $5f^37s$ configuration are J_a =4 and J_a =5. They can be adequately described as the $5f^3\ ^4I_{4.5}$ core interacting with the 7s electron. Each of these atomic states gives rise to a ladder of UF^+ states starting with Ω=4 and Ω=5, respectively. The energy gap between the lowest state in each ladder is very close to the energy gap between the atomic ion J_a = 4 and 5 levels. States of UF^+ belonging to the same atomic ion configuration have very similar bond lengths and vibrational constants, as can be seen from the data given in Table VII.5. The predicted single-point energies near the equilibrium distance for the Ω=4,3,2,1,0 and

Ω=5,4,3,2,1,0 levels, presented in Table VII.2 and Fig. VII.7, reflect the structure expected from the LFT model, and are in good agreement with the experimental results. Vibrational frequencies of the $5f^3 7s$ configuration states (Table VII.1) were calculated at the spin-free level and therefore cannot be directly compared to the experimental values. However, both calculated and measured vibrational frequencies have only a minor dependence on the value of projections of the total and orbital electronic angular momentum (Ω and Λ) within the same atomic ion core configuration. The typical value of the vibrational frequency for the $5f^3 7s$ configuration is slightly underestimated by calculations (631 cm^{-1} predicted for the ^5I term vs. 649 cm^{-1} observed for X(1)4).

The second U^{2+} configuration that can be identified in the UF^+ PFI-ZEKE spectrum is $5f^3 6d\delta$. Only two levels with Ω=6 and 5 were identified at relatively high energies, with vibrational frequencies of 621 and 618 cm^{-1}. Due to the presence of an electron in the less polarizable 6d orbital, the vibrational frequencies were ~15 cm^{-1} lower than those of the $5f^3 7s$ states. The ab initio calculations predicted two states with Ω=6 and 5, with leading eigenvector contributions of 99.1% $5f^3 6d\delta$ (88.0% $^5L_6$, 10.6% $^5K_6$) for the 1(6) state and ~53% $5f^3 6d\delta$ (37.1 % $^5K_5$, 12.8% $^5I_5$, 2.5% $^5H_5$) and ~47% $5f^3 7s$ (17.5% $^5I_5$, 21.1% $^3I_5$, 5.3% $^3H_5$) for 2(5) state. The predicted energies are in good agreement with experimental observation. The vibrational frequency predicted for the $5f^3 6d\delta$ configuration state (^5L spin-free term) was 602 cm^{-1}, 19 cm^{-1} lower than the value observed for the (1)6 state. Hence, the underestimation of the vibrational frequencies for both the $5f^3 7s$ and $5f^3 6d\delta$ configurations was 18-19 cm^{-1}.

The 11 low-lying electronic states observed previously for UO[9] present energy level patterns that are very similar to those of the UF^+ Ω=4,3,2,1,0 and Ω=5,4,3,2,1,0 $5f^3 7s$ states. The energy separation between the (1)4 and (1)5 states of UO is close to that of UF^+, and to the $J_a = 4$ to 5 interval of U^{2+} $5f^3 7s$. The stronger ligand field of O^{2-} elevates the energies of the lowest Ω states in UO compared to UF^+. This behavior suggests that electrostatic ligand field interactions provide a good description of the electronic structure of the lowest excited states in UO and UF^+.

The (1)6 state of UO is observed at higher energy compared to UF^+. LFT calculations[10] indicate that this state is derived from the J_a=6 atomic level of the $5f^3 7s$ configuration. The $5f^3 6d\delta$ configuration in UO is destabilized by stronger ligand field of O^{2-} and most likely located at higher energies than in UF^+. The vibrational frequency could be used to determine whether the UO (1)6 state belongs to the $5f^3 6d\delta$ or the $5f^3 7s$ configuration. However, only the v=0 level was observed for that state. The predicted energies of the J_a=6 and 5 levels of U^{2+} are lower than the (1)6 state of UO but higher than (1)6 state of UF^+.

The (3)4, (3)3 and (3)2 states of UF^+, observed at 2593 cm^{-1}, 3060 cm^{-1} and 3316 cm^{-1}, were not predicted by our calculations. These levels form another series in which the energy increases with decreasing Ω. Therefore, it is likely that they belong to a common atomic U^{2+} core configuration. The spectral features associated with these levels were weak, and only v=0 band was observed for the (3)4 and (3)3 states. The v=0 and 1 levels were found for the (3)2 state yielding $\Delta G_{1/2}$=687 cm^{-1}. Based on the $\Delta G_{1/2}$ for (3)2, it seems unlikely that the (3)4, (3)3 and (3)2 states can be correlated with either the $5f^3(^4I)7s$ or $5f^3 6d\delta$ configurations. Another candidate is the $5f^2 7s^2$ configuration which also gives rise to a low-lying Ω=4 state in the isoelectronic UO molecule. For this configuration a 5f electron is promoted to the more polarizable 7s orbital, resulting in a U-F bond that is stiffer and shorter. The vibrational interval observed for the 3(2) state supports the assignment to the $5f^2 7s^2$ ion core. The (3)4 and (3)3 states can then be tentatively linked to the $5f^2 7s^2$ core based on the energy level pattern. Unfortunately, no theoretical predictions were made for the energies of $5f^2 7s^2$ levels. When such calculations were attempted at the CASSCF level, the $5f^2 7s^2$ triplets were found at very high energies (>10000 cm^{-1}) with more than 20 spin-free triplets of the $5f^3 7s$ configuration at lower energies. The presence of the low-lying $5f^3 7s$ triplets made the CASPT2 calculations of the $5f^2 7s^2$ states computationally impractical.

VII.7 CONCLUSIONS

Electronic spectra for UF and UF^+ show patterns of low-lying states that are consistent with the predictions of ligand field theory. The ground states of these molecules are shown to be X(1)4.5 and X(1)4, respectively. Comparisons of the electronic states of UF^+ and UO clearly illustrate qualitative similarities, with the greater field strength of the O^{2-} ligand producing a more pronounced electrostatic perturbation of the $U^{2+}(5f^37s)$ atomic ion core. Closely related patterns of states were also evident for $U^+(5f^37s^2)F^-$ and $U^{3+}(5f^3)O^{2-}$.

Relativistic ab initio calculations were used to predict the ground and low-lying states of UF and UF^+. The results were found to be in good agreement with both the experimental data and an ionic, ligand field theory model of the electronic structure. The level of agreement indicates that the U atom pseudo-potential of Dolg et al.[17] can yield good quantitative predictions in spin-orbit coupled calculations.

The observation that the energy level patterns for UF, UF^+, UO, and UO^+ are all consistent with LFT models indicates minimal participation of the 5f orbitals in the bonding for these species. However, this behavior does not necessarily imply that the 5f orbitals of U generally act as spectators. The cylindrical symmetry of a diatomic and the ligands F^- and O^{2-} restrict the options for 5f orbital participation in the bonding. Gas phase studies with more complex ligands are needed to systematically explore the conditions that favor covalent bonds that involve the 5f orbitals.

REFERENCES

(1) Barker, B. J.; Antonov, I. O.; Heaven, M. C.; Peterson, K. A. *J. Chem. Phys.* **2012**, *136*, 104305/1.

(2) Wang, F.; Le, A.; Steimle, T. C.; Heaven, M. C. *J. Chem. Phys.* **2011**, *134*, 031102/1.

(3) Heaven, M. C.; Gibson, J. K.; Marcalo, J. In *The chemistry of the actinide and transactinide elements*; Morss, L. R., Edelstein, N. M., Fuger, J., Eds.; Springer: 2010; Vol. 6, p 4079.

(4) Heaven, M. C.; Goncharov, V.; Steimle, T. C.; Ma, T.; Linton, C. *J. Chem. Phys.* **2006**, *125*, 204314/1.

(5) Heaven, M. C. *Phys. Chem. Chem. Phys.* **2006**, *8*, 4497.

(6) Goncharov, V.; Kaledin, L. A.; Heaven, M. C. *J. Chem. Phys.* **2006**, *125*, 133202/1.

(7) Goncharov, V.; Heaven, M. C. *J. Chem. Phys.* **2006**, *124*, 064312/1.

(8) Goncharov, V.; Han, J.; Kaledin, L. A.; Heaven, M. C. *J. Chem. Phys.* **2005**, *122*, 204311/1.

(9) Kaledin, L. A.; Heaven, M. C. *J. Mol. Spectrosc.* **1997**, *185*, 1.

(10) Kaledin, L. A.; McCord, J. E.; Heaven, M. C. *J. Mol. Spectrosc.* **1994**, *164*, 27.

(11) Dewberry, C. T.; Etchison, K. C.; Cooke, S. A. *Phys. Chem. Chem. Phys.* **2007**, *9*, 4895.

(12) Dewberry, C. T.; Etchison, K. C.; Grubbs, G. S.; Powoski, R. A.; Serafin, M. M.; Peebles, S. A.; Cooke, S. A. *Phys. Chem. Chem. Phys.* **2007**, *9*, 5897.

(13) Gagliardi, L.; Roos, B. O. *Nature (London, U. K.)* **2005**, *433*, 848.

(14) Gagliardi, L.; Roos, B. O. *Chem. Soc. Rev.* **2007**, *36*, 893.

(15) Hunt, R. D.; Thompson, C.; Hassanzadeh, P.; Andrews, L. *Inorg. Chem.* **1994**, *33*, 388.

(16) Liang, B.; Andrews, L.; Ismail, N.; Marsden, C. J. *Inorg. Chem.* **2002**, *41*, 2811.

(17) Dolg, M.; Cao, X. *J. Phys. Chem. A* **2009**, *113*, 12573.

(18) Cao, X.; Moritz, A.; Dolg, M. *Chem. Phys.* **2008**, *343*, 250.

(19) Cao, X.; Dolg, M. *Coord. Chem. Rev.* **2006**, *250*, 900.

(20) Tyagi, R., R. Tyagi, Ph.D. Thesis, Department of Chemistry, Ohio State University, 2005 (Advisor, R. M. Pitzer).

(21) Krauss, M.; Stevens, W. J. *Mol. Phys.* **2003**, *101*, 125.

(22) Fedorov, D. G.; Nakajima, T.; Hirao, K. *J. Chem. Phys.* **2003**, *118*, 4970.

(23) Krauss, M.; Stevens, W. J. *J. Comput. Chem.* **1983**, *4*, 127.

(24) Han, J.; Kaledin, L. A.; Goncharov, V.; Komissarov, A. V.; Heaven, M. C. *J. Am. Chem. Soc.* **2003**, *125*, 7176.

(25) Field, R. W. *Ber. Bunsenges. Phys. Chem.* **1982**, *86*, 771.

(26) Hunt, R. D.; Thompson, C.; Hassanzadeh, P.; Andrews, L. *Inorg. Chem.* **1994**, *33*, 388.

(27) Hildenbrand, D. L.; Lau, K. H. *J. Chem. Phys.* **1991**, *94*, 1420.

(28) Merritt, J. M.; Kaledin, A. L.; Bondybey, V. E.; Heaven, M. C. *Phys. Chem. Chem. Phys.* **2008**, *10*, 4006.

(29) Merritt, J. M.; Bondybey, V. E.; Heaven, M. C. *Phys. Chem. Chem. Phys.* **2008**, *10*, 5403.

(30) Salami, H.; Ross, A. J. *J. Mol. Spectrosc.* **2005**, *233*, 157.

(31) MOLPRO, version 2010, a package of ab initio programs, H.-J. Werner, P. J. Knowles, R. Lindh, F. R. Manby, M. Schütz, and others.

(32) Dunning, T. H., Jr. *J. Chem. Phys.* **1989**, *90*, 1007.

(33) Balasubramanian, K.; Siekhuas, W. J.; McLean, W. *J. Chem. Phys.* **2003**, *119*, 5889.

(34) R. J. Le Roy, LEVEL 8.0: *A Computer Program for Solving the Radial Schrödinger Equation for Bound and Quasibound Levels*, University of Waterloo Chemical Physics Research Report CP-663 (2007); see http://leroy.uwaterloo.ca/programs/.

(35) Ghigo, G.; Roos, B. O.; Malmqvist, P.-A. *Chem. Phys. Lett.* **2004**, *396*, 142.

(36) Blaise, J.; Wyart, J.-F. *International tables of selected constants* Paris, 1992; Vol. 20.

(37) Ruiperez, F.; Roos, B. O.; Barandiaran, Z.; Seijo, L. *Chem. Phys. Lett.* **2007**, *434*, 1.

(38) Steinhaus, D. W.; Radziemski, L. J., Jr.; Cowan, R. D.; Blaise, J.; Guelachvili, G.; Osman, Z. B.; Verges, J. *Present status of the analyses of the first and second spectra of uranium (U I and U II) as derived from measurements of optical spectra*, Los Alamos Sci. Lab., Los Alamos, NM, USA., 1971.

(39) Western, C. M. *PGOPHER, a program for simulating rotational structure,* University of Bristol 2007.

(40) Li, J.; Bursten, B. E.; Andrews, L.; Marsden, C. J. *J. Am. Chem. Soc.* **2004**, *126*, 3424.

(41) Li, J.; Bursten, B. E.; Liang, B.; Andrews, L. *Science* **2002**, *295*, 2242.

(42) Roos B. O.; Widmark, P.-O.; Gagliardi, L. *Faraday Discussions* **2003**, *124*, 57.

(43) Liang, B.; Andrews, L.; Li, J.; Bursten Bruce, E. *J. Am. Chem. Soc.* **2002**, *124*, 9016.

Table VII.1. Calculated energies and molecular constants for spin-free states of UF^+.

Term/configuration	T_e, cm^{-1} cas[a]	T_e, cm^{-1} rs2[b]	ω_e, cm^{-1} [a]	$\omega_e x_e$, cm^{-1} [a]	R_e, Å[a]
^5I / $5f^3 7s$	0	0	629.15	1.891	2.009
^5H / $5f^3 7s$	659.88	461.56	625.91	2.143	2.014
$^5\Gamma$ / $5f^3 7s$	943.23	661.71	623.01	1.895	2.018
$^5\Phi$ / $5f^3 7s$	1085.05	869.16	625.32	2.34	2.018
$^5\Delta$ / $5f^3 7s$	1190.24	977.56	622.95	1.889	2.016
$^5\Pi$ / $5f^3 7s$	1273.99	966.37	622.80	2.256	2.013
$^5\Sigma^-$ / $5f^3 7s$	1199.55	802.15	623.06	1.959	2.016
^5L / $5f^3 6d\delta$	1097.64	4575.95	601.90	1.850	2.027
^5K / $5f^3 6d\delta$	1793.14	5248.94	598.37	0.805	2.029
^5I / $5f^3 6d\delta$	2740.12	5514.37	596.81	1.807	2.034
^5H / $5f^3 6d\delta$	3575.66	6449.59	593.99	1.799	2.038
$^5\Gamma$ / $5f^3 6d\delta$	4214.00	6573.18	591.61	1.820	2.039
$^5\Phi$ / $5f^3 6d\delta$	4741.77	6810.77	589.43	1.827	2.040
$^5\Delta$ / $5f^3 6d\delta$	5240.81	7260.22	587.05	1.825	2.040
$^5\Pi$ / $5f^3 6d\delta$	5683.07	7401.85	584.59	1.814	2.040
$^5\Sigma^+$ / $5f^3 6d\delta$	5872.41	7558.85	583.19	1.803	2.040

[a] Potential energy curve (PEC) was calculated at the CASSCF level and the radial Schrödinger equation was solved to obtain T_e, ω_e and $\omega_e x_e$. Each PEC was fitted to a Morse potential $U(r)= T_e+D_e(1-\exp(-\alpha(R-R_e)))^2$ to obtain R_e.

[b] Single-point calculations at R=2.00 Å.

Table VII.2. Comparison of experimental and theoretical excitation energies for low-lying electronic states of UF^+, UO and U^{2+}.

State	UF^+, theory[a]	UF^+, exp.[b]	UO, exp.[c]	U^{2+}, exp.[d]	U^{2+}, theory	U^{2+} levels
(1)4	0	0	0			
(1)3	494.36	511.794	651.13			
(1)2	725.86	739.42	958.66	0	0	$^5I_4$
(1)1	813.66	777.806	[1181.3]			
(1)0	802.16	773.83	[1253.7]			
(1)5	1100.47	1005.67	1043.00			
(2)4	1575.29	1509.10	1574.09			
(2)3	1855.29	1835.32	1941.48	974	973.55	$^5I_5$
(2)2	1891.47	1779.14	[2118.8]			
(2)1	1830.86	1804.26	[2235.0]			
(2)0	1820.26	1784.30	[2272.0]			
(1)6	2929.37	2618.52	4469.00	-	3638.56	$^5I_6$
(1)5	3510.60	3329.44	[4595.4]	-	3915.47	$^5I_5$
(3)4	-	2593.30	294.12			
(3)3	-	3059.52	-	-	-	-
(3)2	-	3316.44	-			

[a] Single-point calculations at R=2.00 Å.
[b] T_e values obtained by fitting the experimental T_v values to the anharmonic oscillator expression
[c] Data from Kaledin et al.[9], the values are T_0, the values in brackets were predicted by LFT
[d] Data from Blaise et al.[36]

Table VII.3. Comparison of experimental and theoretical excitation energies of low-lying electronic states of UF, UO^+ and U^+ and U^{3+}.

State	UF, calc. this work[a]	UF, theory[b]	UF, exp. this work	UO^+, exp.[c]	U^{3+}, calc.[d]	U^+, exp.[e]	U^+ levels
(1)4.5	0	0	0	0	0	0	$^4I_{4.5}$
(1)3.5	415	61	435	764.93			
(1)2.5	678	805	650	1132.42			
(1)1.5	824	944	-	1284.50			
(1)0.5	790	794	-	1324.9			
(1)5.5	3060	3801	-	4177.83	4990	4420.870	$^4I_{5.5}$
(2)4.5	3379	3942	-	4758.46			
(2)3.5	3623	4317	-	5161.96			
(2)2.5	3753	4484	-	5219.37			
(2)1.5	3780	4548	-	-			
(2)0.5	3874	4526	-	-			
(2)5.5[f]	4755	7357	-	-	-	289.040	$^6L_{5.5}$
(3)4.5[f]	5347	7732	-	-			
(1)6.5	6639	7747	-	-	9415	8276.733	$^4I_{6.5}$
(3)5.5	6907	7807	-	-			
(4)4.5	7125	8149	-	-			
(3)3.5	7275	8248	-	-			
(3)0.5	7460	8197	-	-			
(4)3.5[f]	6135	8248	-	-	-	289.040	$^6L_{5.5}$

[a] Single-point calculations at R=2.00 Å.
[b] Data from Fedorov et al.[22]
[c] Data from Goncharov et al.[6]
[d] Data from Ruiperez et al.[37]
[e] Data from Steinhaus et al.[38]
[f] These states belong to $5f^3 7s6d\delta$ ion core

Table VII.4. Energies and molecular constants for the ground and excited states of UF.

Level	T_0, cm^{-1}	B, cm^{-1}	R_0, Å
X(1)4.5	0	0.2348(2)	2.020(1)
[18.6]3.5	18632.4(1)	0.2293(2)	2.044(1)
[19.9]5.5	19941.0(1)	0.239(1)	2.002(5)

Table VII.5. Spectroscopy parameters of the ground and low-lying excited states of UF^+. The value in brackets is $\Delta G_{1/2}$.

State	v+	$T_{e,v+}$, cm^{-1}	B^+, cm^{-1}	ω_e (cm^{-1})	$\omega_e x_e$ (cm^{-1})
X 1(4)	0	0	0.250(3)	649.92(35)	1.831(49)
	1	646.10	0.247(3)		
	2	1289.34	0.244(5)		
	3	1928.00	0.241(17)		
	4	2563.00	0.234(17)		
	5	3194.16	0.248(27)		
	6	3823.06	0.244(27)		
1(3)	0	510.78	0.243(7)	648.26(62)	2.01(12)
	1	1155.63	0.27(4)		
	2	1795.46	0.238(3)		
	3	2431.26	0.246(3)		
	4	3063.92	0.237(22)		
1(2)	0	737.53	0.224(1)	646.32(28)	1.859(46)
	1	1380.51	0.221(2)		
	2	2019.13	0.221(4)		
	3	2654.43	0.221(1)		
	4	3285.43	0.222(25)		
	5	3913.69	-		
1(1)	0	776.12	0.241(2)	646.39(37)	1.928(90)
	1	1418.49	0.240(4)		
	2	2057.41	0.228(3)		
	3	2692.07	0.245(7)		
1(0)	0	771.81	-	646.11(55)	1.77(11)

	1	1414.98	-		
	2	2053.50	-		
	3	2688.80	-		
	4	3321.20	-		
1(5)	0	1005.62	0.256(18)	649.53(25)	1.710(41)
	1	1651.45	0.244(14)		
	2	2294.55	0.248(14)		
	3	2933.75	0.238(10)		
	4	3569.20	0.245(23)		
	5	4202.01	0.243(16)		
2(4)	0	1508.70	0.247(2)	648.64(68)	1.75(13)
	1	2153.20	0.242(2)		
	2	2795.80	0.233(2)		
	3	3433.36	0.252(19)		
	4	4068.16	-		
2(3)	0	1833.36	0.273(2)	645.7(5)	1.45(10)
	1	2476.16	0.262(3)		
	2	3116.06	0.242(20)		
2(2)	0	1777.83	0.254(12)	647.2(5)	1.85(10)
	1	2421.33	0.267(17)		
	2	3061.13	-		
2(1)	0	1804.91	0.249(5)	651.77(57)	3.41(14)
	1	2448.01	0.233(3)		
	2	3086.31	-		
	3	3719.17	0.227(4)		

2(0)	0	1784.30	-	-	-
3(4)	0	2593.30	0.239(2)	-	-
1(6)	0	2604.31	0.240(20)	621.05(5)	1.17(10)
	1	3223.27	0.241(20)		
	2	3839.37	0.236(20)		
3(3)	0	3059.52	0.233(53)	-	-
3(2)	0	3301.03	0.235(25)	[687]	-
	1	3987.56	0.238(9)		
2(5)	0	3313.51	0.241(23)	[618]	-
	1	3931.31	0.249(23)		

Figure VII.1. Laser induced fluorescence spectrum of the [18.6]3.5-X(1)4.5 transition of UF. The black trace is the experimental data and the red trace (inverted) is a computational simulation. The rotational temperature was set to 9K.

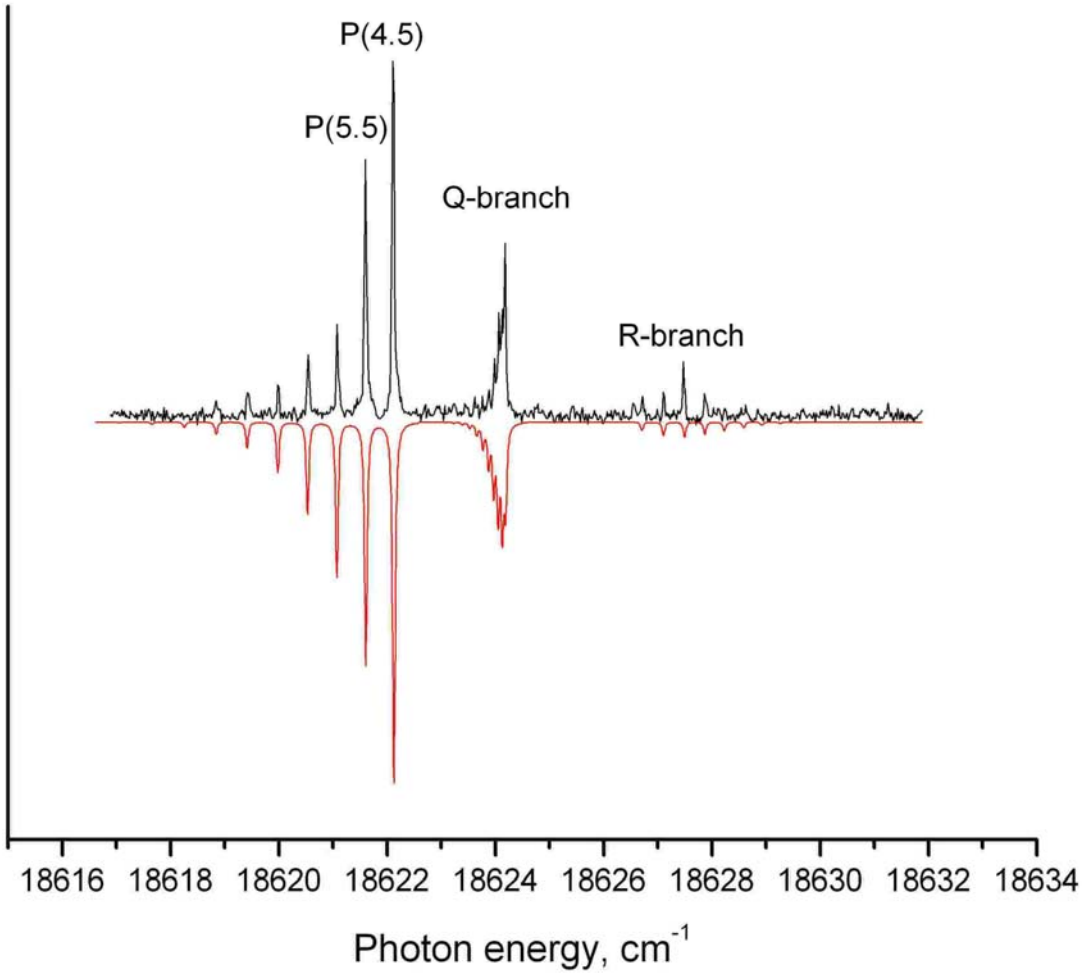

Figure VII.2. 1+1′ REMPI spectrum of the [19.9]5.5- X(1)4.5 transition of UF. The red trace is the experimental data, and the inverted red trace is computational simulation. The blue trace shows the overlapping [19.950]4-X(1)4 transition of UO.

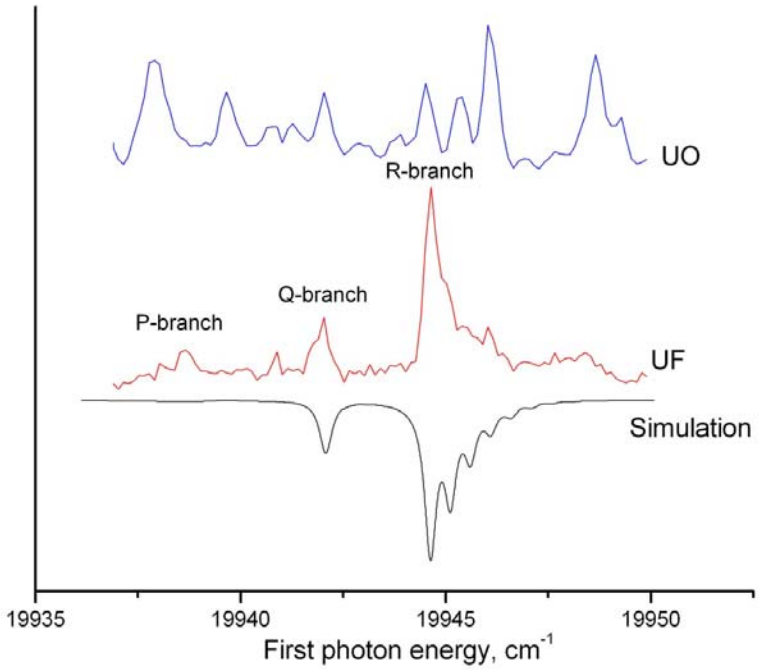

Figure VII.3. Dispersed fluorescence spectrum taken by exciting the Q-branch of the UF [18.6]3.5-X(1)4.5 band at 18624 cm^{-1}.

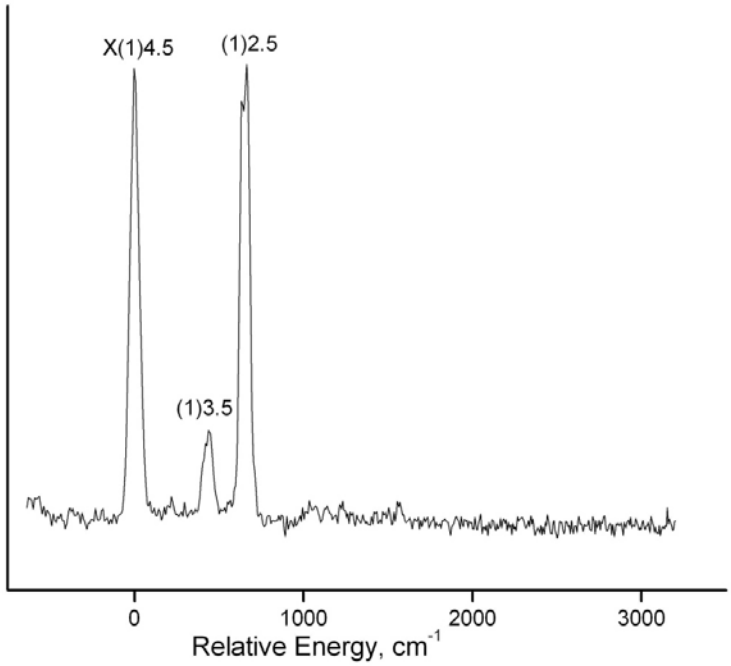

Figure VII.4. Low resolution PFI-ZEKE survey scan of UF^+. The horizontal axis is the sum of the energies of two photons.

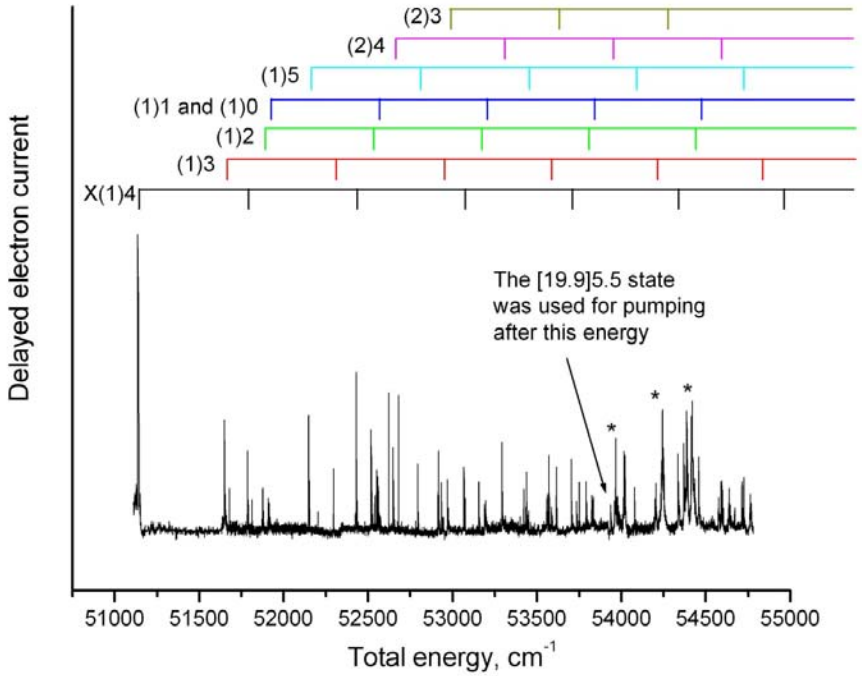

Figure VII.5. Rotationally resolved PFI-ZEKE scan of the UF^+ origin band. The upper trace was taken with the first laser tuned to the P(4.5) line of the [18.6]3.5-X(1)4.5 transition of UF, and the lower trace with excitation of the P(5.5) line. The horizontal axis is the sum of the energies of two photons and the rotational energy in the ground state of UF.

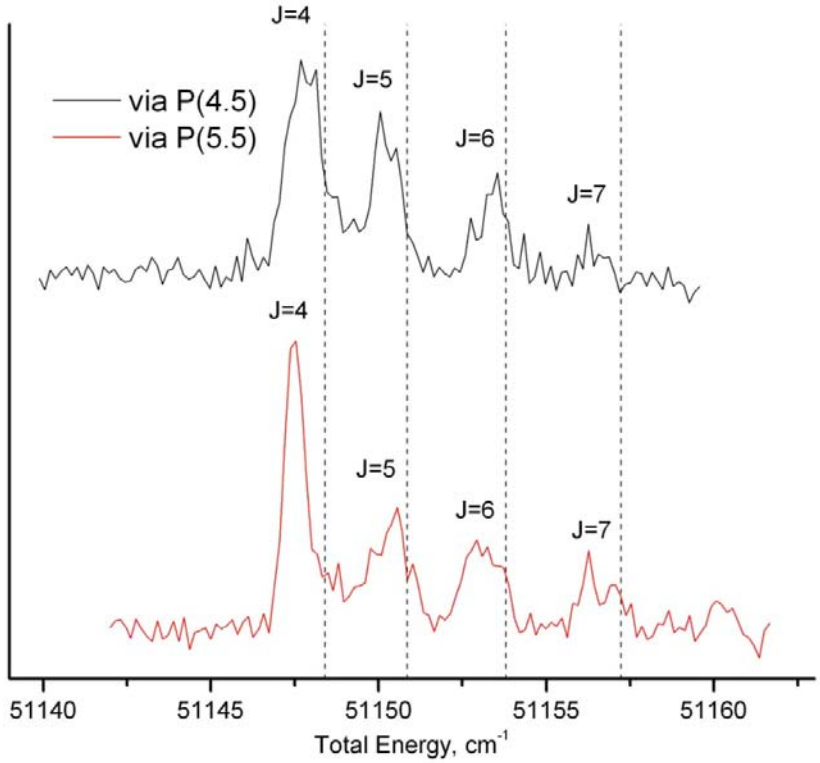

Figure VII.6. Rotationally resolved PFI-ZEKE scan of the UF^+ (1)1 and (1)0 bands. The upper trace is the experimental data and the inverted lower trace is a computational simulation. Only the (1)1 band is simulated. The values $\Omega''=4$ and $\Omega'=1$ are assumed for the initial and final states. Only the J=4 level is populated in the initial state and all $\Delta J<|6|$ are allowed. Note the large Ω-doubling of rotational levels of (1)1 state.

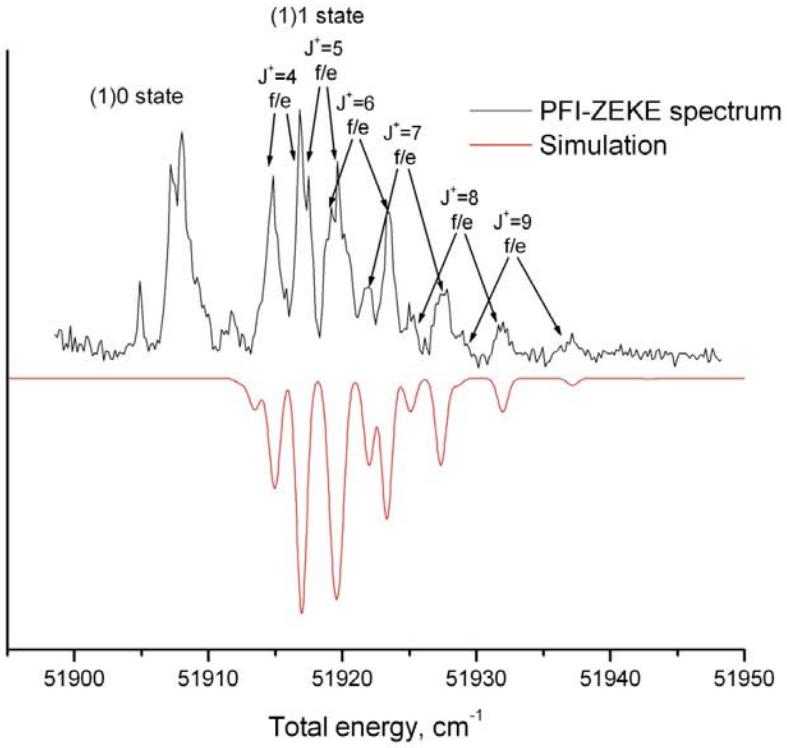

Figure VII.7. Energy level diagram of UF^+ and UO electronic states. The black circles are the UF^+ experimental data, red circles are the calculated energies and the blue circles are UO experimental data. The half-filled circles on the right-hand side are the calculated energies of the lowest levels of the U^{2+} f^3s configuration relative to the lowest f^3s J_a=4 level.

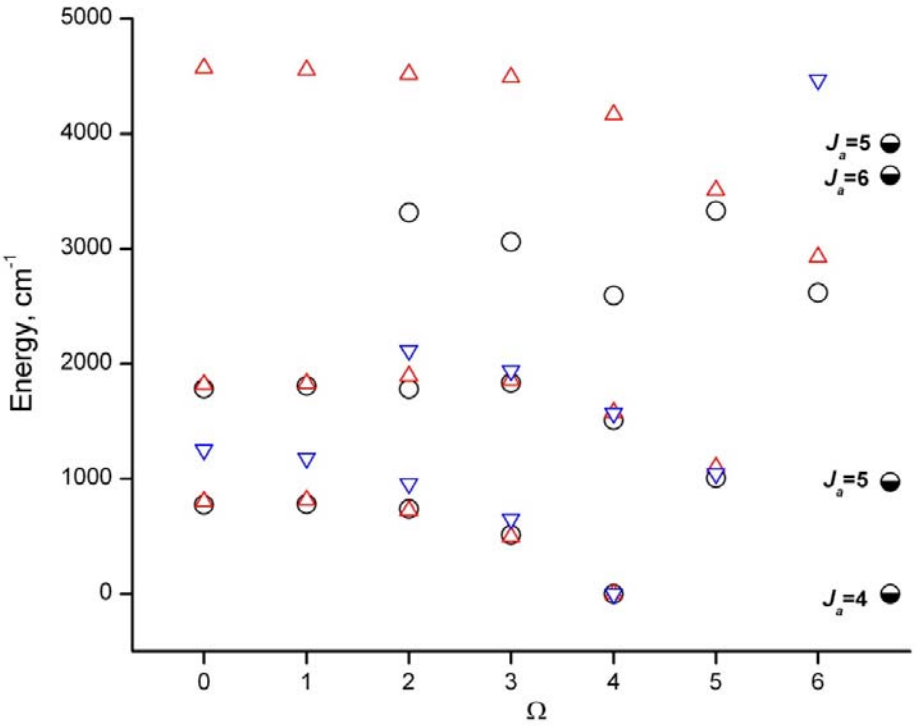

Figure VII.8. Isodensity surfaces D=0.02 of *7s* and *5fδ* orbitals of UF+ calculated at CASSCF level.

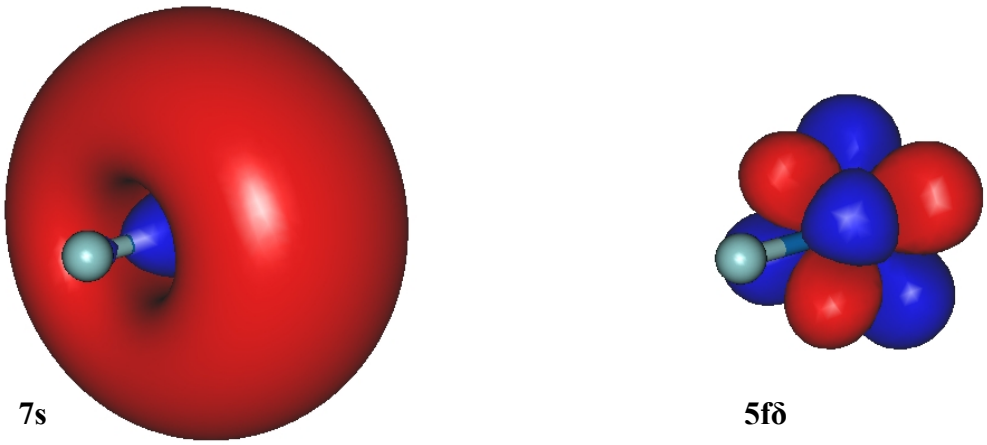

7s **5fδ**

APPENDIX

SUPPLEMENTARY MATERIALS ON BeC CALCULATIONS

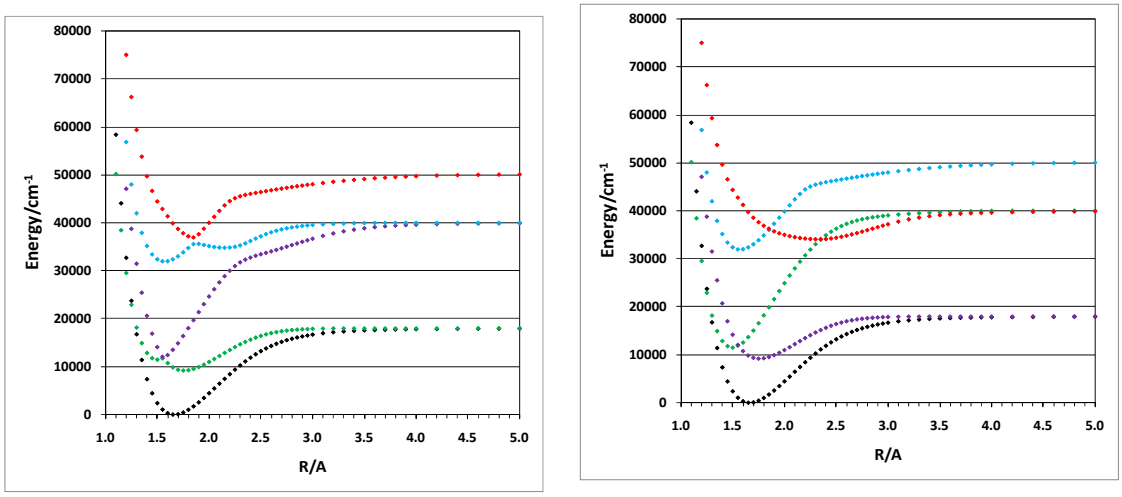

Figure App. 1. Electronic states of BeC plotted in adiabatic (on left) and diabatic (on right) representations. The zero of energy is the minimum of the $X^3\Sigma^-$ ground state (black), with the four lowest $^3\Pi$ states appearing above (in color).

The diabatic potential energy curves and coupling matrix elements were reconstructed from the n=1-4 adiabats. At each internuclear distance, the inverse eigenvalue problem was solved for a four-coupled-state model including couplings only between neighboring states. Diabatic coupling strengths were set to one-half of the minimum gaps between adiabatic curves. Based on calculated derivative couplings (Molpro), Gaussian coupling profiles were used. The minimum energy gaps are ΔE= 425.97, 3376.84, and 1317.08 cm^{-1} for the interactions between the 1-2, 2-3, and 3-4 states, respectively. The locations of those minimum gaps were R_x= 1.5545, 2.3576, and 1.8550 Angstroms. The matrix elements coupling these states (α) were defined by the expression

$$\alpha = \frac{\Delta E}{2}\mathrm{Exp}\left(-0.95\left(R - R_x\right)^2\right)$$

Vibronic energies were calculated were calculated for the system of the four coupled $^3\Pi$ states. It can be appreciated from Figure 1 that with a four-state model, even vibronic states with dominant $3^3\Pi$and $4^3\Pi$ character couple to the continuum through the chain of couplings. Therefore an optimized complex absorbing potential (CAP) was used and the vibronic state solutions were obtained by diagonalizing the resulting complex-symmetric Hamiltonian. The real part of each eigenvalue gives the vibronic energy, while the complex part defines the width.

Table App. 1. Calculated $^3\Pi$state vibronic levels (cm^{-1}) for the four-pi-state diabatization model, with percent character from each diabatic state and expectation value of the coordinate R. Widths $\Gamma(cm^{-1})$ for each level were determined using individually optimized Complex Absorbing Potentials (CAP).

level	E(n)	E(n)-ZPE(GS)	% 1-pi	% 2-pi	% 3-pi	% 4-pi	< R >	$(<1/R^2>)^{-}_{1/2}$	Γ
1	9459.12	8992.32	99.622	0.376	0.000	0.003	1.76822	1.76458	
2	10216.78	9749.98	99.349	0.647	0.000	0.004	1.79038	1.77928	
3	10947.18	10480.38	98.314	1.679	0.000	0.007	1.80994	1.79070	
4	11620.72	11153.92	83.974	15.973	0.000	0.053	1.78293	1.74904	
5	11916.46	11449.67	24.882	74.902	0.001	0.216	1.59394	1.56669	
6	12389.79	11922.99	91.492	8.487	0.000	0.021	1.83950	1.79708	
7	13018.77	12551.97	81.812	18.137	0.000	0.052	1.83350	1.77703	
8	13235.09	12768.29	21.201	78.504	0.001	0.294	1.59490	1.56829	
9	13693.44	13226.64	96.567	3.413	0.000	0.020	1.90876	1.85581	
10	14246.25	13779.45	63.079	36.769	0.001	0.151	1.80147	1.72827	
11	14444.97	13978.18	42.302	57.466	0.001	0.231	1.72048	1.65295	
12	14931.41	14464.61	96.648	3.333	0.000	0.019	1.98027	1.90693	
13	15457.51	14990.72	78.524	21.345	0.001	0.131	1.91908	1.82863	
14	15577.85	15111.05	24.567	75.069	0.002	0.362	1.68148	1.61409	
15	16016.95	15550.15	97.140	2.852	0.000	0.009	2.07199	1.97418	
16	16498.85	16032.06	98.748	1.248	0.000	0.004	2.13365	2.02565	
17	16729.54	16262.74	2.803	96.592	0.003	0.602	1.56915	1.54503	
18	16934.61	16467.82	98.650	1.347	0.000	0.003	2.20607	2.08265	
19	17314.18	16847.39	98.726	1.271	0.000	0.003	2.30021	2.15985	
20	17623.94	17157.15	98.043	1.950	0.000	0.007	2.43578	2.27210	
21	17838.01	17371.21	86.126	13.788	0.000	0.085	2.57165	2.30144	
22	17889.40	17422.60	28.986	70.480	0.003	0.531	2.03410	1.73913	0.00277
23	17900.60	17433.80	92.521	7.420	0.000	0.058	3.78253	3.25350	0.148
24	17924.57	17457.78	98.060	1.923	0.000	0.017	4.01547	3.62627	1.45
25	19005.33	18538.53	63.592	36.089	0.002	0.317	3.10332	2.21522	37.4
26	20089.62	19622.82	64.175	35.449	0.002	0.373	3.07693	2.21736	52.0
27	21147.18	20680.38	59.611	39.872	0.003	0.514	3.04956	2.15531	49.8
28	22183.21	21716.42	45.940	53.198	0.005	0.857	2.69676	1.96865	37.0
29	23197.13	22730.34	28.771	69.801	0.009	1.419	2.26763	1.80251	22.4
30	24186.35	23719.55	14.536	83.298	0.014	2.152	1.96205	1.70655	10.6
31	25147.02	24680.22	5.648	91.312	0.020	3.021	1.79850	1.66525	3.47
32	26074.98	25608.19	1.843	94.107	0.026	4.024	1.74833	1.66047	0.362
33	26968.97	26502.17	1.605	93.148	0.033	5.215	1.77193	1.67857	0.237
34	27822.58	27355.78	3.373	89.888	0.041	6.698	1.83852	1.71091	1.93
35	28631.61	28164.81	5.801	85.502	0.052	8.645	1.92122	1.75102	4.43
36	29389.98	28923.18	7.968	80.674	0.065	11.293	2.00143	1.79479	6.99
37	30090.83	29624.03	9.549	75.512	0.082	14.857	2.07724	1.84195	8.97
38	30728.47	30261.67	10.464	70.132	0.101	19.303	2.14867	1.89202	10.2
39	31304.40	30837.60	10.703	65.178	0.118	24.001	2.20358	1.93808	10.8
40	31831.71	31364.92	10.783	60.965	0.129	28.123	2.25098	1.97767	11.3
41	32280.27	31813.47	0.000	0.020	98.309	1.672	1.58371	1.58058	0.00000492
42	32323.75	31856.96	10.798	57.804	0.133	31.265	2.29224	2.01111	11.6
43	32791.98	32325.18	11.124	55.277	0.132	33.467	2.34047	2.04151	11.8
44	33242.89	32776.10	10.977	53.620	0.129	35.274	2.36643	2.06324	12.2
45	33261.05	32794.26	0.000	0.042	97.303	2.654	1.60321	1.59368	0.00000301
46	33681.37	33214.58	10.919	52.233	0.125	36.723	2.39749	2.08523	12.3
47	34107.62	33640.83	10.811	51.179	0.121	37.889	2.42624	2.10516	12.3

48	34208.49	33741.69	0.000	0.103	95.095	4.802	1.62659	1.61025	0.000000204
49	34524.23	34057.44	10.606	50.306	0.116	38.972	2.45407	2.12507	12.2
50	34930.92	34464.13	10.307	49.718	0.110	39.864	2.47829	2.14292	12.1
51	35092.21	34625.41	0.000	0.404	87.296	12.300	1.66782	1.64278	0.000000143
52	35327.67	34860.88	9.972	49.141	0.105	40.782	2.50616	2.16343	11.7
53	35662.19	35195.40	0.001	5.989	29.523	64.487	1.91169	1.87883	0.0000601
54	35714.53	35247.73	10.000	48.529	0.100	41.371	2.54840	2.18770	11.4
55	35964.93	35498.13	0.001	7.094	47.274	45.631	1.86295	1.80602	0.000000567
56	36090.74	35623.95	9.271	48.382	0.095	42.252	2.56592	2.20607	11.0
57	36362.82	35896.02	0.002	11.113	35.618	53.267	1.92750	1.86434	0.0000763
58	36456.01	35989.22	8.708	48.183	0.090	43.019	2.59382	2.22886	10.5
59	36803.50	36336.71	0.083	13.858	36.922	49.138	1.94291	1.86558	0.0926
60	36809.56	36342.77	8.276	47.709	0.379	43.636	2.62582	2.25113	9.95
61	37150.45	36683.65	7.917	47.866	0.096	44.121	2.66991	2.28337	9.49
62	37237.90	36771.11	0.007	15.775	39.629	44.589	1.94410	1.85864	0.00542
63	37478.34	37011.55	7.360	47.904	0.075	44.660	2.70875	2.31393	8.93
64	37680.53	37213.74	0.009	19.199	34.889	45.902	1.98201	1.88971	0.00746
65	37792.15	37325.35	6.909	47.940	0.077	45.074	2.75546	2.34873	8.34
66	38090.84	37624.04	6.329	48.020	0.158	45.494	2.80144	2.38454	7.72
67	38135.35	37668.55	0.029	22.679	30.289	47.003	2.02201	1.92166	0.0250
68	38373.84	37907.05	5.921	48.167	0.060	45.853	2.86366	2.43131	7.11
69	38374.37	37907.57	0.000	0.948	43.438	55.614	1.80160	1.78888	0.000000095
70	38585.37	38118.57	0.005	26.066	27.481	46.448	2.05560	1.94756	0.00246
71	38639.72	38172.93	5.321	48.175	0.057	46.447	2.92483	2.48061	6.53
72	38887.37	38420.57	4.852	47.798	0.049	47.301	3.00017	2.53947	5.91
73	39022.38	38555.59	0.003	29.671	27.054	43.271	2.09435	1.97187	0.000626
74	39115.33	38648.53	4.344	46.883	0.046	48.727	3.08697	2.60904	5.30
75	39321.83	38855.03	3.803	45.240	0.043	50.915	3.19128	2.69455	4.64
76	39394.26	38927.47	0.001	11.653	54.935	33.410	1.88750	1.80458	0.000407
77	39465.96	38999.16	0.002	23.602	16.606	59.790	2.07174	1.99187	0.0000418

Table App. 2. Vibrational levels on $X^3\Sigma^-$ ground electronic state. Results include ^{12}C and ^{13}C isotopomers and show the effect of relativistic and Davidson corrections on the levels.

$Be^{12}C$

v	No Davidson				Davidson			
	No relativistic		Relativistic		No relativistic		Relativistic	
	E(v)	E(v)-E(0)	E(v)	E(v)-E(0)	E(v)	E(v)-E(0)	E(v)	E(v)-E(0)
0	466.86	0.00	466.79	0.00	466.65	0.00	466.58	0.00
1	1386.37	919.50	1386.16	919.37	1385.35	918.71	1385.16	918.58
2	2287.16	1820.30	2286.85	1820.05	2284.61	1817.96	2284.31	1817.73
3	3170.08	2703.22	3169.71	2702.91	3164.68	2698.03	3164.32	2697.74
4	4036.01	3569.15	4035.53	3568.73	4026.01	3559.37	4025.56	3558.97
5	4884.31	4417.45	4883.48	4416.68	4869.02	4402.37	4868.21	4401.63
6	5713.71	5246.85	5712.39	5245.60	5693.72	5227.07	5692.42	5225.84
7	6524.64	6057.77	6522.94	6056.15	6499.92	6033.28	6498.25	6031.67
8	7316.94	6850.07	7314.83	6848.04	7287.54	6820.89	7285.45	6818.87
9	8090.20	7623.33	8087.60	7620.80	8056.32	7589.68	8053.74	7587.16
10	8843.88	8377.02	8840.79	8374.00	8805.85	8339.21	8802.78	8336.20
11	9577.39	9110.52	9573.73	9106.93	9535.68	9069.03	9532.03	9065.45
12	10289.91	9823.05	10285.65	9818.86	10245.14	9778.50	10240.90	9774.31
13	10980.55	10513.69	10975.63	10508.83	10933.52	10466.87	10928.61	10462.02
14	11648.19	11181.33	11642.54	11175.75	11599.90	11133.25	11594.27	11127.69
15	12291.56	11824.69	12285.12	11818.32	12243.25	11776.60	12236.84	11770.26
16	12909.16	12442.30	12901.87	12435.08	12862.36	12395.71	12855.12	12388.54
17	13499.35	13032.49	13491.14	13024.35	13455.90	12989.25	13447.77	12981.19
18	14060.28	13593.42	14051.08	13584.29	14022.38	13555.73	14013.31	13546.73
19	14589.98	14123.12	14579.74	14112.94	14560.20	14093.55	14550.14	14083.55
20	15086.42	14619.55	15075.07	14608.28	15067.68	14601.03	15056.59	14590.01
21	15547.54	15080.67	15535.05	15068.25	15543.13	15076.48	15530.97	15064.39
22	15971.35	15504.49	15957.68	15490.88	15984.83	15518.18	15971.58	15504.99
23	16355.96	15889.09	16341.07	15874.28	16391.10	15924.45	16376.73	15910.15
24	16699.60	16232.74	16683.50	16216.71	16760.31	16293.67	16744.83	16278.24
25	17000.80	16533.94	16983.49	16516.70	17090.96	16624.31	17074.35	16607.77
26	17258.46	16791.59	17239.97	16773.17	17381.71	16915.07	17364.01	16897.43
27	17472.12	17005.25	17452.50	16985.70	17631.62	17164.97	17612.84	17146.26
28	17642.34	17175.48	17621.67	17154.87	17840.26	17373.61	17820.45	17353.87
29	17771.08	17304.22	17749.47	17282.67	18008.04	17541.40	17987.28	17520.70
30	17862.18	17395.32	17839.78	17372.99	18136.56	17669.92	18114.93	17648.35
31	17922.20	17455.34	17899.22	17432.43	18229.06	17762.41	18206.69	17740.11
32	17960.20	17493.34	17936.86	17470.06	18291.29	17824.65	18268.37	17801.78
33					18331.44	17864.79	18308.15	17841.57
De	17990.83		17966.82		18368.02		18344.04	
D_0	17523.96		17500.02		17901.37		17877.45	

$Be^{13}C$

v	No Davidson				Davidson			
	No relativistic		Relativistic		No relativistic		Relativistic	
	E(v)	E(v)-E(0)	E(v)	E(v)-E(0)	E(v)	E(v)-E(0)	E(v)	E(v)-E(0)
0	459.11	0.00	459.05	0.00	458.90	0.00	458.84	0.00
1	1363.58	904.47	1363.38	904.34	1362.60	903.70	1362.41	903.57
2	2249.94	1790.83	2249.63	1790.59	2247.48	1788.58	2247.18	1788.35
3	3118.98	2659.87	3118.61	2659.57	3113.80	2654.90	3113.45	2654.61
4	3971.59	3512.48	3971.12	3512.08	3961.98	3503.07	3961.53	3502.70
5	4807.24	4348.13	4806.45	4347.41	4792.42	4333.51	4791.65	4332.81
6	5624.65	5165.54	5623.38	5164.34	5605.16	5146.26	5603.92	5145.08
7	6424.16	5965.05	6422.51	5963.47	6400.05	5941.14	6398.42	5939.58
8	7205.72	6746.60	7203.68	6744.64	7176.97	6718.06	7174.95	6716.11
9	7968.91	7509.80	7966.39	7507.34	7935.73	7476.83	7933.23	7474.39
10	8713.28	8254.17	8710.28	8251.24	8675.94	8217.04	8672.96	8214.12
11	9438.23	8979.12	9434.69	8975.64	9397.19	8938.29	9393.66	8934.82
12	10143.08	9683.96	10138.95	9679.91	10098.88	9639.98	10094.77	9635.93
13	10826.95	10367.84	10822.18	10363.13	10780.35	10321.44	10775.59	10316.75
14	11488.84	11029.73	11483.37	11024.33	11440.75	10981.85	11435.30	10976.46
15	12127.58	11668.46	12121.35	11662.30	12079.14	11620.23	12072.93	11614.10
16	12741.79	12282.68	12734.74	12275.70	12694.41	12235.50	12687.40	12228.56
17	13329.96	12870.85	13322.03	12862.98	13285.32	12826.42	13277.46	12818.62
18	13890.37	13431.26	13881.49	13422.44	13850.50	13391.60	13841.73	13382.89
19	14421.19	13962.08	14411.29	13952.25	14388.46	13929.55	14378.72	13919.89
20	14920.48	14461.37	14909.52	14450.48	14897.61	14438.71	14886.88	14428.04
21	15386.30	14927.19	15374.23	14915.19	15376.36	14917.46	15364.59	14905.75
22	15816.74	15357.63	15803.51	15344.47	15823.07	15364.17	15810.23	15351.39
23	16209.94	15750.82	16195.53	15736.48	16236.13	15777.22	16222.20	15763.36
24	16564.17	16105.06	16548.57	16089.52	16613.96	16155.06	16598.93	16140.09
25	16877.91	16418.80	16861.11	16402.07	16955.08	16496.17	16938.94	16480.11
26	17149.94	16690.83	17131.97	16672.92	17258.14	16799.23	17240.92	16782.08
27	17379.53	16920.41	17360.42	16901.37	17522.06	17063.16	17503.77	17044.93
28	17566.72	17107.60	17546.53	17087.49	17746.18	17287.28	17726.86	17268.02
29	17712.70	17253.58	17691.53	17232.48	17930.49	17471.58	17910.18	17451.35
30	17820.18	17361.07	17798.16	17339.11	18075.90	17617.00	18054.70	17595.86
31	17894.00	17434.89	17871.30	17412.25	18184.64	17725.74	18162.64	17703.81
32	17941.73	17482.61	17918.55	17459.50	18260.83	17801.93	18238.18	17779.34
33	17972.92	17513.81	17949.52	17490.48	18311.18	17852.28	18288.07	17829.23
34					18344.37	17885.47	18321.01	17862.17
De	17990.83		17966.82		18368.02		18344.04	
D_0	17531.71		17507.77		17909.11		17885.20	

Figure App. 2. Four lowest $^3\Pi$states (at left) shown previously. Lowest four $^3\Sigma^-$ states (at right) including ground state.

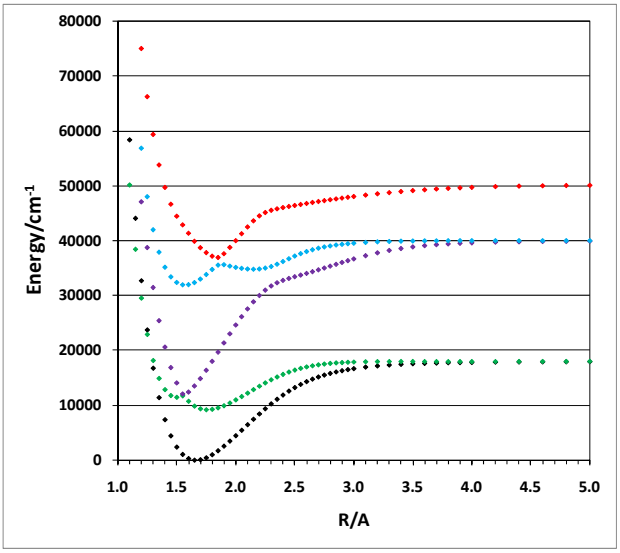

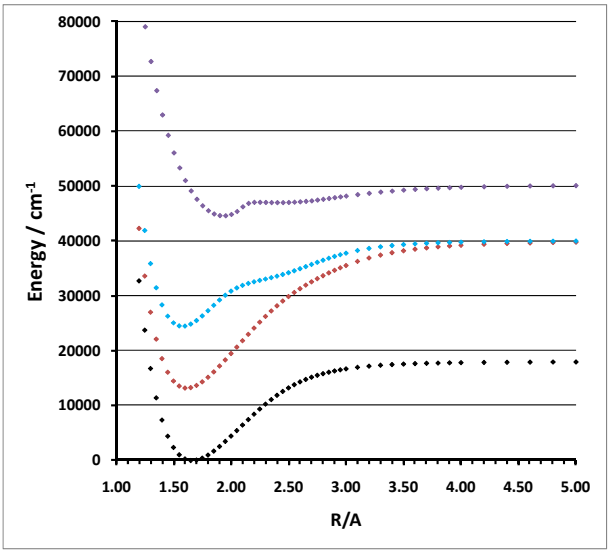

Table App. 3. Calculated $2^3\Sigma^-$ state (plotted in red in Figure 1 at right) vibrational levels (cm^{-1}) using adiabatic PEC.

level	E(n)	$E(n)-E_{GS}(1)$	<R>	$(<1/R^2>)^{-1/2}$	FC
1	13660.96	13194.17	1.6238	1.6208	0.8408
2	14660.43	14193.63	1.6408	1.6317	0.1511
3	15640.99	15174.2	1.6580	1.6427	0.0079
4	16603.65	16136.86	1.6754	1.6538	1.26E-04
5	17547.24	17080.45	1.6936	1.6656	6.51E-07
6	18470.55	18003.76	1.7120	1.6774	6.74E-09
7	19375.83	18909.04	1.7304	1.6892	1.92E-09
8	20262.88	19796.09	1.7494	1.7014	2.96E-09
9	21131.77	20664.98	1.7685	1.7136	1.05E-10
10	21982.97	21516.18	1.7881	1.7260	1.02E-09
11	22816.19	22349.39	1.8079	1.7387	7.57E-11
12	23631.26	23164.47	1.8283	1.7517	3.08E-10
13	24427.78	23960.98	1.8494	1.7651	1.16E-10
14	25205.48	24738.68	1.8709	1.7787	4.90E-11
15	25963.84	25497.04	1.8928	1.7924	1.15E-10
16	26702.28	26235.48	1.9153	1.8065	2.40E-12
17	27420.67	26953.87	1.9392	1.8217	4.22E-11
18	28119.13	27652.34	1.9644	1.8380	3.60E-11
19	28797.33	28330.54	1.9908	1.8553	5.80E-14
20	29454.71	28987.92	2.0184	1.8735	1.78E-11
21	30090.82	29624.03	2.0474	1.8928	1.84E-11
22	30705.6	30238.8	2.0783	1.9140	1.54E-12
23	31299.53	30832.73	2.1114	1.9376	3.60E-12
24	31873.49	31406.69	2.1468	1.9638	9.86E-12
25	32428.45	31961.65	2.1840	1.9923	5.48E-12
26	32965.36	32498.57	2.2227	2.0225	2.84E-13
27	33485.14	33018.35	2.2619	2.0535	1.27E-12
28	33988.77	33521.97	2.3013	2.0847	3.90E-12
29	34476.38	34009.58	2.3423	2.1172	3.64E-12
30	34946.65	34479.85	2.3857	2.1516	1.48E-12
31	35399.2	34932.4	2.4295	2.1860	9.20E-14
32	35834.29	35367.49	2.4756	2.2220	2.55E-13
33	36250.56	35783.77	2.5244	2.2602	1.05E-12
34	36647.77	36180.98	2.5761	2.3005	1.46E-12
35	37024.64	36557.85	2.6320	2.3444	1.25E-12
36	37380.52	36913.72	2.6926	2.3922	7.29E-13
37	37714.16	37247.37	2.7589	2.4448	2.64E-13
38	38024.78	37557.99	2.8323	2.5037	3.20E-14
39	38311.43	37844.63	2.9135	2.5694	1.00E-14
40	38573.31	38106.51	3.0044	2.6439	9.00E-14
41	38809.95	38343.15	3.1067	2.7288	1.81E-13
42	39021.06	38554.26	3.2221	2.8258	2.36E-13
43	39206.77	38739.98	3.3528	2.9370	2.47E-13
44	39367.67	38900.88	3.5013	3.0648	2.27E-13
45	39504.88	39038.08	3.6701	3.2115	1.92E-13

46	39620.22	39153.42	3.8564	3.3740	1.54E-13
47	39719.07	39252.28	3.9991	3.4874	1.30E-13
48	39817.12	39350.33	3.9941	3.4461	1.29E-13
49	39928.3	39461.51	3.9210	3.3500	1.28E-13

Table App. IV. Calculated $3^3\Sigma^-$ state (plotted in blue in Figure 2 at right) vibrational levels (cm^{-1}) using adiabatic PEC.

level	E(n)	$E(n)-E_{GS}(1)$	<R>	$(<1/R^2>)^{-1/2}$	FC
1	24906.13	24439.34	1.5867	1.5838	0.5750
2	25958.62	25491.82	1.6050	1.5961	0.3469
3	26978.57	26511.77	1.6246	1.6095	0.0725
4	27963.56	27496.77	1.6460	1.6244	0.0054
5	28908.39	28441.59	1.6705	1.6420	5.69E-05
6	29804.34	29337.55	1.6998	1.6638	5.28E-06
7	30639.80	30173.01	1.7364	1.6920	5.28E-07
8	31398.86	30932.06	1.7848	1.7306	1.29E-08
9	32062.23	31595.43	1.8497	1.7843	5.38E-09
10	32619.65	32152.85	1.9285	1.8506	6.17E-10
11	33092.98	32626.18	1.9976	1.9066	9.66E-11
12	33528.16	33061.37	2.0446	1.9404	2.49E-10
13	33950.34	33483.54	2.0801	1.9634	7.01E-11
14	34367.55	33900.76	2.1104	1.9816	3.03E-13
15	34781.68	34314.88	2.1388	1.9982	2.84E-11
16	35192.54	34725.75	2.1671	2.0147	3.05E-11
17	35599.02	35132.22	2.1962	2.0319	1.02E-11
18	35999.72	35532.92	2.2268	2.0503	2.83E-13
19	36393.25	35926.46	2.2595	2.0705	1.51E-12
20	36777.81	36311.01	2.2960	2.0939	3.52E-12
21	37150.75	36683.96	2.3377	2.1218	3.01E-12
22	37509.82	37043.02	2.3837	2.1533	1.54E-12
23	37853.49	37386.69	2.4352	2.1893	4.85E-13
24	38179.27	37712.48	2.4948	2.2323	6.00E-14
25	38484.56	38017.77	2.5631	2.2828	6.00E-15
26	38766.96	38300.17	2.6435	2.3439	8.40E-14
27	39023.67	38556.88	2.7388	2.4183	1.68E-13
28	39252.19	38785.40	2.8539	2.5110	2.13E-13
29	39450.05	38983.26	2.9948	2.6280	2.14E-13
30	39615.25	39148.46	3.1711	2.7795	1.85E-13
31	39746.64	39279.85	3.3972	2.9804	1.42E-13
32	39844.60	39377.81	3.6913	3.2498	9.90E-14
33	39914.82	39448.03	3.9740	3.5010	7.30E-14
34	39979.78	39512.98	3.9843	3.4512	7.90E-14

Figure App. 3. Plot of $^3\Sigma^+$ states (red and blue) and Δ states (open triangles), with ground $X^3\Sigma^-$ state for reference.

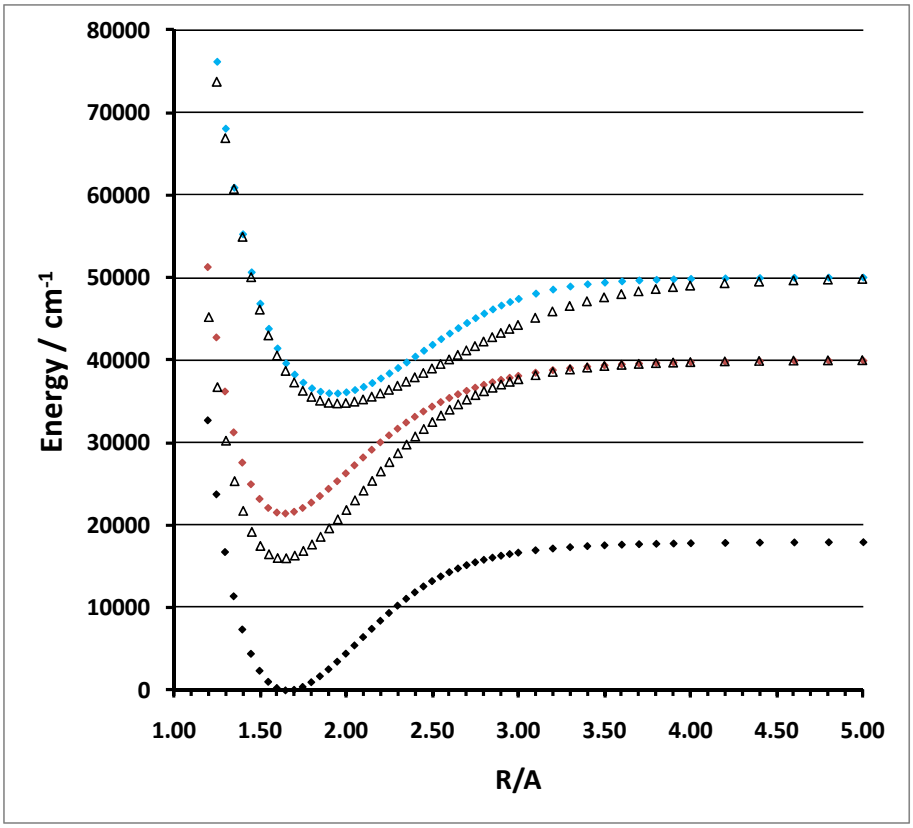

Table App. 5. Levels on $1^3\Sigma^+$ state (adiabat) plotted (in red) in Figure 3.

level	E(n)	$E(n)-E_{GS}(1)$	$\langle R \rangle$	$(\langle 1/R^2 \rangle)^{-1/2}$	FC
1	21938.95	21472.15	1.6505	1.6473	0.9664
2	22868.48	22401.68	1.6689	1.6593	0.0336
3	23778.66	23311.86	1.6876	1.6714	1.15E-06
4	24668.70	24201.90	1.7074	1.6844	2.03E-06
5	25535.11	25068.32	1.7281	1.6982	1.00E-07
6	26380.20	25913.40	1.7488	1.7118	3.50E-09
7	27204.16	26737.36	1.7706	1.7264	8.02E-09
8	28006.37	27539.57	1.7929	1.7412	4.00E-10
9	28787.25	28320.46	1.8162	1.7568	2.13E-09
10	29545.98	29079.18	1.8405	1.7732	4.08E-10
11	30281.92	29815.12	1.8663	1.7908	4.28E-10
12	30994.38	30527.58	1.8932	1.8092	4.58E-10
13	31683.03	31216.24	1.9215	1.8287	2.89E-12
14	32347.54	31880.74	1.9513	1.8494	2.46E-10
15	32987.32	32520.53	1.9828	1.8715	1.23E-10
16	33601.98	33135.18	2.0162	1.8951	1.83E-12
17	34191.01	33724.21	2.0517	1.9203	8.67E-11
18	34754.04	34287.24	2.0894	1.9473	7.83E-11
19	35290.72	34823.93	2.1295	1.9762	1.00E-11
20	35800.89	35334.09	2.1722	2.0073	7.63E-12
21	36284.52	35817.72	2.2175	2.0404	3.43E-11
22	36741.95	36275.16	2.2654	2.0755	3.20E-11
23	37173.30	36706.51	2.3174	2.1141	1.11E-11
24	37576.97	37110.18	2.3761	2.1586	2.06E-13
25	37951.71	37484.92	2.4396	2.2070	3.45E-12
26	38298.01	37831.21	2.5103	2.2617	9.85E-12
27	38613.98	38147.19	2.5908	2.3251	1.17E-11
28	38899.15	38432.35	2.6830	2.3991	9.14E-12
29	39151.80	38685.01	2.7906	2.4871	5.23E-12
30	39370.96	38904.17	2.9198	2.5957	2.22E-12
31	39555.49	39088.70	3.0777	2.7317	6.49E-13
32	39704.60	39237.80	3.2763	2.9074	9.30E-14
33	39818.47	39351.67	3.5359	3.1438	0.00E+00
34	39899.48	39432.68	3.8585	3.4424	2.40E-14
35	39961.40	39494.60	4.0286	3.5640	6.60E-14

Table App. 6. Levels on $2^3\Sigma^+$ state (adiabat) plotted (in blue) in Figure 3.

level	E(n)	$E(n)-E_{GS}(1)$	<R>	$(<1/R^2>)^{-1/2}$	FC
1	36345.33	35878.53	1.9373	1.9334	0.0162
2	36996.67	36529.87	1.9549	1.9432	0.0555
3	37643.94	37177.14	1.9722	1.9527	0.1042
4	38284.04	37817.25	1.9893	1.9620	0.1414
5	38915.98	38449.19	2.0073	1.9720	0.1541
6	39540.13	39073.33	2.0262	1.9828	0.1434
7	40156.00	39689.20	2.0457	1.9942	0.1187
8	40762.90	40296.10	2.0660	2.0062	0.0899
9	41360.20	40893.41	2.0871	2.0189	0.0637
10	41947.16	41480.37	2.1090	2.0321	0.0427
11	42523.16	42056.37	2.1320	2.0463	0.0275
12	43087.69	42620.90	2.1560	2.0613	0.0171
13	43640.12	43173.33	2.1813	2.0773	0.0104
14	44179.74	43712.95	2.2077	2.0942	0.0062
15	44705.80	44239.01	2.2358	2.1124	0.0037
16	45217.52	44750.72	2.2656	2.1320	0.0021
17	45714.15	45247.36	2.2972	2.1530	0.0012
18	46194.98	45728.19	2.3310	2.1758	0.0007
19	46658.64	46191.84	2.3685	2.2017	0.0004
20	47103.08	46636.28	2.4104	2.2312	0.0002
21	47526.52	47059.72	2.4570	2.2646	0.0001
22	47927.16	47460.37	2.5097	2.3034	8.28E-05
23	48302.64	47835.84	2.5702	2.3488	4.94E-05
24	48650.31	48183.51	2.6412	2.4036	2.99E-05
25	48966.99	48500.19	2.7259	2.4708	1.83E-05
26	49249.20	48782.40	2.8298	2.5558	1.13E-05
27	49493.13	49026.34	2.9600	2.6661	7.07E-06
28	49695.13	49228.33	3.1282	2.8139	4.41E-06
29	49852.24	49385.44	3.3541	3.0205	2.69E-06
30	49963.81	49497.01	3.6647	3.3147	1.56E-06
31	50037.10	49570.30	3.9987	3.6271	9.75E-07
32	50099.83	49633.03	4.0454	3.6130	9.97E-07

Table App. 7. Levels on 1Δ state (adiabat) plotted (lower, open triangles) in Figure 3.

level	E(n)	$E(n)-E_{GS}(1)$	<R>	$(<1/R^2>)^{-1/2}$	FC
1	16364.02	15897.22	1.6359	1.6329	0.9079
2	17341.54	16874.74	1.6526	1.6434	0.0900
3	18302.28	17835.48	1.6693	1.6538	0.0021
4	19247.34	18780.54	1.6863	1.6644	1.50E-05
5	20174.00	19707.20	1.7043	1.6760	2.28E-07
6	21081.92	20615.13	1.7221	1.6872	5.88E-09
7	21974.14	21507.35	1.7400	1.6984	8.23E-09
8	22849.52	22382.73	1.7585	1.7101	3.04E-09
9	23709.17	23242.37	1.7769	1.7216	1.56E-09
10	24553.11	24086.31	1.7958	1.7334	9.44E-10
11	25381.41	24914.61	1.8150	1.7455	6.81E-10
12	26193.60	25726.81	1.8350	1.7582	1.79E-10
13	26989.28	26522.48	1.8555	1.7713	4.44E-10
14	27768.17	27301.37	1.8766	1.7848	0.00E+00
15	28530.13	28063.34	1.8984	1.7988	2.09E-10
16	29274.76	28807.97	1.9211	1.8135	7.80E-11
17	30001.47	29534.68	1.9447	1.8289	1.75E-11
18	30709.76	30242.97	1.9694	1.8452	9.23E-11
19	31398.88	30932.09	1.9955	1.8626	2.53E-11
20	32068.11	31601.32	2.0230	1.8811	6.37E-12
21	32716.60	32249.81	2.0523	1.9011	3.87E-11
22	33343.49	32876.70	2.0834	1.9226	2.09E-11
23	33947.89	33481.10	2.1167	1.9458	9.80E-14
24	34528.96	34062.17	2.1524	1.9711	9.74E-12
25	35085.90	34619.11	2.1906	1.9987	1.62E-11
26	35618.12	35151.33	2.2316	2.0285	7.36E-12
27	36125.06	35658.26	2.2759	2.0612	2.23E-13
28	36605.36	36138.56	2.3251	2.0983	2.08E-12
29	37057.10	36590.30	2.3795	2.1400	5.75E-12
30	37479.60	37012.81	2.4388	2.1860	5.67E-12
31	37871.66	37404.86	2.5056	2.2387	2.98E-12
32	38231.91	37765.11	2.5800	2.2983	6.98E-13
33	38559.17	38092.37	2.6650	2.3677	0.00E+00
34	38852.24	38385.45	2.7624	2.4485	3.51E-13
35	39110.05	38643.25	2.8757	2.5445	8.92E-13
36	39331.85	38865.06	3.0104	2.6611	1.17E-12
37	39517.22	39050.42	3.1723	2.8042	1.15E-12
38	39666.65	39199.86	3.3713	2.9839	9.51E-13
39	39781.65	39314.86	3.6199	3.2124	7.02E-13
40	39866.37	39399.57	3.9056	3.4751	4.97E-13
41	39934.99	39468.19	4.0382	3.5612	4.52E-13

Table App. 8. Levels on 2Δ state (adiabat) plotted (upper, open triangles) in Figure 3.

level	E(n)	$E(n)-E_{GS}(1)$	<R>	$(<1/R^2>)^{-1/2}$	FC
1	35082.01	34615.22	1.9649	1.9607	0.0083
2	35670.50	35203.71	1.9873	1.9746	0.0315
3	36251.42	35784.63	2.0100	1.9887	0.0656
4	36822.66	36355.86	2.0330	2.0030	0.0993
5	37382.68	36915.88	2.0561	2.0172	0.1223
6	37931.78	37464.98	2.0800	2.0320	0.1295
7	38470.46	38003.67	2.1044	2.0473	0.1225
8	38999.15	38532.35	2.1292	2.0629	0.1064
9	39518.18	39051.39	2.1543	2.0786	0.0866
10	40027.91	39561.12	2.1794	2.0942	0.0669
11	40528.64	40061.85	2.2046	2.1099	0.0497
12	41020.55	40553.75	2.2301	2.1256	0.0357
13	41503.66	41036.87	2.2561	2.1418	0.0250
14	41978.05	41511.25	2.2824	2.1581	0.0171
15	42444.49	41977.70	2.3077	2.1735	0.0116
16	42903.98	42437.19	2.3332	2.1890	0.0077
17	43354.93	42888.13	2.3626	2.2077	0.0050
18	43794.76	43327.97	2.3936	2.2278	0.0033
19	44224.85	43758.05	2.4229	2.2461	0.0021
20	44645.11	44178.32	2.4562	2.2679	0.0014
21	45053.44	44586.65	2.4906	2.2904	0.0009
22	45450.87	44984.08	2.5263	2.3139	0.0006
23	45835.61	45368.82	2.5655	2.3404	0.0004
24	46207.80	45741.01	2.6062	2.3678	0.0002
25	46566.17	46099.38	2.6508	2.3986	0.0002
26	46910.51	46443.71	2.6983	2.4317	9.98E-05
27	47239.66	46772.86	2.7499	2.4681	6.58E-05
28	47553.30	47086.51	2.8061	2.5084	4.38E-05
29	47850.55	47383.75	2.8667	2.5523	2.95E-05
30	48130.80	47664.00	2.9337	2.6017	2.00E-05
31	48393.41	47926.62	3.0073	2.6568	1.38E-05
32	48637.69	48170.90	3.0885	2.7184	9.58E-06
33	48863.15	48396.36	3.1789	2.7883	6.74E-06
34	49069.26	48602.46	3.2809	2.8685	4.78E-06
35	49255.39	48788.59	3.3960	2.9608	3.43E-06
36	49421.46	48954.67	3.5264	3.0670	2.48E-06
37	49566.89	49100.10	3.6810	3.1966	1.80E-06
38	49692.26	49225.46	3.8430	3.3321	1.34E-06
39	49803.11	49336.31	3.9664	3.4270	1.07E-06
40	49912.54	49445.75	3.9635	3.3938	9.96E-07
41	50034.36	49567.57	3.8915	3.3036	9.67E-07

Figure App. 4. Quintet states ($^5\Sigma^-$ in red, $1^5\Pi$state in blue), with ground $X^3\Sigma^-$ state plotted in black for reference.

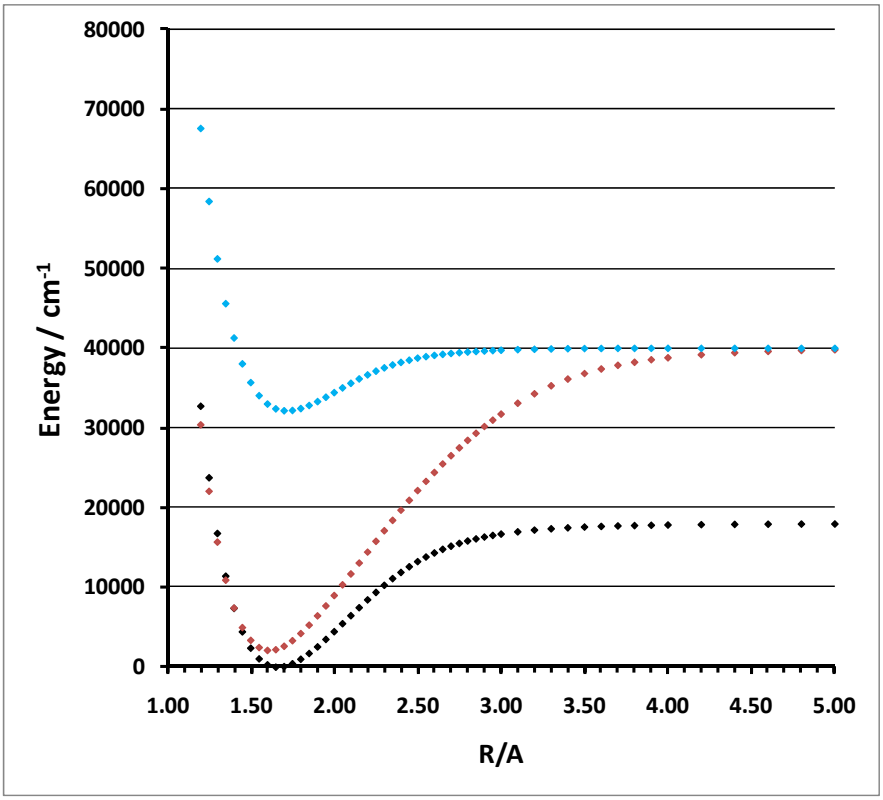

Table App. 9. All bound levels on the $^5\Sigma^-$ state. Energies are also listed relative to the lowest quintet and triplet states. The triplet-quintet gap is seen to be 2059 cm^{-1}. Franck-Condon factors with the ground triplet state are tabulated showing that the lowest quintet level has a large overlap with the triplet ground state.

level	E(n)	E(n)-E(1)	$E(n)-E_{trip}(1)$	<R>	$(<1/R^2>)^{-1/2}$	FC
1	2526.51	0.00	2059.71	1.6214	1.6185	0.8245
2	3547.00	1020.49	3080.20	1.6368	1.6279	0.1634
3	4551.47	2024.96	4084.68	1.6523	1.6374	0.0117
4	5540.27	3013.76	5073.48	1.6681	1.6470	0.0004
5	6513.75	3987.24	6046.95	1.6839	1.6566	9.72E-06
6	7472.26	4945.75	7005.47	1.7000	1.6664	1.57E-07
7	8416.18	5889.67	7949.38	1.7161	1.6762	1.15E-09
8	9345.85	6819.34	8879.05	1.7325	1.6861	9.56E-12
9	10261.59	7735.08	9794.80	1.7489	1.6961	2.02E-12
10	11163.69	8637.18	10696.90	1.7655	1.7061	4.87E-12
11	12052.39	9525.88	11585.59	1.7823	1.7162	3.97E-12
12	12927.88	10401.37	12461.09	1.7993	1.7264	1.06E-13
13	13790.33	11263.83	13323.54	1.8164	1.7368	1.44E-12
14	14639.88	12113.37	14173.08	1.8338	1.7472	6.00E-15
15	15476.61	12950.10	15009.82	1.8514	1.7578	5.96E-13
16	16300.62	13774.11	15833.82	1.8692	1.7686	5.00E-15
17	17111.96	14585.46	16645.17	1.8873	1.7795	3.24E-13
18	17910.69	15384.19	17443.90	1.9056	1.7906	5.00E-15
19	18696.84	16170.33	18230.05	1.9243	1.8019	1.63E-13
20	19470.42	16943.91	19003.63	1.9432	1.8133	4.50E-14
21	20231.46	17704.96	19764.67	1.9624	1.8250	4.10E-14
22	20980.20	18453.69	20513.40	1.9817	1.8367	7.10E-14
23	21717.28	19190.77	21250.49	2.0007	1.8481	0.00E+00
24	22443.48	19916.97	21976.68	2.0199	1.8595	4.30E-14
25	23158.34	20631.83	22691.55	2.0402	1.8719	2.00E-14
26	23860.09	21333.58	23393.29	2.0620	1.8855	4.00E-15
27	24548.52	22022.01	24081.72	2.0833	1.8986	2.70E-14
28	25225.48	22698.97	24758.69	2.1041	1.9111	8.00E-15
29	25890.78	23364.27	25423.99	2.1262	1.9248	3.00E-15
30	26543.47	24016.96	26076.67	2.1487	1.9387	1.70E-14
31	27184.41	24657.90	26717.61	2.1711	1.9524	7.00E-15
32	27813.39	25286.88	27346.60	2.1945	1.9669	0.00E+00
33	28430.21	25903.70	27963.41	2.2181	1.9815	9.00E-15
34	29035.09	26508.58	28568.29	2.2424	1.9967	9.00E-15
35	29627.72	27101.21	29160.92	2.2674	2.0123	1.00E-15
36	30208.12	27681.62	29741.33	2.2930	2.0284	2.00E-15
37	30776.07	28249.56	30309.28	2.3195	2.0452	6.00E-15
38	31331.41	28804.90	30864.62	2.3468	2.0626	5.00E-15
39	31873.90	29347.39	31407.10	2.3752	2.0808	1.00E-15
40	32403.27	29876.76	31936.47	2.4047	2.0998	1.00E-15
41	32919.21	30392.71	32452.42	2.4355	2.1198	4.00E-15
42	33421.39	30894.88	32954.59	2.4677	2.1410	4.00E-15
43	33909.39	31382.89	33442.60	2.5015	2.1634	1.00E-15

44	34382.80	31856.29	33916.00	2.5372	2.1873	0.00E+00
45	34841.11	32314.60	34374.31	2.5748	2.2129	1.00E-15
46	35283.81	32757.30	34817.02	2.6149	2.2404	2.00E-15
47	35710.33	33183.82	35243.54	2.6576	2.2700	2.00E-15
48	36120.06	33593.55	35653.27	2.7032	2.3022	1.00E-15
49	36512.36	33985.85	36045.56	2.7523	2.3373	0.00E+00
50	36886.54	34360.03	36419.74	2.8054	2.3757	0.00E+00
51	37241.91	34715.40	36775.12	2.8629	2.4180	0.00E+00
52	37577.77	35051.26	37110.98	2.9255	2.4648	1.00E-15
53	37893.42	35366.91	37426.62	2.9940	2.5169	1.00E-15
54	38188.18	35661.67	37721.39	3.0693	2.5751	1.00E-15
55	38461.44	35934.93	37994.64	3.1524	2.6406	1.00E-15
56	38712.63	36186.12	38245.83	3.2448	2.7147	0.00E+00
57	38941.30	36414.79	38474.50	3.3479	2.7990	0.00E+00
58	39147.09	36620.58	38680.30	3.4642	2.8961	0.00E+00
59	39329.78	36803.27	38862.99	3.5960	3.0084	0.00E+00
60	39489.42	36962.92	39022.63	3.7466	3.1395	0.00E+00
61	39626.74	37100.24	39159.95	3.9105	3.2837	0.00E+00
62	39748.09	37221.59	39281.30	4.0148	3.3615	0.00E+00
63	39871.82	37345.31	39405.02	3.9851	3.2982	0.00E+00

Table App. 10: transitions between the $^5\Sigma^-$ and the $1^5\Pi$ state.

level	E(n)	$E(n)-E_{GS}(1)$	$\langle R \rangle$	$(\langle 1/R^2 \rangle)^{-1/2}$	FC
1	32568.22	30041.66	1.7293	1.7256	0.4509
2	33344.86	30818.30	1.7542	1.7432	0.3286
3	34092.27	31565.71	1.7809	1.7621	0.1450
4	34809.22	32282.66	1.8096	1.7827	0.0516
5	35494.15	32967.59	1.8408	1.8053	0.0166
6	36145.09	33618.53	1.8752	1.8306	0.0051
7	36759.46	34232.90	1.9137	1.8594	0.0016
8	37334.01	34807.45	1.9578	1.8929	0.0005
9	37864.74	35338.18	2.0094	1.9328	0.0002
10	38347.07	35820.51	2.0705	1.9811	5.82E-05
11	38777.74	36251.18	2.1427	2.0390	2.20E-05
12	39151.85	36625.29	2.2406	2.1202	8.74E-06
13	39451.99	36925.43	2.3765	2.2380	3.71E-06
14	39687.40	37160.84	2.5355	2.3749	1.77E-06
15	39858.46	37331.90	2.7568	2.5703	8.80E-07
16	39966.15	37439.59	3.1840	2.9661	3.53E-07

Spin-orbit coupling

The experimental spectra allowed determination of the spin-orbit (SO) constant *A* splitting the Π-states in the molecular region into three levels: Ω = 0+/-, ±1, ±2 with energies of –A, 0, A. For the $3^3\Pi$-state in the Franck-Condon region, the spectra are more consistent with (but not definitive about) a negative sign for *A* corresponding to an inverted order with Ω = ±2 being the lowest. The recorded magnitude of *A* decreases with increasing vibrational quanta from 9.9 to 9.0 (see Table 3 in paper).

It is possible to calculate SO splittings quite accurately with ab initio calculations using the Breit-Pauli operator method, and in principle one can follow each fine structure level out to well-known atomic asymptotes. In practice it can be challenging to follow the large number of fine-structure levels. In regions of avoided crossings between adiabatic states, *A* can change very rapidly, since due to its relation to the character of states it more smoothly follows the diabatic states.

SO coupling is small in BeC. Asymptotically the ground $^3\Sigma^-$ and first triplet Π state ($1^3\Pi$) correlate with ground state atoms C(^3P_g) and Be(^1S_g). The ground state of carbon is split into *J* = 0, 1, and 2 levels at 0.0, 16.40, and 43.40 cm^{-1} respectively. Molpro calculations for separate atoms (or a lone C-atom) using the Breit-Pauli operator method and MRCI with all-electrons correlated slightly underestimate the splitting yielding (0, 13.2, 39.6) cm^{-1} with the aug-cc-pwCVQZ basis, and (0, 13.4, 40.1) cm^{-1} with the aug-cc-pwCV5Z basis. CBS extrapolation only produces (0, 13.5, 40.6) compared with (0, 16.4, 43.4) from experiment.

Figure App. 5 shows the ground $^3\Sigma^-$ state and the first 4 Π-states in the adiabatic and diabatic representations.

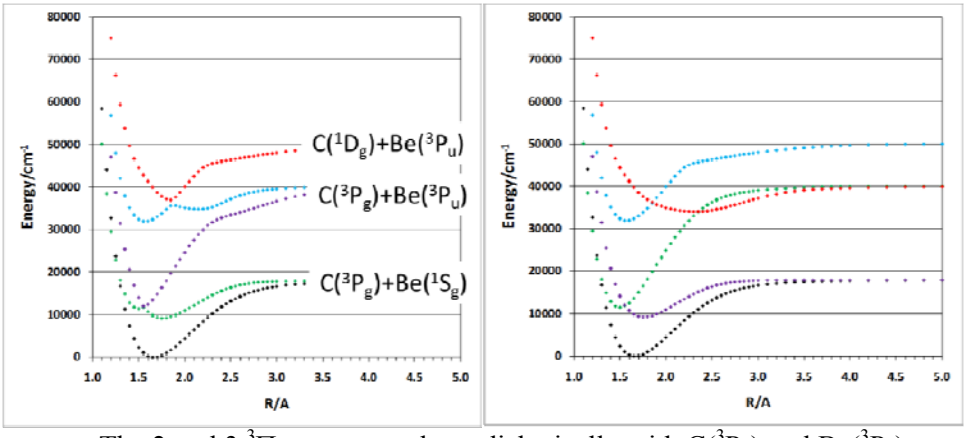

The 2 and 3 $^3\Pi$-states correlate adiabatically with C(^3P_g) and Be(^3P_u) atoms and an energy splitting pattern that is a combination of the *J* = 0, 1, 2 splitting from carbon (0, 16.4, 43.4) and a smaller *J* = 0, 1, 2 splitting from beryllium (0, 0.65, 2.99). However, it is clear from Figure 5, that the four-state model is neglecting a crossing with the next higher Π-state at R ~ 2.2 Å.

Figure 6 shows the first 11 Π-states at the CASSCF level. The diabatic state corresponding to the $3^3\Pi$-state at R = 1.5 Å can easily be followed by eye to the C(^5S_u) + Be(^3P_u) asymptote. The two

highest states corresponding to $C(^3P_g) + Be(^1P_u)$ should actually appear just above the four states corresponding to $C(^1D_g) + Be(^3P_u)$. The $Be(^1P_u)$ atomic state is too high in energy at the CASSCF level, but we have confirmed that the correct order is restored when electron correlation through MRCI is included. Also some high-lying states whose atomic asymptotes involve 3rd shell configurations don't appear due to the full-valence active space used here (higher occupations weren't considered).

Figure App. 6. Lowest 11 Π-states at the CASSCF/aug-cc-pwCVQZ level (see text).

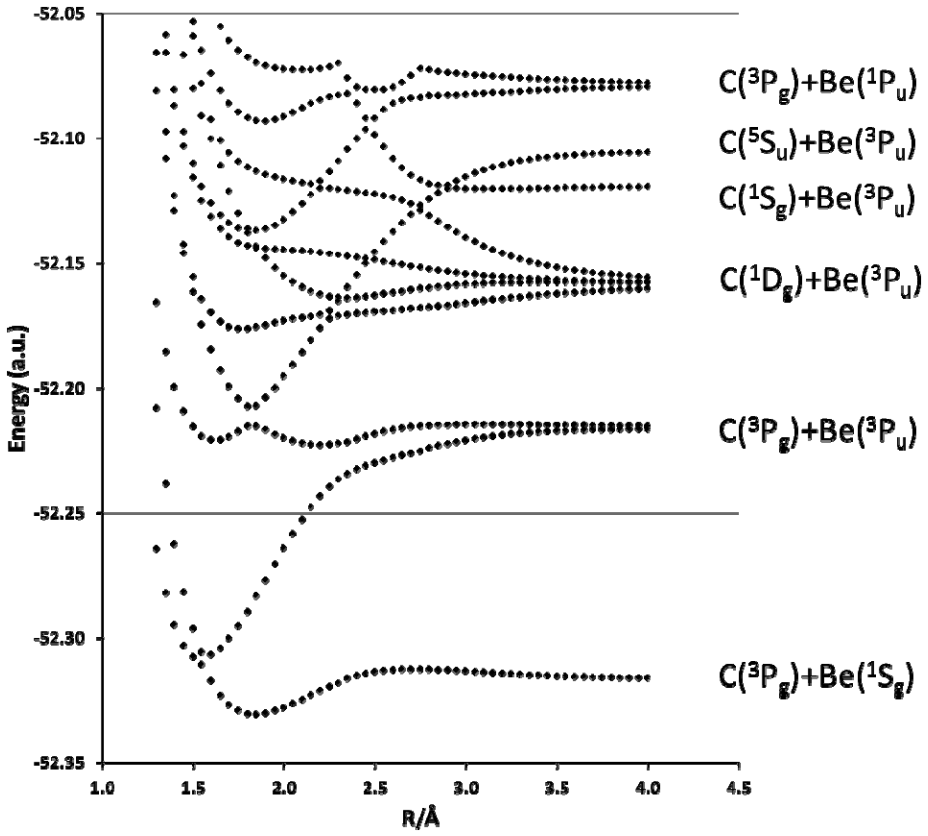

In Figure App. 7, splittings from the individual components of the ground state atoms are followed into the molecular region, tending to no splitting of the ground $^3\Sigma^-$ state (as expected) and a value for *A* of ~9 cm^{-1} at R = 1.6 Å.

Figure App. 7. Spin-orbit splittings for the ground ($^3\Sigma^-$) and 1st Π-state of BeC which correspond to ground state atoms, Be(^1S_g) and C(^3P_g). The *J* = 0, 1, 2 levels of C($^3P_{0,1,2}$) are calculated at 0, 13.2, and 39.6 cm^{-1} at the MRCI(AE)/aug-cc-pwCVQZ level (experimental values are 0, 16.4, 43.4 cm^{-1}). As expected the splitting for the ground ($^3\Sigma^-$) state becomes zero in the molecular region. The 1st Π-state splitting reaches A = 9.04 cm-1 at 1.6 Å (just before the avoided crossing with the second Π-state).

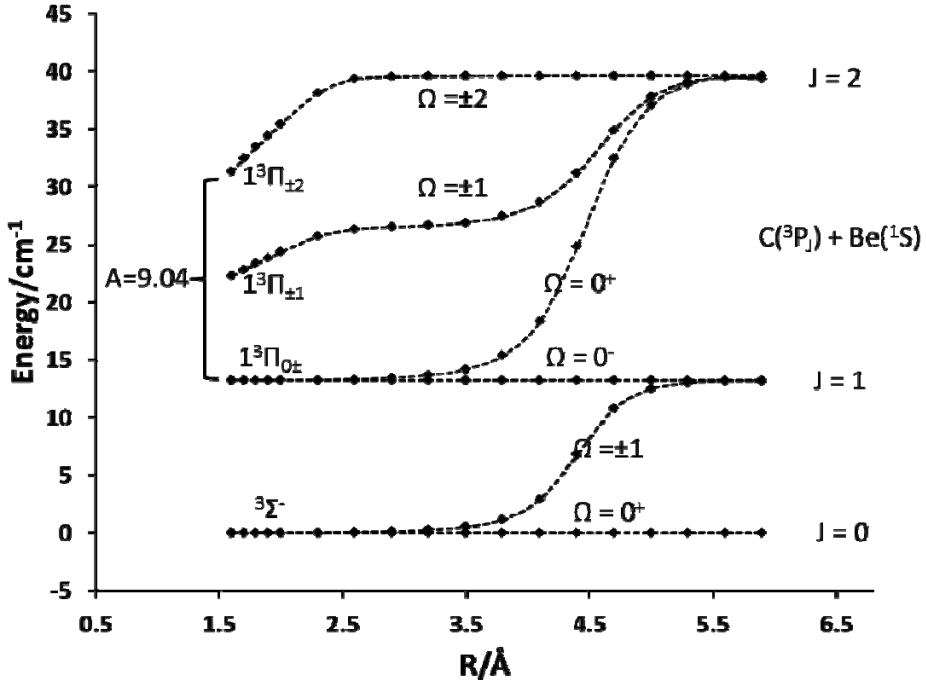

The SO constant *A* for the $1^3\Pi$-state was expected to be negative at R = 1.5 Å. The adiabatic state barely avoids crossing with $2^3\Pi$ at R ~ 1.55 Å. Figure 8 shows a plot of the SO constants for the two states through that region with *A* for both states reversing signs at the crossing.

Figure App. 8. The SO constants of the first two Π-states plotted in the adiabatic representation. The constants switch with each other over a very short distance in the diabatic crossing region (see Figure App. 5).

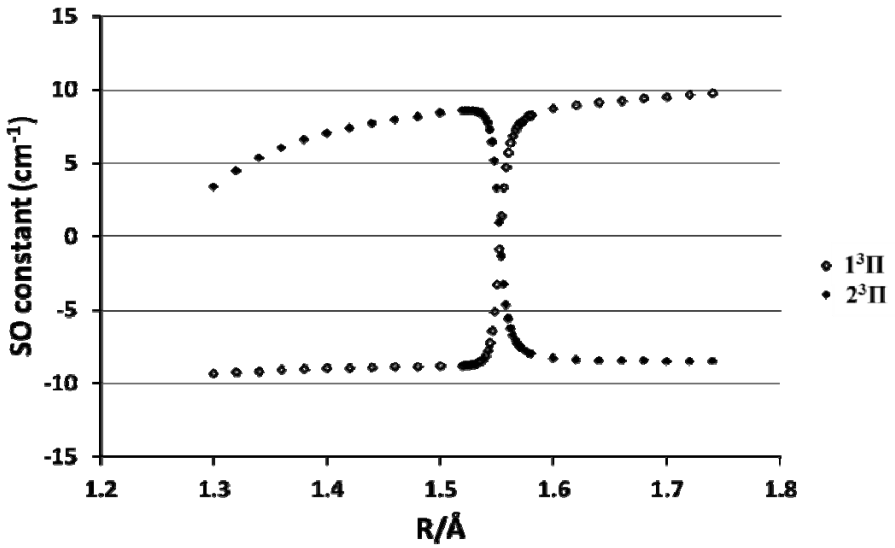

A plot of the SO constants for the first four Π-states is shown in Figure 9. In the region of each crossing, the SO constants rapidly switch. In fact the slopes of the constants (how quickly they switch) is roughly proportional to the adiabatic gaps between the states. The barely avoided crossing between $1^3\Pi$ and $2^3\Pi$ at R ~ 1.55 Å is the fastest, while that between $2^3\Pi$ and $3^3\Pi$ at R ~ 2.35 Å is much slower.

Figure App. 9. The SO constants *A*, for the lowest four Π-states in the adiabatic representation. Rapid switching is recorded in the region of avoided crossings.

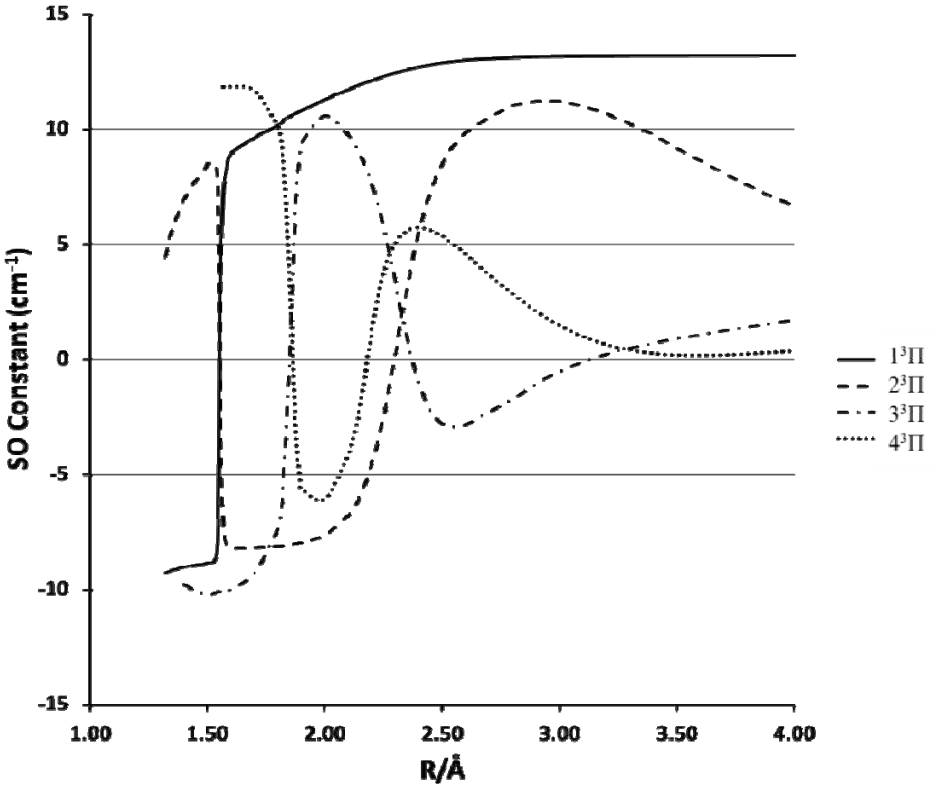

As seen in Figures App. 7-9, the SO constant for $1^3\Pi$ is negative at R < 1.55 Å and positive for R > 1.55 Å. For $2^3\Pi$, SO switches from positive to negative at R ~ 1.55 Å and switches again (back to positive) at R ~ 2.35 Å and is thus expected to be positive asymptotically. This is confirmed in Figure 10 where the individual Ω components are followed confirming their *regular* order. SO for $3^3\Pi$ ranges from ~-10 cm^{-1} at R = 1.5 Å to ~-7 cm^{-1} at R = 1.8 Å in close agreement with the experiment.

Figure App. 10. Asymptotic behavior of $2^3\Pi$ confirming the regular ordering (positive *A*) at R > 2.35 Å. As discussed in the text, the 2 and 3 $^3\Pi$-states correlate adiabatically with C(^3P_g) and Be(^3P_u) atoms and an energy splitting pattern that is a combination of the *J* = 0, 1, 2 splitting from carbon (0, 16.4, 43.4) and a smaller *J* = 0, 1, 2 splitting from beryllium (0, 0.65, 2.99).

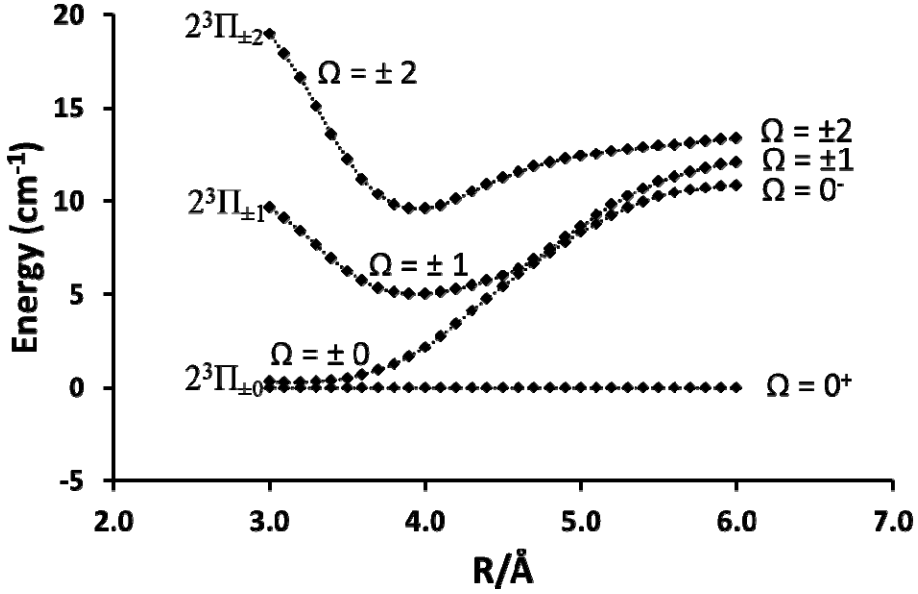

SO for the $3^3\Pi$ adiabat was confirmed to be as it appears in Figure App. 9 (small, positive and increasing slightly towards the atomic asymptote). Since the diabatic states tend to maintain their character over crossings, the asymptotic behavior of the $3^3\Pi$ diabat was also determined. Figure App. 11 shows the behavior approaching the high lying C(^5S_u) + Be(^3P_u) asymptote (see Figure App. 6) with the small splitting coming from the Be(^3P_u) state. Since these atomic states combine to form triplets, quintets and septets, the higher multiplicity states were also computed and found to be numerically exactly degenerate as expected.

Figure App. 11. Splitting of the $^3\Pi$ state correlating with the high lying $C(^5S_u)$ + $Be(^3P_u)$ asymptote. The inverted order (negative *A*), is confirmed asymptotically for the diabatic $3^3\Pi$ state.

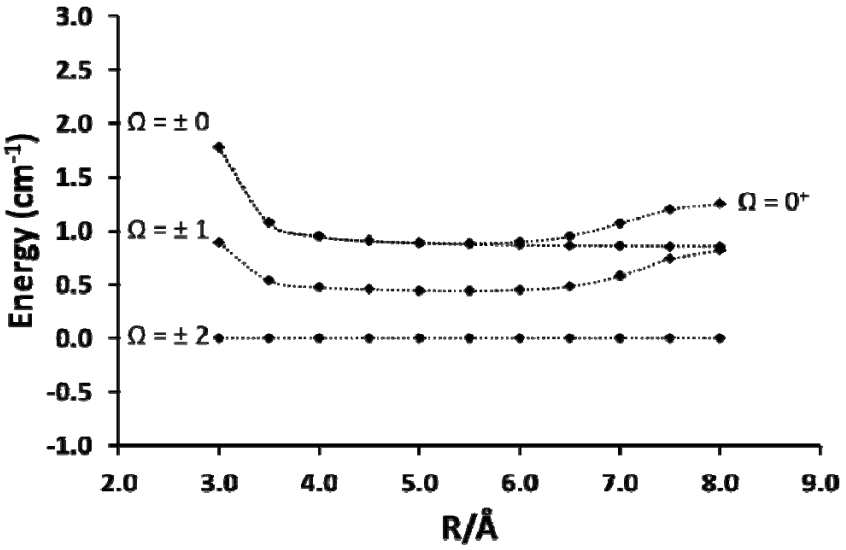

Table App. 11. Fitting of the BeC $(3)^3\Pi$-$X^3\Sigma^-$ 0-0 band (B"=1.1624 cm^{-1}, fixed).

(Data taken using a laser linewidth of 0.15 cm^{-1})

Observed	Calculated	Obs-Calc	Line
31789.20	31789.17	0.03	qR12(1)
31789.20	31789.17	0.03	qQ1(2)
31789.20	31789.32	-0.12	pP3(7)
31789.20	31789.14	0.07	pQ23(4)
31789.20	31788.71	0.49	pP3(8)
31789.20	31789.14	0.07	pP2(5)
31817.22	31817.24	-0.02	rR1(7)
31817.22	31817.20	0.02	rR2(5)
31817.22	31817.21	0.01	rR3(3)
31817.22	31817.21	0.01	rQ32(4)
31817.22	31817.20	0.02	rQ21(6)
31817.22	31817.68	-0.46	rQ32(12)
31832.36	31832.60	-0.24	rR3(7)
31832.36	31832.60	-0.24	rQ32(8)
31791.04	31791.03	0.01	qQ1(3)
31791.04	31791.50	-0.46	rR1(1)
31791.04	31791.03	0.01	qR12(2)
31791.04	31790.68	0.36	pQ23(3)
31782.78	31782.70	0.08	pP1(7)
31782.78	31782.45	0.33	pP1(8)
31782.78	31782.37	0.41	pP1(9)
31782.78	31782.47	0.31	pP1(10)
31782.78	31782.70	0.08	pQ12(6)
31782.78	31782.77	0.00	pP1(11)
31782.78	31782.45	0.33	pQ12(7)
31782.78	31782.37	0.41	pQ12(8)
31794.59	31794.71	-0.12	qQ1(5)
31794.59	31794.71	-0.12	qR12(4)
31796.50	31796.65	-0.15	qQ1(6)
31837.45	31837.29	0.17	qR23(8)
31837.45	31837.52	-0.06	rR1(11)
31835.07	31835.01	0.06	sR32(9)
31835.07	31835.18	-0.10	sR21(6)
31830.17	31830.14	0.03	sR32(8)
31830.17	31830.14	0.03	sQ31(9)
31814.16	31814.04	0.12	pQ23(9)
31814.16	31814.36	-0.20	rQ32(3)
31814.16	31814.59	-0.43	rQ32(11)

31814.16	31814.36	-0.20	rR3(2)
31811.89	31811.68	0.21	qQ3(8)
31811.89	31811.76	0.13	rQ32(10)
31811.89	31811.94	-0.05	qQ1(12)
31811.89	31812.03	-0.13	rQ32(2)
31811.89	31812.03	-0.13	rR3(1)
31811.89	31811.60	0.29	sR21(2)
31810.13	31810.06	0.07	rQ21(4)
31810.13	31810.06	0.07	rR2(3)
31810.13	31810.34	-0.20	rQ32(1)
31810.13	31810.34	-0.20	rP31(2)
31799.70	31799.83	-0.13	rR1(3)
31799.70	31799.98	-0.28	qQ2(3)
31799.70	31799.98	-0.28	qR23(2)
31799.70	31799.98	-0.28	qP21(4)
31801.63	31801.85	-0.22	qQ2(5)
31801.63	31801.56	0.07	rQ21(1)
31801.63	31801.85	-0.22	qP21(6)
31801.63	31801.85	-0.22	qR23(4)
31821.32	31821.23	0.09	rR2(6)
31821.32	31821.23	0.09	rQ21(7)
31821.32	31821.05	0.27	rQ32(13)
31824.26	31824.19	0.07	rR3(5)
31824.26	31824.19	0.07	rQ32(6)
31786.01	31786.35	-0.34	pP2(8)
31786.01	31786.02	-0.01	pP2(9)
31786.01	31785.97	0.05	qP32(10)
31786.01	31786.19	-0.18	qP32(11)
31786.01	31786.35	-0.34	pQ23(7)
31786.01	31786.02	-0.01	pQ23(8)
31840.19	31840.16	0.03	sR32(10)
31826.67	31826.95	-0.27	rR1(9)
31805.40	31805.58	-0.18	qQ3(4)
31805.40	31804.95	0.45	qQ2(7)
31805.40	31805.06	0.35	qQ3(3)

73 Observations, 3 Parameters. Predicted New Error: 0.220725909582493

Parameters:

1.	Origin=	31797.005(41)
2.	B'=	1.29339(62)
3.	A'=-	-9.779(52)

Correlation Matrix:

	1	2	3
1	1.000		
2	-0.782	1.000	
3	0.001	0.028	1.000

Table XII. Fitting of the BeC $(1)^5\Pi$-$(1)^5\Sigma^-$ 1-0 band (B"=1.229 cm^{-1}, fixed).

(Data taken using a laser linewidth of 0.6 cm^{-1})

Observed	Calculated	Obs-Calc	Line
30798.42	30798.22	0.20	qR23(6)
30798.42	30798.43	-0.01	qR23(7)
30798.42	30798.26	0.16	qR23(8)
30798.42	30797.71	0.71	sR43(9)
30798.42	30798.51	-0.09	qR12(6)
30798.42	30798.32	0.10	qR12(5)
30798.42	30798.33	0.09	qR12(7)
30798.42	30797.77	0.65	qR12(8)
30798.42	30797.75	0.67	qR12(4)
30766.64	30766.73	-0.09	rQ43(13)
30766.64	30766.78	-0.14	pQ12(12)
30766.64	30766.48	0.16	oP23(9)
30766.64	30766.81	-0.17	sQ31(11)
30766.64	30766.85	-0.21	oQ24(10)
30766.64	30766.56	0.08	oP12(8)
30766.64	30766.88	-0.24	pQ45(9)
30766.64	30766.63	0.01	rP31(7)
30766.64	30766.69	-0.05	qP54(6)
30766.64	30766.73	-0.09	oP45(5)
30771.26	30770.88	0.38	rQ43(12)
30771.26	30770.93	0.33	pQ12(11)
30771.26	30770.97	0.29	sQ31(10)
30771.26	30771.01	0.25	rQ54(9)
30771.26	30771.18	0.08	oP23(8)
30771.26	30771.04	0.22	pQ45(8)
30771.26	30771.28	-0.02	oP12(7)
30771.26	30771.37	-0.11	rP31(6)
30771.26	30771.43	-0.17	nP24(5)
30771.26	30771.48	-0.22	oP45(4)
30775.24	30774.65	0.59	rQ43(11)
30775.24	30774.71	0.53	pQ12(10)
30775.24	30774.75	0.49	sQ31(9)
30775.24	30774.79	0.45	rQ54(8)
30775.24	30774.83	0.41	pQ45(7)
30775.24	30775.50	-0.26	oP23(7)
30775.24	30775.63	-0.39	oP12(6)
30775.24	30775.74	-0.50	rP31(5)
30775.24	30775.81	-0.57	nP24(4)

30778.15	30778.04	0.11	rQ43(10)
30778.15	30778.10	0.05	pQ12(9)
30778.15	30778.16	-0.01	sQ31(8)
30778.15	30778.20	-0.05	rQ54(7)
30778.15	30778.24	-0.09	pQ45(6)
30778.15	30779.43	-1.28	oP23(6)
30778.15	30779.61	-1.46	sP52(5)
30761.61	30761.39	0.22	qP43(10)
30761.61	30762.21	-0.60	rQ43(14)
30761.61	30762.24	-0.63	pQ12(13)
30761.61	30761.46	0.15	oP12(9)
30761.61	30762.28	-0.67	sQ31(12)
30761.61	30761.52	0.09	rP31(8)
30761.61	30762.31	-0.70	oQ24(11)
30761.61	30762.34	-0.73	qQ5(10)
30761.61	30761.57	0.04	qP54(7)
30761.61	30761.61	0.00	oP45(6)
30752.34	30752.01	0.33	rQ43(16)
30752.34	30752.05	0.29	pQ12(15)
30752.34	30752.08	0.26	sQ31(14)
30752.34	30752.10	0.24	oQ24(13)
30752.34	30752.13	0.21	qQ5(12)
30749.91	30750.07	-0.16	qP43(12)
30749.91	30750.13	-0.22	oP12(11)
30749.91	30750.17	-0.26	rP31(10)
30749.91	30750.21	-0.30	nP24(9)
30749.91	30750.25	-0.34	oP45(8)
30761.61	30761.39	0.22	qP43(10)
30761.61	30762.21	-0.60	rQ43(14)
30761.61	30762.24	-0.63	pQ12(13)
30761.61	30761.46	0.15	oP12(9)
30761.61	30762.28	-0.67	sQ31(12)
30761.61	30761.52	0.09	rP31(8)
30761.61	30762.31	-0.70	oQ24(11)
30761.61	30762.34	-0.73	qQ5(10)
30761.61	30761.57	0.04	qP54(7)
30761.61	30761.61	0.00	oP45(6)
30766.62	30766.73	-0.11	rQ43(13)
30766.62	30766.78	-0.16	pQ12(12)
30766.62	30766.48	0.14	qP43(9)
30766.62	30766.81	-0.19	sQ31(11)
30766.62	30766.85	-0.23	oQ24(10)
30766.62	30766.56	0.06	oP12(8)

30766.62	30766.88	-0.26	qQ5(9)
30766.62	30766.63	-0.01	rP31(7)
30766.62	30766.69	-0.07	qP54(6)
30766.62	30766.73	-0.11	oP45(5)
30771.23	30770.88	0.35	rQ43(12)
30771.23	30770.93	0.30	pQ12(11)
30771.23	30770.97	0.26	sQ31(10)
30771.23	30771.01	0.22	oQ24(9)
30771.23	30771.18	0.05	oP23(8)
30771.23	30771.04	0.19	qQ5(8)
30771.23	30771.28	-0.05	oP12(7)
30771.23	30771.37	-0.14	rP31(6)
30771.23	30771.43	-0.20	qP54(5)
30771.23	30771.48	-0.25	oP45(4)
30775.22	30774.65	0.57	rQ43(11)
30775.22	30774.71	0.51	pQ12(10)
30775.22	30774.75	0.47	sQ31(9)
30775.22	30774.79	0.43	oQ24(8)
30775.22	30774.83	0.39	pQ45(7)
30775.22	30775.50	-0.28	oP23(7)
30775.22	30775.63	-0.41	oP12(6)
30775.22	30775.74	-0.52	rP31(5)
30775.22	30775.81	-0.59	nP24(4)
30778.15	30778.04	0.11	rQ43(10)
30778.15	30778.10	0.05	pQ12(9)
30778.15	30778.16	-0.01	sQ31(8)
30778.15	30778.20	-0.05	rQ54(7)
30778.15	30778.24	-0.09	pQ45(6)
30781.16	30781.05	0.11	rQ43(9)
30781.16	30781.12	0.04	pQ12(8)
30781.16	30781.18	-0.02	sQ31(7)
30781.16	30781.23	-0.07	rQ54(6)
30781.16	30781.28	-0.12	pQ45(5)
30783.99	30783.68	0.31	rQ43(8)
30783.99	30783.77	0.22	pQ12(7)
30783.99	30783.84	0.15	sQ31(6)
30783.99	30783.89	0.10	rQ54(5)
30783.99	30783.94	0.05	pQ45(4)
30783.99	30782.95	1.04	oP23(5)
30786.17	30785.93	0.24	pQ23(7)
30786.17	30786.03	0.14	pQ12(6)
30786.17	30786.11	0.06	sQ31(5)
30786.17	30786.18	-0.01	rQ54(4)

30786.17	30786.23	-0.06	pQ45(3)
30798.27	30798.22	0.05	qR23(6)
30798.27	30797.62	0.65	qR23(5)
30798.27	30798.43	-0.16	sR43(7)
30798.27	30798.26	0.01	sR43(8)
30798.27	30798.51	-0.24	qR12(6)
30798.27	30798.32	-0.05	qR12(5)
30798.27	30797.71	0.56	sR43(9)
30798.27	30798.33	-0.06	qR12(7)
30798.27	30797.75	0.52	qR12(4)
30798.27	30797.77	0.50	qR12(8)
30794.2	30793.40	0.80	pR13(2)
30794.2	30793.97	0.23	rQ43(2)
30794.2	30793.77	0.43	tR53(12)
30794.2	30793.81	0.39	qR12(11)
30794.2	30793.85	0.35	sR21(10)
30794.2	30793.89	0.31	qR34(9)
30794.2	30794.37	-0.17	pP3(2)
30794.2	30793.92	0.28	qR45(8)
30761.61	30761.39	0.22	oP23(10)
30761.61	30762.21	-0.60	rQ43(14)
30761.61	30762.24	-0.63	pQ12(13)
30761.61	30761.46	0.15	oP12(9)
30761.61	30762.28	-0.67	sQ31(12)
30761.61	30761.52	0.09	rP31(8)
30761.61	30762.31	-0.70	oQ24(11)
30761.61	30762.34	-0.73	qQ5(10)
30761.61	30761.57	0.04	qP54(7)
30761.61	30761.61	0.00	oP45(6)
30766.62	30766.73	-0.11	rQ43(13)
30766.62	30766.78	-0.16	pQ12(12)
30766.62	30766.48	0.14	oP23(9)
30766.62	30766.81	-0.19	sQ31(11)
30766.62	30766.85	-0.23	oQ24(10)
30766.62	30766.56	0.06	oP12(8)
30766.62	30766.88	-0.26	pQ45(9)
30766.62	30766.63	-0.01	rP31(7)
30766.62	30766.69	-0.07	qP54(6)
30766.62	30766.73	-0.11	oP45(5)
30771.23	30770.88	0.35	rQ43(12)
30771.23	30770.93	0.30	pQ12(11)
30771.23	30770.97	0.26	sQ31(10)
30771.23	30771.01	0.22	rQ54(9)

30771.23	30771.18	0.05	oP23(8)
30771.23	30771.04	0.19	pQ45(8)
30771.23	30771.28	-0.05	oP12(7)
30771.23	30771.37	-0.14	rP31(6)
30771.23	30771.43	-0.20	nP24(5)
30771.23	30771.48	-0.25	oP45(4)
30775.64	30774.65	0.99	rQ43(11)
30775.64	30774.71	0.93	pQ12(10)
30775.64	30774.75	0.89	sQ31(9)
30775.64	30774.79	0.85	rQ54(8)
30775.64	30774.83	0.81	pQ45(7)
30775.64	30775.50	0.14	oP23(7)
30775.64	30775.63	0.01	oP12(6)
30775.64	30775.74	-0.10	rP31(5)
30775.64	30775.81	-0.17	nP24(4)
30778.15	30778.04	0.11	rQ43(10)
30778.15	30778.10	0.05	pQ12(9)
30778.15	30778.16	-0.01	sQ31(8)
30778.15	30778.20	-0.05	rQ54(7)
30778.15	30778.24	-0.09	pQ45(6)
30778.15	30779.43	-1.28	oP23(6)
30781.16	30781.05	0.11	pQ23(9)
30781.16	30781.12	0.04	pQ12(8)
30781.16	30781.18	-0.02	sQ31(7)
30781.16	30781.28	-0.12	pQ45(5)
30784.07	30783.68	0.39	pQ23(8)
30784.07	30783.77	0.30	pQ12(7)
30784.07	30783.84	0.23	sQ31(6)
30784.07	30783.89	0.18	rQ54(5)
30784.07	30783.94	0.13	pQ45(4)
30786.17	30785.93	0.24	pQ23(7)
30786.17	30786.03	0.14	pQ12(6)
30786.17	30786.11	0.06	sQ31(5)
30786.17	30786.18	-0.01	oQ24(4)
30786.17	30786.23	-0.06	pQ45(3)
30789.61	30789.26	0.35	pQ23(5)
30789.61	30790.94	-1.33	oQ13(3)
30789.61	30790.94	-1.33	qR12(2)
30789.61	30790.32	-0.71	qR12(3)

206 Observations, 3 Parameters Predicted New Error: 0.4066

Parameters:

1.	Origin=	30791.745(52)
2.	B'=	1.04004(60)
3.	A'=-	-0.351(94)

Correlation Matrix

	1	2	3
1	1.000		
2	-0.836	1.000	
3	-0.142	0.134	1.000